Master of Science Thesis

Base Drag Reduction of Heavy Duty Vehicles by Combining a Tail and Guide Vanes

A Numerical and Experimental Analysis

M.L. Hoogendoorn

TU Delft

Base Drag Reduction of Heavy Duty Vehicles by Combining a Tail and Guide Vanes

A Numerical and Experimental Analysis

by

M.L. Hoogendoorn

to obtain the degree of Master of Science
at the Delft University of Technology,
to be defended publicly on Friday February 23, 2018 at 10:30 AM.

Student number:	4103963	
Thesis committee:	Prof. dr. ir. L.L.M. Veldhuis,	Chair
	Dr. ir. G.M.R. van Raemdonck,	Supervisor
	Ir. W.A. Timmer,	Supervisor
	Dr. ir. A.H. van Zuijlen	Examiner

Cover image courtesy of Wabco Optiflow [69], edited by Marit Schavemaker
An electronic version of this thesis is available at http://repository.tudelft.nl/.

TU Delft

Preface

This thesis is the result of my final year at the faculty of Aerospace Engineering at the TU Delft and marks the end of my time as a student. It was a challenging year, where I learned a lot about myself and the subtle art of vehicle drag reduction. When I was orienting on a subject for my master thesis research I was determined to work on something where I could apply my knowledge and skills on a practical problem. It might not seem obvious for a Flight Performance and Propulsion student to be investigating heavy duty vehicles, but looking back at the numerical analysis, the wind tunnel experiment and everything I have learned the past year, I am happy with my choice.

This brings me to my daily supervisor, Gandert van Raemdonck, who introduced me to the subject of heavy duty vehicle aerodynamics. Your knowledge of the subject has helped me a lot during this project and your enthusiasm during our meetings always ensured I walked away from them feeling motivated to keep going. Also thanks for making it possible to make those beautiful 3D printed prototypes of the guide vanes. Furthermore, I would like to thank Nando Timmer for acting as my second supervisor, even though you admitted you did not have time for it. Your practical experience and fresh view on the subject were very helpful. Finally, many thanks to Leo Veldhuis and Sander van Zuijlen for completing my thesis committee.

For me, to produce and test my drag reduction devices in the Open Jet Facility was definitely the highlight of this project. The two weeks of wind tunnel testing were intense, and I was very happy to do this together with Frank van Tilborg. I learned a lot during these weeks, so thank you for sharing the time in the wind tunnel and I hope that it helped both of us towards a successful thesis project. Also many thanks to the guys in the DEMO workshop for your tips and for producing parts of the model.

Special thanks to my family for always supporting me throughout my studies and in particular my dad for proofreading my thesis and my mom for her continuous support. Also many thanks to Anti and Marit for helping me with the design of the cover. Finally, I would like to thank my roommates and friends for always being there for me with support, advice and most importantly, welcome distractions. Not only the past year, but my whole time in Delft would not have been the same without you.

M.L. Hoogendoorn
Delft, February 2017

Summary

To limit the threat posed by global climate change, it is vital to reduce the emissions of the transport sector in the short term. A large portion of the fuel consumption of heavy duty vehicles is used to overcome the aerodynamic drag and the base of the trailer is a region where large drag reductions can be achieved. Two existing aerodynamic add-on devices for the rear-end of a heavy duty vehicle, a tail and guide vanes, are combined in an attempt to achieve a larger base drag reduction. Both these devices deflect flow into the near wake region to reduce the size of the wake and increase the base pressure.

A numerical analysis is performed using the RANS equations with the SST $\kappa - \omega$ turbulence model on a generic vehicle model (GETS). First the effect of adding a tail to the GETS model is analysed, as this serves as a baseline model to compare the guide vane configurations to. The tail reduces the drag of the GETS model with 56 drag counts, which is in accordance with previous research. If a guide vane is placed at the trailing edge of the tail, the drag contributions of the base and the tail are reduced, but this is largely counteracted by the added vane drag. For this reason the largest drag reduction is achieved if the chord of the vane, as well as the gap height is reduced to lower the vane drag. Depending on the airfoil profile, a certain incidence angle yields the largest drag reduction, which is 6° for the NACA 6415. If a guide vane with a NACA 2412 profile is placed at an 8° angle, it provides an additional drag reduction of 3 drag counts relative to the baseline model. The drag reduction that the guide vane provides at 0° yaw angle is also present if the vehicle is subjected to a crosswind.

To validate the results of the numerical analysis, a wind tunnel experiment is conducted in the Open Jet Facility. Five guide vane configurations have been produced on a 1/8-scale using a 3D-printing technique and tested in the wind tunnel together with the GETS and baseline model. In the experiment, the NACA 2412 airfoil guide vanes with an angle of 6° and 8° both yielded a wind-averaged drag reduction of 2 drag counts. The wind-averaged drag coefficients predicted by numerical and experimental analysis show good agreement. Although the drag increase with yaw angle and the drag of the GETS model show some discrepancies. The latter is attributed to the inability of the RANS simulation to capture unsteady flow phenomena and the yaw simulations might be improved by extending the mesh refinement box on the leeward side. Averaged over the 7 configurations, the numerical and experimental results of the wind-averaged drag coefficient differ just 3.9 drag counts or 1.2%.

To understand the marginal additional drag reduction that is achieved by combining a tail and a guide, the interaction between the two elements is investigated. Because the vane is operating in the deflected flow field around the tail, a component of the lift force lies in the tangential direction. Combined with the effect of the vane lift on the base and tail drag, the achievable drag reduction is nearly independent of the vane lift. As a result, the largest drag reduction is achieved when the guide vane is operating at its minimum drag condition. Taking viscous drag into consideration, it is estimated that the drag reduction can be increased to 5 drag counts if a low drag airfoil is used.

The design of the NACA 2412 8° guide vane can be fine-tuned by rounding the aft portion of the tail and shifting the vane forward, to offer a 3.5 drag count reduction relative to the baseline model. Given the drag of the full-scale baseline model, $C_T = 0.203$, this corresponds to a 1.7% drag reduction. More fine-tuning of the design can probably lead to a larger drag reduction. However, ultimately it can be concluded that combining a guide vane and a tail will at best yield around the same drag reduction as a tail elongation of the same length, which is a simpler solution.

Nomenclature

Abbreviations

2D	Two-dimensional
3D	Three-dimensional
CFD	Computational Fluid Dynamics
DC	Drag count, equal to $C_T = 0.001$
DNS	Direct Numerical Simulation
EU	European Union
GCI	Grid Convergence Index
GEM	Generic European Model
GETS	Generalised European Transport Model
GtCO_2	Gigatonne CO_2 equivalent
GTS	Generic Transport System
HDV	Heavy Duty Vehicle
HPC	High Performace Computing cluster of the faculty of Aerospace Engineering
ICCT	International Council on Clean Transportation
IPCC	Intergovernmental Panel on Climate Change
L/D	Lift to drag ratio
LES	Large Eddy Simulation
Mtoe	Megatonne of oil equivalent
NACA	National Advisory Committee for Aeronautics
NLR	Netherlands Aerospace Centre
OCI	Oil Change Initiative
OJF	Open Jet Facility
PIV	Particle Image Velocimetry
RANS	Reynolds-Averaged Navier-Stokes
RSM	Reynolds Stress equation Model
SAE	Society of Automotive Engineers
SDR	System Drag Reduction

SST Shear Stress Transport

Greek symbols

α Incidence angle with respect to x-axis

Δ Change in a parameter

δ Boundary layer thickness

δ^* Displacement thickness

ϵ Error

ϵ_n Nozzle blockage correction factor at the model

ϵ_s Solid blockage correction factor at the model

ϵ_t Total blockage correction factor

ϵ_{qn} Nozzle blockage correction factor at the nozzle

κ Turbulence kinetic energy

μ Dynamic viscosity

ν Kinematic viscosity

ω Specific turbulent dissipation rate

Φ Crosswind angle between wind vector and x-axis

Ψ Yaw angle between velocity vector and vehicle x-axis

ρ Density

σ Standard deviation

τ Shear stress

Θ Local flow angle with respect to x-axis

θ^* Momentum loss thickness

θ_r Road incination angle

ε Turbulent dissipation rate

Latin symbols

$u^\star$ Friction velocity

$\bar{C}_T$ Wind-averaged drag coefficient

$\bar{D}$ Mean drag force

$\bar{u}$ Mean velocity component in x-direction

F External force vector

v Velocity vector

a Solid blockage constant for nozzle aspect ratio

C Duplex nozzle area

c Chord

C_D Drag coefficient in vane axis system

C_f Friction coefficient

C_L Lift coefficient in vane axis system

C_p Pressure coefficient

C_S Side force coefficient

C_T Drag coefficient in vehicle axis system

C_X Vane drag coefficient in vehicle axis system

C_Y Vane side force coefficient in vehicle axis system

C_Z Vane lift coefficient in vehicle axis system

D_{aero} Aerodynamic drag force

D_{roll} Rolling resistance

e^n Amplification factor of boundary layer instability

e_a^{ij} Approximate relative error between i^{th} and j^{th} grid

F_{TR} Tractive force

g Gravitational acceleration

H Boundary layer shape factor

h Height

h_r Ride height

h_{gap} Gap height between tail and guide vane

L Length

M Moment

$M(j)$ Constant for determining wind-averaged drag coefficient corresponding to j^{th} crosswind angle

m_v Vehicle mass

n Number of crosswind angles

P Apparent order of grid convergence

p Pressure

R Radius

R_n Hydraulic radius of duplex nozzle

R_{ij} Reynolds stress in direction $_{i,j}$

r_{ij} Grid refinement factor between i^{th} and j^{th} grid

Re	Reynolds number
S	Frontal area
t	Time
u	Velocity in x-direction
u'	Fluctuating velocity component in x-direction
V	Velocity
V_m	Model volume
V_T	Tangential velocity component
V_w	Wind velocity
w	Width
x	Longitudinal coordinate
x', z'	Spatial coordinates in vane axis system
x_m	Longitudinal distance between wind tunnel nozzle and model front
x_s	Longitudinal distance from the source to the nozzle
y^+	Non-dimensional wall distance
$y_{1/2}$	Half-height of the first cell

Sub- and superscripts

exp	Experimental value
i,j	Index 1,2 or 3 in x-, y- or z-direction
m	Model
rear	Combined contributions of base, tail and vane (if present)
sim	Simulated value
t	Tail
vane	Parameter belonging to the guide vane
x	Based on longitudinal distance x

Contents

1 Introduction **1**
- 1.1 Impact of road transport . . . 2
- 1.2 Energy balance of a heavy duty vehicle . . . 3
- 1.3 Bluff body aerodynamics . . . 4
- 1.4 Rear-end drag reduction devices . . . 6
  - 1.4.1 Tail . . . 6
  - 1.4.2 Guide vane . . . 7
- 1.5 Present study . . . 8

2 Numerical set-up **11**
- 2.1 Simulation set-up . . . 11
  - 2.1.1 Governing equations . . . 11
  - 2.1.2 Turbulence modelling . . . 12
  - 2.1.3 Wall treatment . . . 13
  - 2.1.4 Solver settings . . . 14
- 2.2 Computational grid . . . 16
  - 2.2.1 Surface model . . . 16
  - 2.2.2 Computational domain . . . 17
  - 2.2.3 Meshing strategy . . . 19
- 2.3 Mesh sensitivity study . . . 21
  - 2.3.1 Mesh refinement . . . 21
  - 2.3.2 Uncertainty . . . 23

3 Numerical results **25**
- 3.1 GETS model . . . 25
  - 3.1.1 Validation of GETS simulations . . . 27
- 3.2 Baseline configuration . . . 30
  - 3.2.1 Scaled simulations . . . 30
- 3.3 Guide vane . . . 34
  - 3.3.1 Incidence angle . . . 35
  - 3.3.2 Chord length . . . 35
  - 3.3.3 Gap height . . . 36
  - 3.3.4 Airfoil variation . . . 37
  - 3.3.5 Effect of closing the tail cavity . . . 42
  - 3.3.6 Effect of yaw angle . . . 43
- 3.4 Slotted tail . . . 44

4 Experimental set-up **47**
- 4.1 Wind tunnel model . . . 47
  - 4.1.1 GETS model . . . 48
  - 4.1.2 Tail . . . 48
  - 4.1.3 Guide vanes . . . 48
  - 4.1.4 Ground board . . . 50

4.2 Measurement techniques . . . 50
4.2.1 Qualitative flow assessment . . . 50
4.2.2 Balance measurements . . . 50
4.3 Post-processing . . . 51
4.3.1 Turning disk drag . . . 51
4.3.2 Wind tunnel blockage corrections . . . 51
4.3.3 Wind-averaged drag coefficient . . . 52

5 Experimental results **55**
5.1 Set-up validation . . . 55
5.1.1 Model Alignment . . . 56
5.1.2 Reynolds sweep . . . 56
5.1.3 Drag uncertainty . . . 57
5.2 Experimental results . . . 57
5.2.1 Effect of tail . . . 58
5.2.2 Effect of guide vanes . . . 59

6 Discussion of results **63**
6.1 Validation . . . 63
6.1.1 Changes to numerical simulations . . . 63
6.1.2 Comparison between the numerical and experimental results . . . 64
6.1.3 Reflecting on initial 1/8-scale simulations . . . 68
6.1.4 Wake analysis . . . 69
6.2 Reflecting on guide vanes . . . 72

7 Conclusion and recommendations **81**
7.1 Conclusion . . . 81
7.2 Recommendations . . . 83

Bibliography **85**

1

Introduction

In 2015, the Paris climate agreement voiced the worldwide intent to respond to the global threat of climate change by limiting the temperature rise this century to $2°C$ above pre-industrial levels, pursuing efforts to limit the rise to $1.5°C$. It is believed that a higher temperature rise will significantly increase the chance of irreversible changes to the climate, with the the risk of food and water shortage, floods, extreme weather events and more. The agreement was signed by every eligible state worldwide and to date has been ratified by 170 states [63], together representing 87% of global greenhouse gas emissions. In the fifth assesment report of the Intergovernmental Panel on Climate Change (IPCC) published in 2014 [14], it was estimated that the remaining global carbon budget to have a 50% chance of achieving the ambitious target of limiting temperature rise to $1.5°C$ is 550 GtCO_2. Meinshausen et al. warned in Nature magazine that burning the currently available fossil fuel reserves in mines and fields would well exceed this budget. [39] Given the current annual emission rate of 39.2 GtCO_2 and the emissions to date, the global carbon budget would be exhausted as early as 2025. The Oil Change Initiative [43] predicted scenarios with a chance of achieving these climate goals. In all these scenarios there should be a peak in emissions in the coming years followed by a steady decline, as can be seen in figure 1.1. This signifies the need to take immediate action to reduce carbon emissions in the short term. This chapter will focus on the role that aerodynamic drag reduction of heavy duty vehicles (HDV's) can play in reducing greenhouse gas emissions.

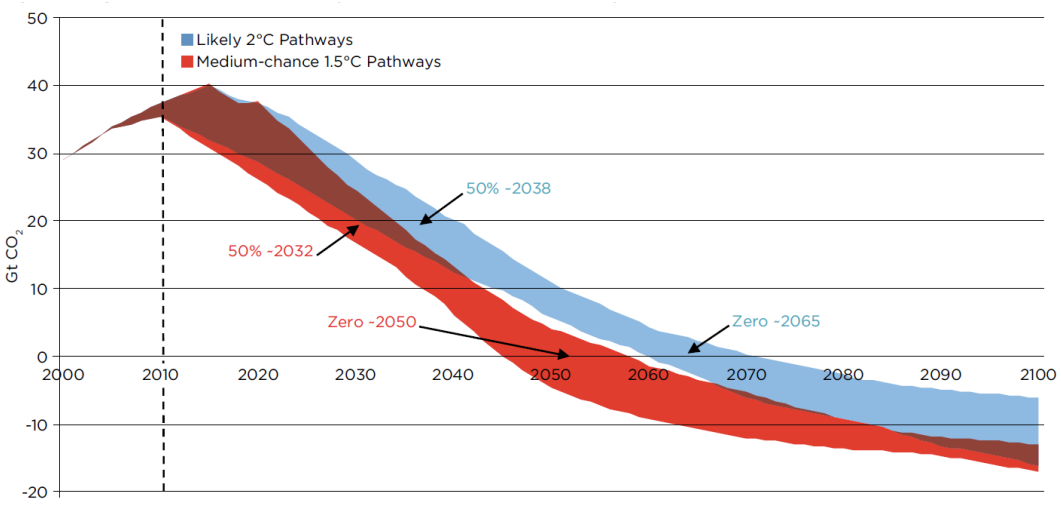

Figure 1.1: **Range of global emissions pathways in scenarios consistent with a 66% chance of $2°C$ or 50% chance of $1.5°C$ temperature rise above pre-industrial levels. Source: OCI [43]**

1.1. Impact of road transport

It is evident that greenhouse gas emissions of all sectors should reduce in order to reduce the risks that are related to global climate change. However, this is in conflict with the ever growing need for transport. Therefore it is vital to greatly reduce the impact of transport on the environment for sustainable growth to be possible. Long-term mitigation scenarios in accordance with the Paris agreement require zero emissions in the second half of the century. [43] For the transport sector this could be achieved by having solely electric vehicles powered by renewable energy, assuming that the production of these vehicles also occurs emissionless. The past months have shown some promising developments in that direction with both Daimler [15] and Tesla [59] presenting fully electric truck designs. However, it will take a long time to replace the current truck fleet with electric vehicles, so to initiate a decline in emissions in the coming years, add-on drag reduction devices offer a good solution in the short term.

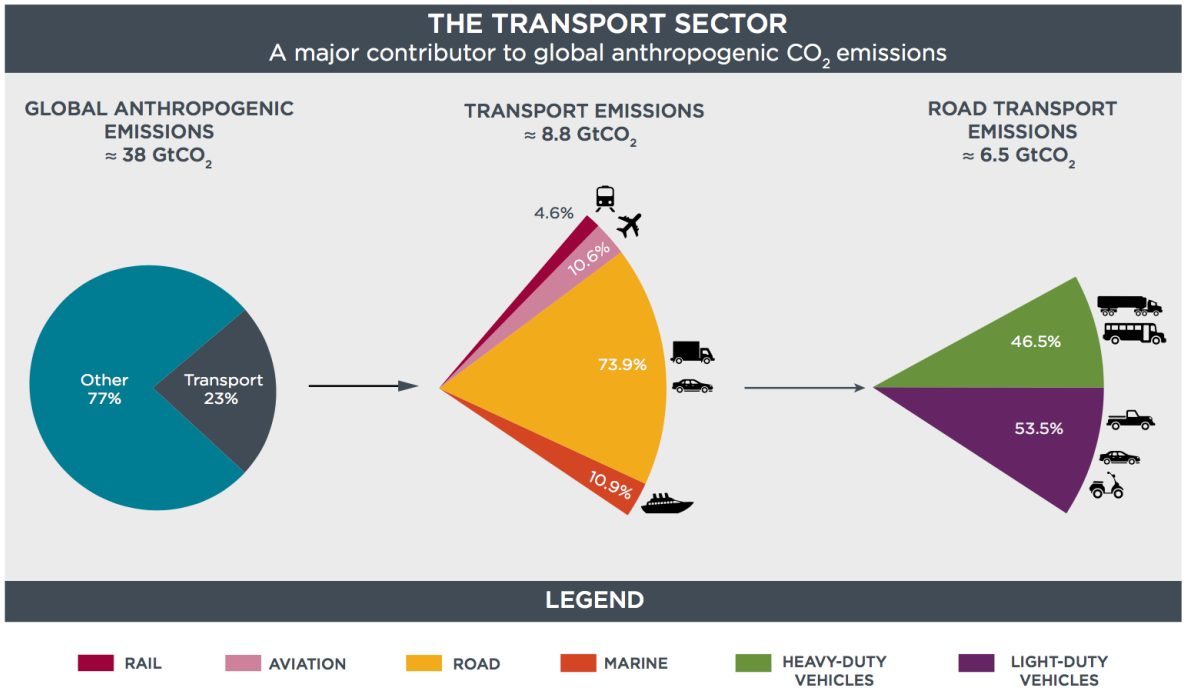

Figure 1.2: **Global transport sector lifecycle CO2 emissions, 2010 Source: ICCT [41]**

The transport sector is an ever-growing market and can be considered as indispensable to modern society. Driven by the demand for goods from all over the world, the versatile and efficient road transport network will continue to grow for years to come. In 2015 approximately half of all goods in the European Union (EU) were transported via road. [19] The impact of road transport on the environment as well as the economy is huge. According to Eurostat [20], from 1990 to 2006 the energy consumption of road transport in the EU grew at an annual rate of 1.6%, to reach 303.3 Mtoe in 2006. To put this into perspective: This was approximately a quarter of the total energy consumption in the EU. Globally the transport sector is responsible for 23% of anthropogenic CO_2 emmisions as can be seen in figure 1.2. Trucks and busses are responsible for 34% of the CO_2 emissions in transport globally, at around 3 GtCO_2. [41] Apart from the impact on the climate there is also the influence of HDV's on the local air quality, which has caused older trucks to be banned from some city centres. As the need for transport will only increase in the coming decades, improving the fuel efficiency of the road transport fleet is vital for achieving sustainable growth. For the transport industry itself, the economical considerations are probably a larger incentive than the environmental impact of transport. Given that 30% of the total operating costs of a truck are spent on fuel, financially there is also a strong incentive to increase fuel efficiency of HDV's. A typical European long-haul truck drives around one million kilometres in its first

life span of four to six years. [65] For this reason even a small reduction in fuel consumption can yield huge savings for transport companies and reduction in CO_2 emissions. Looking at the energy balance of an HDV can reveal the influence that improving the aerodynamics can have on the fuel consumption.

1.2. Energy balance of a heavy duty vehicle

HDV's operate in a wide variety of operating conditions with changing velocities, wind conditions, turns and inclinations. Most of the operational time, however, is spent cruising with constant velocity at highway velocities and this is where the largest fuel efficiency improvement can be made. In general the required engine power during operation of an HDV consists of three main contributors, namely the power related to:

- Accelerating the vehicle and to overcome differences in height
- Rolling resistance
- Aerodynamic drag

The first term is related to the kinetic and potential energy of the system and is for a large part influenced by the driving style, selected route and traffic. When driving on the highway with a constant velocity, this term should be small. The rolling resistance between the tires and the road surface depends on the weight of the vehicle and the tire friction coefficient, which varies with driving velocity and tire type. Lowering the power required to overcome the aerodynamic drag is what is attempted in this thesis. The total required tractive power is $P_{TR} = F_{TR}V$. The the tractive force F_{TR} is defined by Sovran and Bohn [56] as follows:

$$F_{TR} = m_v \frac{dV}{dt} + Mg \sin\theta_r + D_{roll} + D_{aero} \tag{1.1}$$

This required power is to be delivered by the engine through the crankshaft. To arrive at the fuel that is consumed by the engine, one needs to consider some losses that occur due to friction in the engine, clutch, gearbox and axles and power consumed by auxiliary devices. A much larger part of the available energy in the fuel is lost in the form of waste heat in the combustion process. According to Wood [73] ground vehicles use approximately 50% of their energy overcoming aerodynamic drag. Road tests on a semi-truck were performed by van Raemdonck and van Tooren [66], which revealed that at highway velocities 39% of the delivered engine power is used to overcome the aerodynamic drag. The rolling resistance was responsible for 47% and the remaining 14% was attributed to mechanical losses. Furthermore it was found that the average fuel consumption over a six week period was approximately 30 l/100km.

In general the aerodynamic drag of a bluff body is dominated by pressure rather than friction drag and for HDV's the pressure drag contribution can be as large as 90% [73]. As can be seen in figure 1.3, this is a much larger fraction than for subsonic aircraft where pressure and friction drag are of similar magnitude. The pressure drag of HDV's is caused by a high pressure region in front and a low pressure region behind the vehicle. The vehicle is dragged back by the low pressure on the rear surface, which is caused by the recirculation area behind the vehicle. For a bluff body with a rounded front edge this base pressure is the main contributor to the pressure drag.

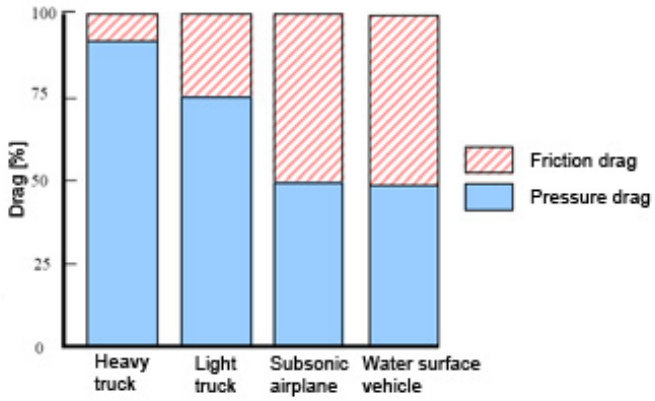

Figure 1.3: **Friction and pressure drag contributions of various vehicles. Source: Wood [73]**

1.3. Bluff body aerodynamics

From an aerodynamic perspective, trucks and road vehicles in general can be described as bluff bodies in close ground proximity. As opposed to aircraft, the shape of road vehicles is primarily determined by functional, economical and aesthetic requirements, while aerodynamic shaping is a secondary design activity according to Hucho.[29] In the case of HDV's, the shape can be said to be fully determined by functional requirements, combined with regulations regarding maximum length, width and height. To maximise the loading capacity, HDV's have a large cross sectional area and an untapered shape, which results in a large region of separated flow at the rear-end.

Boundary layer

The flow field around vehicles is characterized by thick, turbulent boundary layers. In the case of aircraft aerodynamics often laminar boundary layers are present over at least part of the surface. For various reasons this is not the case for road vehicles. First of all road vehicles generally drive in close proximity and therefore move through turbulent wake flows. Furthermore there are many geometric disturbances on the exterior of the vehicle like gaps, ridges and inlets that cause the boundary layer to transition. It is also not uncommon for road vehicles to also have areas of separated flow followed by reattachment of the boundary layer, for example between the cabin and trailer of HDV's. After reattachment the boundary layer will always be turbulent and thicker. As a result, when looking at the rear-end of an HDV, it can be expected that the boundary layer is turbulent. This implies that flow control methods that rely on forcing boundary transition to achieve a drag reduction, such as the zigzag-strips for speed skaters developed by Timmer and Veldhuis [60], will not have an effect on the rear-end of an HDV.

Near wake

At the rear of a bluff body is generally a large region of separated flow, referred to as the near wake. The square trailing edge of a truck gives it a fixed separation point, as opposed to, for example, a sphere where the separation point moves freely depending on the flow conditions. When looked upon from the side, the wake of a road vehicle generally consists of a large recirculation area with two counter rotating vortices, as is visible in figure 1.4. Due to the proximity of the ground, some asymmetry between these two vortices might be present. As HDV's are 3D bodies with a very low aspect ratio, the flow field will be 3D as well, meaning that the flow in the near wake is rotational in all directions. In case of an HDV, this means what the 3D wake contains a ring shaped vortex. Much academic research in the field of bluff body aerodynamics is performed on 2D bluff bodies. This has resulted in a number of flow control applications for the drag reduction of 2D bluff bodies that introduce a span-wise disturbance to risrupt the vortex shedding behaviour. Examples are a segmented trailing egde [49], a wavy trailing edge [61] [10], a wavy front stagnation surface [8] or vertical tabs [47]. Changing the flow structure in the wake

of a bluff body using splitter plates [7] and a multi-cavity [37] has also only been proven effective for 2D bluff bodies. This research is very insightful, but these effects do not necessarily translate to the 3D case. Therefore drag reduction strategies that are effective for 2D bluff bodies, might be ineffective when applied to road vehicles.

Further adding to the complexity of the flow field around road vehicles are rotating wheels, geometric details and cavities. This all ultimately leads to a flow field that is inherently turbulent, unsteady, highly rotational and dominated by separated flows. Therefore the vehicle drag and flow field in numerical simulations and controlled wind tunnel experiments that require simplified models can deviate greatly from full scale HDV's

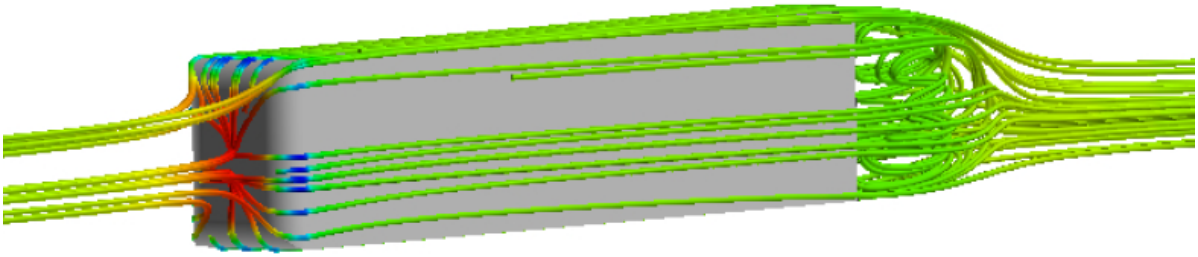

Figure 1.4: **Streamlines around the GETS model. Source: van Leeuwen [64]**

Drag sources

When looking at a typical long-haul truck, which is a semi-trailer truck, there are a number of area's that produce a large amount of drag: There is the high pressure area at the front of the tractor, the gap between tractor and trailer and the low pressure area's at the rear of the tractor underneath the trailer and the rear-end of the trailer respectively. A graphic representation of these drag sources with indicative drag values is given by Wood and Bauer [74] in figure 1.5. The distribution of drag is slightly different for European style trucks compared to the 'conventional' North-American truck shown in figure 1.5. Hjelm [27] notes that in the European Union maximum dimensions exist for the tractor-trailer combination as a whole, whereas in the United States these restrictions only apply to the trailer. This has led to the compact cab-over-engine configuration to become the standard in Europe, unlike the 'conventional' tractors with the engine in front of the cabin, as seen in the United States. The more compact cab-over-engine trucks, have a larger front stagnation surface and benefit less of the thrust force over the curved top part of the cabin, which leads to a larger drag contribution of the front part. Due to the different length restrictions European trucks generally have a smaller tractor-trailer gap, which reduces the drag produced by the gap at the expense of a larger turn radius.

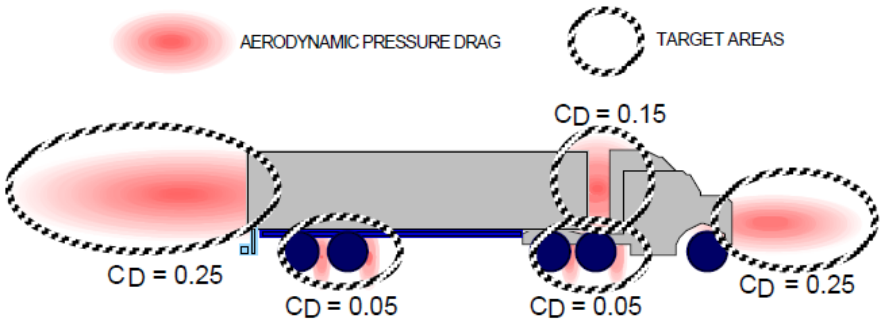

Figure 1.5: **Visualisation of drag sources on a semi-truck operating in a crosswind Source: Wood and Bauer [74]**

Nowadays for each of the regions in figure 1.5 drag reduction devices are commercially available or included by standard in the design of new trucks. The front of the tractor has seen many improvements in the form of rounded corners, cornering vanes and aerodynamic mirrors. These modifications try to transfer the air from the front to the side of the tractor with minimum disruptions. It was argued by Leuschen and Cooper [36] that the external mirrors could be removed and replaced by camera's to lower the drag, which is featured in Tesla's [59] design of a fully electric semi-truck. The airflow is guided past the gap between tractor and trailer by extender plates mounted to the sides of the tractor. If the front of the trailer is exposed to the airflow due to a height difference between tractor and trailer, the flow is guided to the top of the trailer by a roof deflector. Various types of roof deflectors were tested by Watkins et al. in 1993 [71] in a comparison of wind tunnel and road tests and today they are found on the majority of trucks. Van Raemdonck [65] did a thorough investigation of the sources of drag on heavy duty vehicles and identified the area behind behind the tractor, on the underside of the trailer as a large contributor. He found that this can be reduced by preventing the airflow to reach this area by mounting plates to the sides of the trailer. These plates have been developed into SideWings by Wabco Optiflow [69] that can save up to 1.5 l/100km at highway speeds and are shown in figure 1.6

1.4. Rear-end drag reduction devices

Leuschen and Cooper [36] tested many different drag reduction devices on a full-scale tractor-trailer in the wind tunnel. They stated that the large region of separated flow at the rear of a trailer is the largest untreated source of drag on a modern tractor-trailer. That is why this thesis research focusses on reducing the base drag of HDV's.

Some add-on devices for the rear-end of HDV's exist that create vortices just before the trailing edge to reduce the base drag. Examples are the commercially available Airtab vortex generator [1] and the VorBlade trailer wing system [5] which combines vortex generators and a guide vane like function into one device. Wood [74] performed road tests on larger vortex strakes to introduce vorticity and reduce the base drag and an undercarriage device to direct flow into the wake. Some rear-end devices feature flat plates with a certain offset from the sides of the trailer as researched by Khalighi et al. [32] and Gilliéron and Kourta [25]. Also some research has been performed on active flow control applications to reduce the base drag. Examples are the work of Nayeri et al. [44] on both boundary layer blowing and suction in combination with a tail. Van Leeuwen [64] showed that blowing over a tail can be enhanced by employing the Coânda effect using curved tail panels. Also fluidic oscillators [54] and combined suction and oscillatory blowing actuators [55] have been shown to be capable of reducing the base drag.

However, these active flow control applications are still under development to reduce the energy consumption of the control itself. This makes the best performing add-on devices for the rear-end of HDV's that are currently available the boat tail and guide vanes. Both these devices reduce aerodynamic drag by reducing the size of the wake and increasing the base pressure. The topic of this thesis is to improve the drag reduction achieved by such a tail by combining it with a guide vane. Therefore it is important to understand the working principle of both these drag reduction devices, which will be discussed in more detail in the subsequent subsections.

1.4.1. Tail

An effective way to reduce the drag at the rear-end of an HDV is by mounting plates to the sides of the base to form a tapered elongation, or a boat tail. To be effective, the plates should be angled such that the flow is able to follow the geometry and not separate before the trailing edge. If the slant angle of the tail is too large, the flow will separate before the trailing edge and its effect will be reduced. If the boat tail is designed correctly, the wake behind the HDV will be narrower and further away from the base, resulting in a higher base pressure and consequently lower pressure drag. The panels of the boat tail

form a cavity that captures the vortices in the wake, stabilising the flow and reducing the drag.

Apart from the slant angle, the length of the tail is an important design parameter. If the tail is longer, a larger taper ratio can be achieved with the same slant angle. Therefore a longer tail leads to a larger pressure recovery over the surface and moves the vortical structures further away from the body, increasing the base pressure. Van Raemdonck [65] showed that a longer tail improves the efficiency of the tail with yaw angle compared to a shorter tail. He also investigated the effect of several design variations, such as closing the cavity, curved panels and removing the bottom panel. All of these modifications resulted in lower drag reductions than the standard tail with flat plates on all four sides. When the flow separates over a part of the tail due to a too large slant angle, the additional surface of a longer tail provides a larger surface for the low pressure to act on. Schmidt et al. [54] showed that for certain slant angles the tail increases the drag compared to a baseline configuration and that this effect grows with the length of the tail. Until recently maximum length regulations made adding a tail add-on device to a trailer unattractive. In the European Union maximum dimensions exist for the tractor-trailer combination as a whole, which has led to the compact cab-over-engine configuration to become the standard. [27] The current tractor-trailer fleet is sized to these maximum dimensions to maximise loading capacity. This means that adding a tail to the rear-end would require a shorter trailer, reducing the vehicle load capacity and threatening the economic equilibrium of the road transport sector. Therefore in 2015 legislation was passed [18] to allow for aerodynamic devices at the trailer rear-end to exceed the maximum length with 500mm, with even longer aerodynamic devices requiring type-approval. Therefore it is desirable to achieve the highest possible drag reduction within this 500mm length requirement. Applying flow control, such as the guide vanes researched in this thesis, could be an attractive method to increase the performance of the tail without increasing its size.

A practical restriction is that the tail panels should be able to fold away and not obstruct docking and loading operations. A final aspect of tails on HDV's that is important to consider is the transition between trailer and tail. If there is an offset between the trailer and the tail, a separation region may form over the tail, reducing its efficiency. For practical reasons this can not be avoided for the bottom plate of the tail, as otherwise the rear doors are no longer accessible. Fig. 1.6 shows a semi-trailer truck with commercially available SideWings and tail. It can be seen that the bottom plate is removed completely such that the door handles and folding mechanism of the tail is still accessible. According to the manufacturer [69], this tail provides up to 1.1 l/100km savings at highway speeds and can reduce CO_2 emissions up to 2.8 tonnes per trailer per year. The tail design shown in figure 1.6 will be used as a baseline in this thesis. This tail has a length of 0.5m and a slant angle of $12°$. In this study no geometric details are included, so the tail is simply modeled as three rectangular flat plates that form the tapered elongation.

1.4.2. Guide vane

As early as the year 1933 Frey [21] investigated the effect of guide vanes on the drag of 2D bluff bodies. Both single and multi-element airfoils were placed on the trailing edge of various 2D bluff shapes and drag reductions were recorded. Much later, a numerical study was performed at the TU Delft by Jabobs [30] on the drag reduction of a 2D backwards facing step using guide vanes. Later the guide vane concept was applied to an HDV shape by van Straaten [67] in a computational and experimental analysis. He investigated guide vane designs with various airfoil profiles, positions and inclinations on the trailing edge of a generic American style semi-truck model. It was shown that the guide vanes could reduce the base drag by both moving the reattachment point closer to the base and increasing the pressure in the vortex cores in the wake . Ultimately a drag reduction of 21.3% was recorded in the wind tunnel using a NACA 4415 shaped guide vane. More numerical simulations on design variations of this guide vane design indicated the more cambered NACA 6415 airfoil to be even more effective. Based on these results, a full-scale version of these guide vanes was developed by van Raemdonck [65] and subjected to extensive road testing on a semi-truck. With guide vanes

Figure 1.6: **Truck fitted with commercially available tail and SideWings Source: Mercedes Benz [40]**

mounted on all four sides of the trailer base, maximum fuel savings of 0.90 l/100 km were found in circuit tests. It was shown that the effectiveness greatly depends on the boundary layer development, which in the circuit test greatly depended on the driving direction and the resulting crosswind angle and velocity. Therefore an active control strategy for the vane positions is suggested. A drag reduction method similar to the guide vanes is employed by a commercially available device named System Drag Reduction (SDR) mounted to the trailer top edge. The SDR device also forces the flow to be deflected inwards, but has a smaller offset from the trailing edge compared to the guide vanes and is equipped with slots. Van Raemdonck also performed circuit tests on the SDR device and recorded fuel savings of 0.28 l/100 km. Fig. 1.7 shows guide vanes mounted at the rear of a wind tunnel model and an SDR system installed on the rear-end of a trailer.

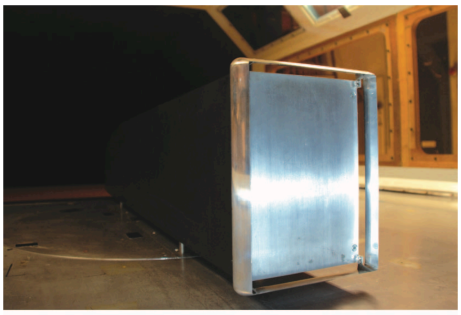

(a) Guide vanes. Source: van Straaten[67]

(b) SDR device installed on a truck trailer. Source: JOST SDR [31]

Figure 1.7: **Two uses of guide vanes to reduce the near wake size**

1.5. Present study

In the previous sections it has been identified that there is a need to reduce the CO_2 emissions by HDV's in the short term. A large portion of the fuel consumption of HDV's is used to overcome the aerodynamic drag and the base of the trailer was identified as a region where large drag reductions can be achieved.

Two drag reduction devices exist that reduce the base drag of a semi-trailer by reducing the size of the near wake: the tail and guide vanes. This thesis aims to combine these devices into a single, more efficient drag reduction device, as visualised in figure 1.8. Therefore the research goal of this thesis project is to: ”Improve the base drag reduction achieved by a heavy duty vehicle tail by combining it with a guide vane.” It is believed that by using a scientific approach combining numerical simulations and scaled wind tunnel experiments, a design can be found that can improve the performance of these tails within the scope of a thesis project. The numerical simulations are used to analyse many different design variations in order to identify the potential drag reduction that can be achieved. Next an experimental analysis in the wind tunnel is performed to validate the computational results. This will provide an answer to the following research question:

What is the effect of combining a tail and a guide vane on the drag coefficient of a bluff body?

This research question can be divided into a number of sub-questions that will be addressed in this thesis:

- How is the base drag of a bluff body affected by combining a tail and a guide vane
- What interaction effects between the tail and the guide vane can be identified?
- How can the design of the guide vane be altered to yield the largest drag reduction?
- To what extent is a method combining numerical simulations and a scaled wind tunnel experiment capable of designing a drag reduction device for a heavy duty vehicle?

The next chapter describes the numerical set-up that was used to analyse the drag reduction solutions, followed by the numerical results in chapter 3. The experimental set-up that was used during the wind tunnel test is presented in chapter 4. The experimental results are given in chapter 5. Next in chapter 6 the numerical and experimental results are compared and a reflection on the concept of combining guide vanes and a tail will be given. Finally in chapter 7 conclusions and recommendations regarding this research will be stated.

Figure 1.8: **Concept of combining a HDV tail and a guide vane. Source: Edited from Wabco [69]**

2

Numerical set-up

The largest part of the research in this thesis project is performed using Computational Fluid Dynamics (CFD). This chapter will elaborate on the methodology that is used to perform these numerical simulations. In this research the commercially available software package Fluent by ANSYS was used with the associated meshing software. First in section 2.1 the set-up of the simulations in terms of the system of equations and solver settings that were used will be discussed. Next the steps that were taken to create the computational grid in the flow domain surrounding the surface model will be described in section 2.2. Finally in section 2.3 the results from the mesh sensitivity study will be presented.

2.1. Simulation set-up

2.1.1. Governing equations

At the basis of virtually all CFD simulations are the Navier-Stokes equations. These equations will not be derived here as that would be too long for the scope of this thesis report and the derivation can be found in standard aerodynamics textbooks like the work of Anderson. [3] However, it is important to know the theoretical basis of these equations and what the associated problems and shortcomings can be. The Navier-Stokes equations are derived from the concept of continuity of mass, momentum and energy in a fluid. To arrive at the most common form of the Navier-Stokes equations these continuity relations need to be combined with the assumption of a viscous Newtonian fluid. If the flow is assumed to be incompressible, which is acceptable for the flow conditions of HDV's, the Navier-Stokes equations can compactly be stated as in equation (2.1).

$$\frac{\partial \mathbf{v}}{\partial t} + (\mathbf{v} \cdot \nabla)\,\mathbf{v} = -\nabla p + \nu \Delta \mathbf{v} + \mathbf{f}(\mathbf{x}, t) \tag{2.1}$$

As $\mathbf{v}$ is a vector containing the three unknown velocity components, this describes the conservation of momentum in each direction as a function of the pressure, viscous stress and $\mathbf{f}(\mathbf{x}, t)$ which is some external force. To solve this system of equations for the three unknown velocity components and the pressure, also the continuity equation needs to be considered:

$$\frac{\partial \rho}{\partial t} + \nabla\,(\rho \mathbf{v}) = 0 \tag{2.2}$$

Which in the incompressible case simplifies to:

$$\nabla \mathbf{v} = 0 \tag{2.3}$$

In the case that heat transfer is present in the system, the energy equation is required to close the system of equations, but that will not be considered in this thesis report.

2.1.2. Turbulence modelling

The challenge in solving the Navier-Stokes equations lies in the modelling of turbulence. It is possible to solve the Navier-Stokes equations without a turbulence model, which is known as Direct Numerical Simulation (DNS). In this method the flow is resolved using the Navier-Stokes equations on all turbulent length scales. For moderate to high Reynolds number flows such as those around HDV's this would require a very fine grid. Generally this leads to computational requirements are too high, especially in a design context. DNS has been successfully applied to simulate the flow around bluff bodies, such as the work by Cai. [10] In practice to solve the Navier-Stokes equations for high Reynolds number flows the computational requirements need to be lowered, for which two methods can be applied; filtering and Reynolds decomposition.

Filtering

This necessity of an extremely fine grid can be partially resolved by applying a space filtered method called Large Eddy Simulation (LES). In LES the lower length scales are discarded by filtering out eddies smaller than the grid size. This can be successfully applied to bluff bodies with moderate Reynolds numbers, as was shown by Krajnovic [33] in a study of passive flow control over an Ahmed body. However, LES still requires a relatively fine grid and therefore a significant computational effort, which is not always acceptable within a design context. To further lower the computational requirements, Reynolds decomposition can be applied.

Reynolds decomposition

In this simplification of the Navier-Stokes equations the velocities are divided into a mean and a fluctuating component. This can be expressed as:

$$u(\mathbf{x}, t) = \bar{u}(\mathbf{x}) + u'(\mathbf{x}, t) \tag{2.4}$$

When this decomposition into mean and fluctuating components is applied to all flow variables and they are substituted back into the general Navier-Stokes equations and averaged over time, the Reynolds-Averaged Navier-Stokes (RANS) equations are obtained. It should be noted that the ensemble averaging procedure to arrive at the RANS equations does not necessarily mean that the solution is steady state. It is possible to solve the unsteady RANS equations to find a transient solution of the flow over a body. However in this thesis the focus is to reduce the drag of HDV's driving on the highway at constant velocity. Therefore the flow is assumed to be independent of time. Because of the Reynolds decomposition six additional terms appear in the RANS equations compared to equation (2.1). These terms are the Reynolds stresses and are defined as $R_{ij} = -\rho\overline{u_i' u_j'}$. Since the second-order Reynolds stress tensor is symmetric, there are six unique terms: three normal stresses (e.g. $u_1' u_1'$) and three shear stresses (e.g. $u_1' u_2' = u_2' u_1'$). [51] The incompressible, steady-state RANS equations, that form the basis of the numerical simulations in this thesis project are given in equation (2.5).

$$\frac{\partial}{\partial x_j}\left(\rho \bar{u}_i \bar{u}_j\right) = \frac{\partial \bar{p}}{\partial x_j} + \frac{\partial}{\partial x_j}\left(\bar{\tau}_{ij} - \rho\overline{u_i' u_j'}\right) \tag{2.5}$$

Closure problem

Where the general Navier-Stokes equations are a closed set of equations, the addition of the Reynolds stresses to the RANS equations require additional relations for closure. This requires modelling of the turbulent stresses, which is one of the central problems of CFD. There are many different turbulence models available, that provide closure with a varying number of equations. For example, there are

turbulence models that complete the system with one (Spalart-Allmaras), two ($\kappa-\varepsilon$, $\kappa-\omega$, V^2F) or seven (RSM) additional equations. The choice of a certain turbulence model depends on many aspects, such as computational resources, Reynolds number, required accuracy and the type of flow (separated regions, rotational flow, free shear layers). For the computational analysis of a generic HDV model it was shown by Pointer et al. [50] that the Shear Stress Transport (SST) $\kappa-\omega$ gave the highest accuracy compared to other two-equation turbulence models. Also numerous other master thesis projects within the department have succesfully made use of the SST $\kappa-\omega$ model, like Nouwens, [45], Mulkens, [42], Gheyssens [24] and Kruijssen. [34]

In contrast to the seven equation RSM turbulence model, which determines the turbulence in each direction separately, the two-equation $\kappa-\varepsilon$ and $\kappa-\omega$ models assume an isotropic eddy viscosity. This can lead to artificial diffusion if isotropic turbulence is imposed on a highly anisotropic flow field such as a recirculating wake. However, given the successful application of the SST $\kappa-\omega$ model in prior work and the additional computational requirements that the RSM model imposes, the SST $\kappa-\omega$ model was selected for this research. This model combines the $\kappa-\varepsilon$ and $\kappa-\omega$ models using a blending function. This entails that the $\kappa-\omega$ model is activated in the near-wall region, whereas a transformed formulation of the $\kappa-\varepsilon$ model is used in the far field. [4]

2.1.3. Wall treatment

In order to analyse the aerodynamic performance of vehicles, it is important to accurately model the behaviour of the flow close to the wall. The presence of a no-slip condition at the wall induces a boundary layer in which the flow is highly dependent on viscous effects. Simulating the flow in the boundary layer region requires special attention as the previously stated governing equations cannot plainly be applied there. When considering wall flows, the non-dimensional wall distance y^+ is used as the coordinate perpendicular to the wall, which is defined as:

$$y^+ = \frac{yu^\star}{\nu} = \frac{y\sqrt{\tau\rho}}{\mu} \tag{2.6}$$

Based on the value of y^+ the turbulent boundary layer can be divided into several regions where different flow phenomena are dominant, as can be seen in figure 2.1. The region closest to the wall, the inner layer where $y^+ < 50$, is dominated by viscous effects rather than the freestream flow. Inside this inner layer is a viscous sub-layer for $y^+ < 5$ where the flow is almost linear and the velocity profile is linear according to the 'law of the wall'. In the outermost region of the boundary layer the flow is fully turbulent. In the overlapping region between these to layers the flow can be approximated using von Kármán's logarithmic law.

For CFD simulations the significance of these various regions inside the boundary layer and the associated y^+ values is that there are two approaches of modelling the flow close to the wall: near wall modelling and wall functions. The first method is to resolve the flow all the way up to the wall using the governing equations and turbulence model. This requires the first layer of cells to cover the viscous sub-layer. This requires $1 < y^+ < 5$, which can result in an excessively fine grid for high Reynolds numbers. For this reason the second approach does not resolve the flow in the inner region, but uses semi-empirical relations (wall functions) such as the log-law to model the flow close to the wall. This requires y^+ to be between 30 and 300 and therefore poses a much less strict requirement on the grid size. In Fluent 'enhanced wall treatment' is applied automatically when the SST $\kappa-\omega$ model is used. In this method wall functions are used, but when the value of y^+ is small enough to resolve the flow up to the viscous sub-layer, near wall modelling is activated. The implications of near wall modelling on the generation of the computational grid will be discussed in subsection 2.2.3.

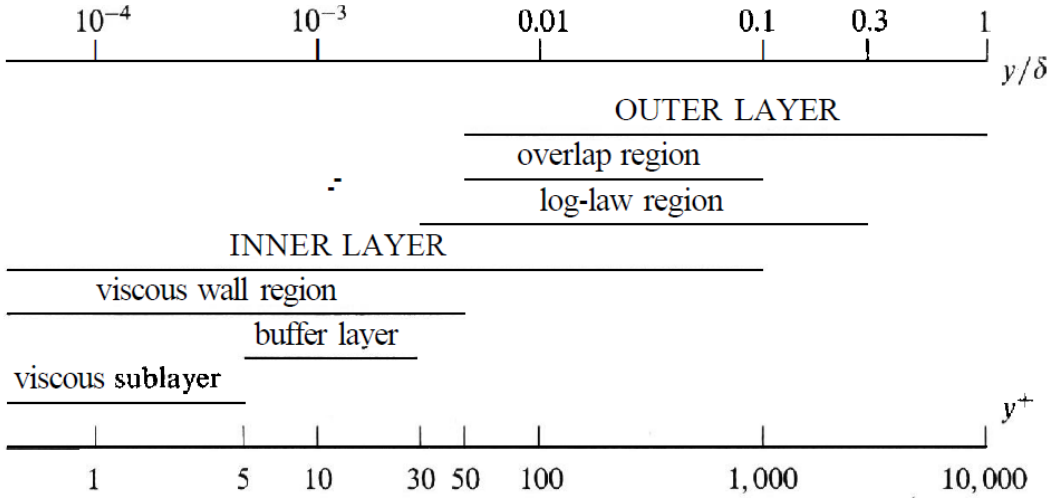

Figure 2.1: **Schematic of layers within the turbulent boundary layer Source: Pope [51]**

2.1.4. Solver settings

The Fluent package offers the choice between a pressure and a density based solver. Originally the first was developed for low-speed, incompressible flows and the latter for high-speed, compressible flows. However, according to the theory guide [4] nowadays both can be used for a wide range of flow conditions beyond their traditional or original intent. Still, the pressure-based solver is used in this research because of the low flow velocities. There are two types of algorithms available for the pressure-based solver. A segregated algorithm that solves each momentum and continuity equation sequentially in an iterative process and a coupled algorithm that solves the entire system of equations at once each iteration. The coupled algorithm was selected as it requires less iterations to converge to a solution, although it uses more memory. This was not an issue as the simulations were performed on the High Performance Computing (HPC12) cluster of the faculty of aerospace engineering. Derivatives and gradients are computed using the Green-Gauss node-based approach, as this method is more accurate on unstructured meshes and better at dealing with highly skewed cells.

Before the simulation is started, an initial solution is determined as a starting point of the iterative process. This is done using the hybrid initialization option which performs ten quick potential flow iterations to ensure a smooth flow field that adheres to all boundary conditions. Next the simulation is started by performing 150 iterations using a first order upwind spatial discretization scheme for momentum, turbulent kinetic energy κ and specific dissipation rate ω to reduce the chance of the solution diverging. After the first 150 iterations the spatial discretization is changed to a second order upwind scheme for these variables. It was determined that a total of 2000 iterations were sufficient to converge the residuals to a value below 10^{-4}, several orders of magnitude lower than the starting residual, which is an indication of good convergence according to SAE J2966. [53] An example of the convergence history of the residuals is shown in figure 2.2. Furthermore, the convergence of the drag coefficient was investigated. Fig. 2.3 shows the convergence history of the total drag coefficient of the baseline model at various yaw angles. It can be seen that the drag converges to a steady value, but to eliminate any small oscillations, all force coefficients in this report are averaged over the last 500 iterations. All simulations were performed on the HPC12 cluster. The computational times were in the order of 6-7 hours when running on 8 cores, which was deemed acceptable.

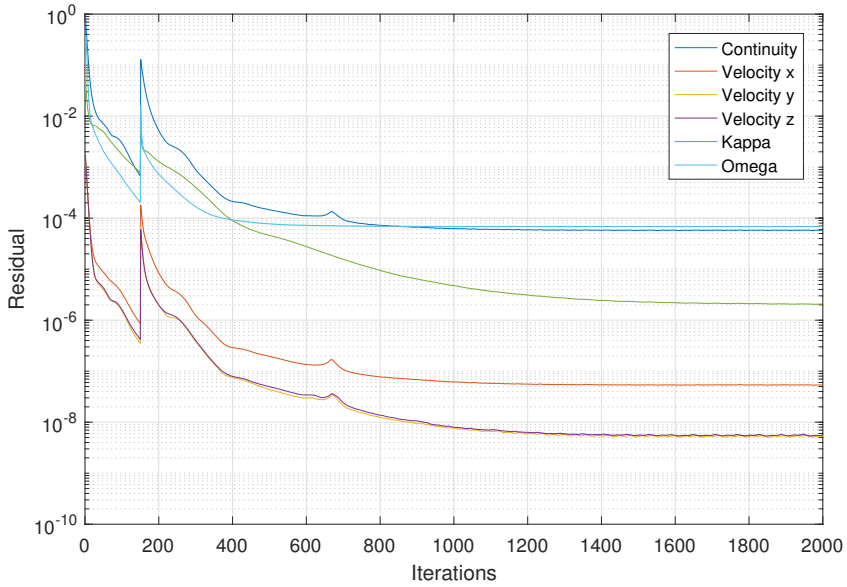

Figure 2.2: **Convergence history of residuals for 1/8 scale GETS model with tail**

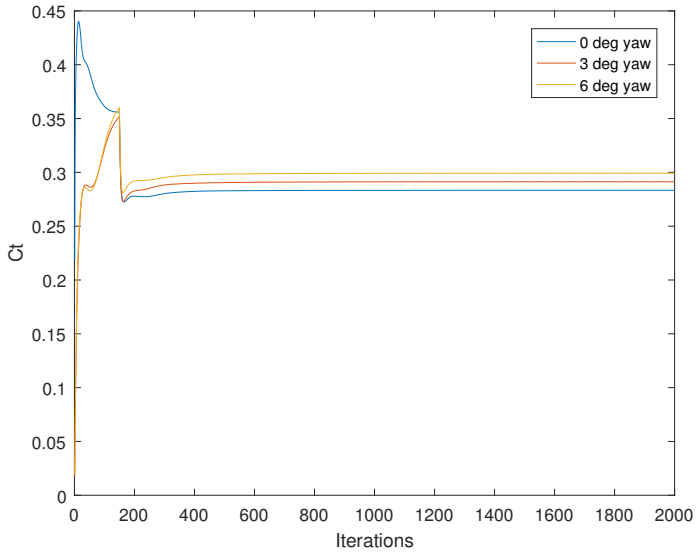

Figure 2.3: **Convergence history of the total drag coefficient of the 1/8 scale GETS model with tail at various yaw angles**

2.2. Computational grid

The Fluent solver uses the finite volume method to solve the RANS equations. This means that the computational domain is split up into many discrete volume elements at which the governing equations must be satisfied. In order to create these elements a surface model of the HDV is required around which an enclosing volume of air is created. Close to the walls of the model a number of inflation layers is extruded to accurately model the boundary layer. It is essential to carefully construct this computational grid as this influences the quality of the solution as well as convergence.

2.2.1. Surface model

A real tractor-trailer combination has many geometric details, interior flow channels and moving parts and it is the choice of the CFD analyst how many details to include in the numerical simulation. Ultimately this is a trade-off between the required accuracy of the simulation and the available computational time. As this is a design study of a drag reduction device, many different configurations need to be simulated and therefore a simplified model with only the generic shape of a HDV has been selected. A number of generic HDV models have been used in aerodynamic research such as the Generic Transport System (GTS) [57] [67], Generalised European Transport System (GETS) [64] [65] [16] [24] and Generic European Model (GEM) [42] [34]. The main difference between the GTS and the GETS model is that the latter is based on a typical European tractor-trailer combination with a 'square' cabin front, whereas the GTS model has a sloped roof resembling an American style tractor. The GEM model is a derivative of the GETS model, but includes a distinct tractor and trailer with a gap and generic wheel shapes. Given that the aim of this thesis project is to further reduce the base drag contribution of a HDV with a tail, it is argued that it is not necessary to model the front part in too much detail and the GETS model is selected. An additional reason for selecting this model is that the wind tunnel campaign is performed in conjunction with a master thesis research on a platoon of HDV's which used the GETS model. A schematic drawing of the GETS model with a tail and its main dimensions can be found in figure 2.4, the dimensions for the full-scale and 1/8-scale model are given in table 2.1. Also the axis convention and origin that are used throughout this thesis are included in figure 2.4. When the numerical results are presented in chapter 3, the drag of the model is often split up into several contributions by each zone. Fig. 2.5 shows how the front, centre and base of the GETS model are defined.

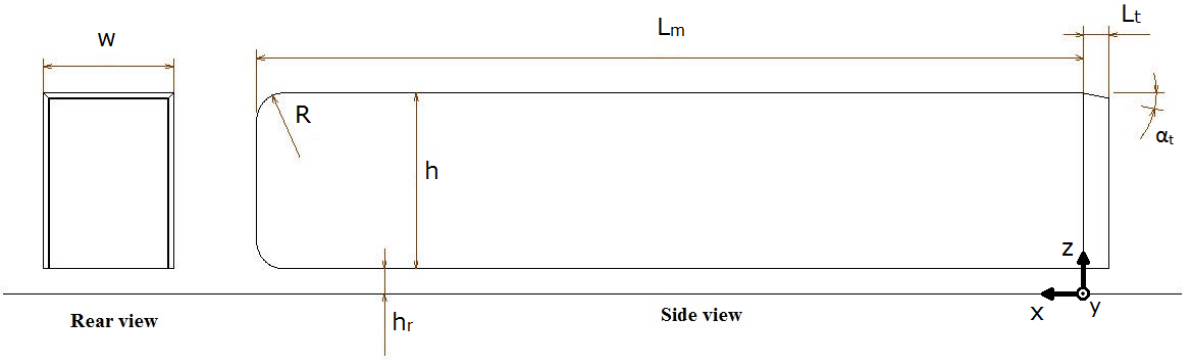

Figure 2.4: **Schematic of the GETS model with tail**

During this research various types of guide vanes are placed on the trailing edge of the tail in order to reduce the base drag. This leads to a number of design parameters that are varied to understand the working of such a vane and find the most effective design. The parameters that are varied during this study are the airfoil profile, the incidence angle, the chord length and the gap height. Fig. 2.6 shows how these parameters are defined. Note that the incidence angle of the guide vane is defined relative to the negative x-axis. The guide vane is placed at the trailing edge of the tail, which has a slant angle

of $12°$. So a guide vane with an incidence angle of $\alpha = 12°$ has its chord line oriented parallel to the tail.

Table 2.1: **Dimensions of full-scale GETS model**

Dimension	Symbol	Full-scale	1/8-scale
Length [m]	L_m	16.5	2.063
Width [m]	w	2.6	0.325
Height [m]	h	3.5	0.438
Frontal area [m^2]	S	9.1	0.142
Ride height [m]	h_r	0.5	0.063
Front radius [m]	R	0.54	0.068
Tail length [m]	L_t	0.5	0.063
Tail angle [°]	α_t	12	12

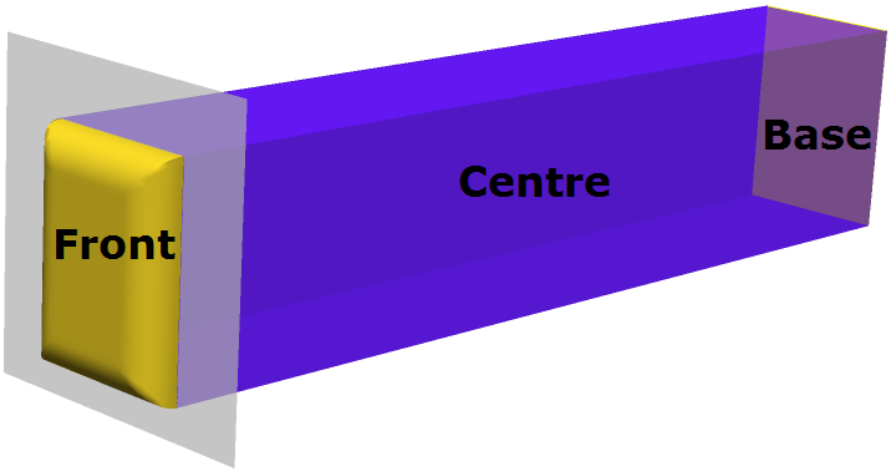

Figure 2.5: **GETS model split up into various zones for drag decomposition**

2.2.2. Computational domain

The computational domain is created by subtracting the surface model from an enclosing volume of air. On all faces of this domain the right boundary conditions need to be applied. These boundary conditions also impose requirements on the size of the enclosing volume. For instance there should be enough vehicle lengths in front and behind the vehicle for the boundary condition of uniform in- and outflow to be valid. It is recommended that the computational domain should extend at least three vehicle lengths in front and five lengths behind the vehicle. Furthermore SAE J2966 guidelines [53] prescribe that the minimum cross section of the domain is 10w by 6h. Whereas Lanfrit [35] recommends that the projected vehicle area should not be more than 1-1.5% of the total cross-sectional area, which results in a very similar requirement. The computational domain around the GETS model and its dimensions is shown in figure 2.7.

Boundary conditions

All faces of the computational domain that are related to the vehicle model (GETS model, tail, guide-vane, etc) are modelled as no-slip walls. A symmetry boundary condition is applied to the top of the domain in all simulations. For symmetric (zero yaw) conditions the sides of the domain are also modelled with a symmetry boundary condition. Whereas for the simulations of a crosswind angle these sides are assigned an inlet and outlet boundary condition respectively. The symmetric case is also

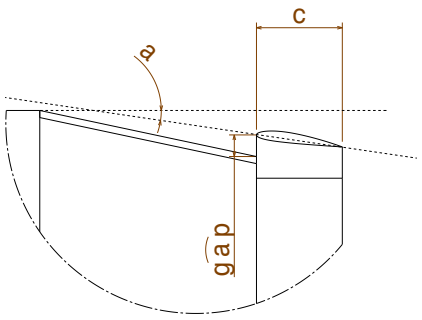

Figure 2.6: **Definition of the design parameters of a guide vane on a tail**

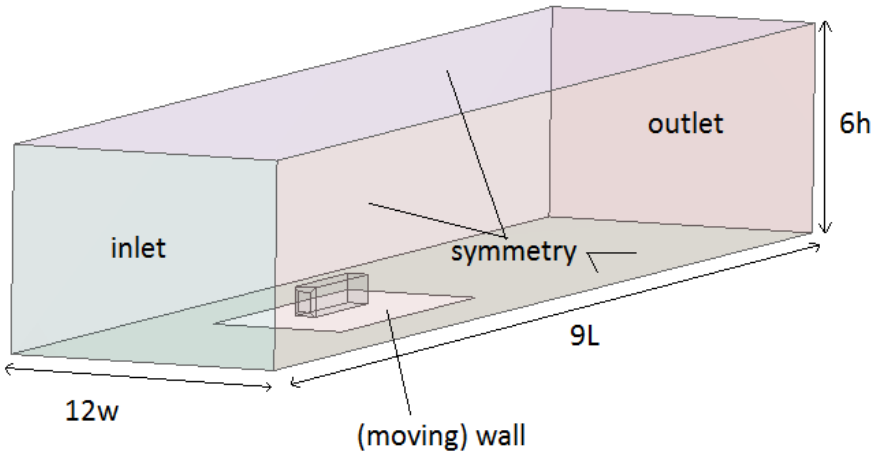

Figure 2.7: **Computational domain around the GETS model including boundary conditions in a $0°$ yaw case**

simulated using a full model, as this allows for the same mesh to be applied for the crosswind simulations, using different boundary conditions. This was considered to be more efficient than having to build a new mesh when simulating crosswind conditions, as the generation of a mesh and uploading it to the HPC cluster is a time-consuming process.

The front face of the domain is defined as a velocity-inlet, whereas the rear face is modelled as a zero gradient pressure outlet. Fluent requires the velocity magnitude, direction vector, turbulence intensity and turbulent length scale to be prescribed for these faces. The initial set of simulations were performed at a velocity of $25m/s$ while the validation runs matched the wind tunnel speed of $15m/s$. In the validation runs the turbulence intensity was set to 0.3% to match the value of the OJF measured by Barlas et al. [6] The turbulent length scale is set to half the vehicle width, as this is the expected size of the largest eddies in the wake containing the most energy. In the initial simulations the turbulence intensity is set to 1% at the inlet and 5% at the outlet. This range of turbulence intensities was measured on the road by Watkins [70] and it was argued that the turbulence is higher downstream of the vehicle. The turbulent viscosity ratio is kept at the default value of 10 as was recommended by Fluent for external aerodynamics. The floor can be modelled as a stationary or a moving wall. During the mesh sensitivity study, which is described in section 2.3 both options were simulated and it was found that the influence on C_T was small. For the full-scale simulations a moving wall boundary condition was used to better represent road conditions. During the validation runs the floor was modelled as a stationary wall with

the same dimensions as the ground board used in the wind tunnel, while the rest of the bottom plane was assigned a symmetry boundary condition. A schematic of the boundary conditions on the faces of the domain around the model for a symmetric (0° yaw) case are given in figure 2.7.

2.2.3. Meshing strategy

The generation of the mesh is performed using ANSYS Meshing to ensure a smooth work flow in conjunction with Fluent. This software creates an unstructured grid of tetrahedral elements in the computational domain. The size of the tetrahedral elements is reduced in the area around the vehicle to accurately model the flow phenomena of interest. To achieve this, two refinement boxes are created around the vehicle model. The wake-box fits closely around the model, but extends further back to also enclose the wake and has the largest grid density. The second box ensures that the cell size in a larger area around the model is sufficiently small, such that the cell size far away from the model can be kept relatively large to reduce the total number of elements. The dimensions of the refinement boxes as well as the computational domain relative to the origin are given in table 2.2. Note that as defined in figure 2.4 the origin is located at the base of the GETS model at the intersection of the road and the symmetry domain. During the mesh sensitivity study, the appropriate element sizes were determined for these refinement boxes. During the simulations of the guide vanes the cell size on the curved faces of the vane was further refined to accurately describe the airfoil shape. An example of the mesh around the model as seen from the symmetry plane is given in figure 2.8. Here the unstructured grid around the model, inner refinement box and inflation layers are clearly visible.

Table 2.2: **Dimensions of computational domain and refinement boxes**

Box	x_{start}	x_{end}	y_{start}	y_{end}	z_{start}	z_{end}
Domain	4L	-5L	6w	-6w	0	6h
Outer refinement	1.5L	-L	3.2w	-3.2w	0	2.4h
Inner refinement	1.1L	-0.5L	0.65w	-0.65w	0	1.3h

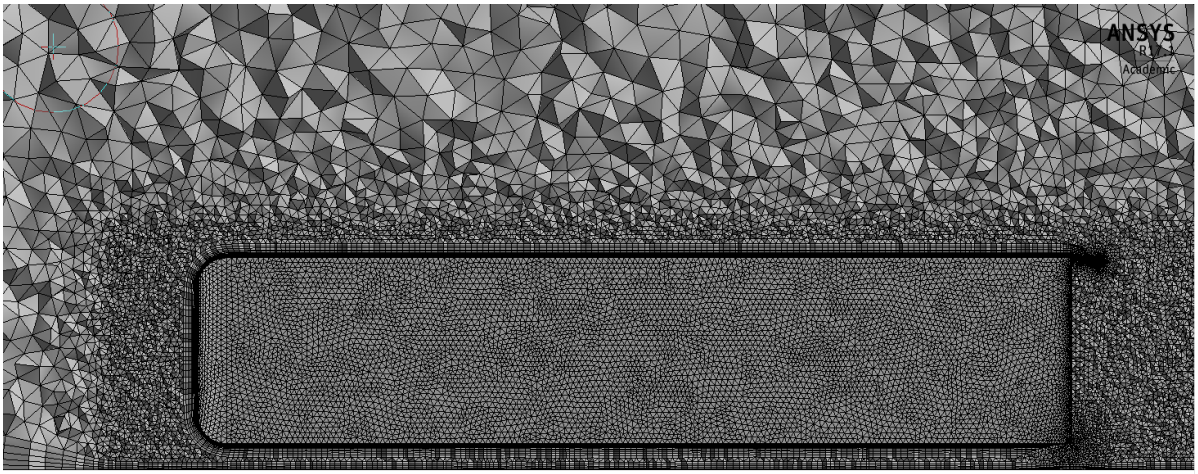

Figure 2.8: **Mesh around the GETS model with tail and guide vane in the symmetry plane**

Inflation layer

To accurately describe the boundary layer around the vehicle, an inflation layer is placed on the model. This layer is generated by the mesher by first creating a surface mesh and extruding this outwards to form layers of prism elements. All wall surfaces except for the GETS base and the inside of the tail get an inflation layer as these faces lie in the vehicle wake and generally do not have attached flow.

Important to consider is the thickness of the first layer (and the corresponding y^+ value), the growth rate and the number of inflation layers. As was described in subsection 2.1.3 the enhanced wall treatment option automatically switches between near wall modelling and wall functions depending on the value of y^+. However, the intention is to use wall functions to avoid the need for an excessively fine mesh, which requires y^+ to be between 30 and 300. A y^+ value of 100 was selected for the road, the front and centre of the GETS model, the outside of the tail panels and the guide vane. The height of the first cell is determined by re-writing the y^+ expression and taking the cell half-height as a reference:

$$y_{1/2} = \frac{y^+ \mu}{\sqrt{\tau \rho}} \tag{2.7}$$

Where the wall shear stress τ is estimated by taking the skin friction coefficient C_f of a turbulent flat plate boundary layer of the same reference length as the GETS model: [72]

$$C_f = \frac{0.027}{Re_x^{1/7}} = \frac{\tau}{1/2 \rho V^2} \tag{2.8}$$

The number of prism layers is determined by selecting a growth rate and estimating the total thickness of the boundary layer by again assuming a turbulent flat plate boundary layer, which is given in equation (2.9) [72]. The growth rate should not be larger than 1.2 according to Lanfrit [35], so a value of 1.1 was selected for the 1/8-scale simulations and 1.15 for the full-scale simulations.

$$\frac{\delta}{x} = \frac{0.16}{Re_x^{1/7}} \tag{2.9}$$

As the inflation layers are extruded out of the surface mesh before the rest of the domain is filled with tetrahedral elements, conflicts can occur when surfaces are in close proximity. The meshing algorithm tries to avoid this by either compressing the layers to a lower thickness or by locally reducing the number of layers in a ‘stairstep’ approach. Stairstepping uses pyramid elements to transition from prism to tetrahedral elements and is also required if a face with an inflation layer is adjacent to a face without one. It can be seen in figure 2.9 that over the largest part of the model the intended value of $y^+ = 100$ is achieved. As the flow accelerates over the rounded front end, the value of τ and consequently y^+ increases, but stays well within the range where wall functions are valid. The highest y^+ value on the model is 194, while the wall functions are valid for $30 < y^+ < 300$. On the stagnation surface y^+ is below this range, but in that case the SST $\kappa - \omega$ model switches to near wall modelling, as was explained in subsection 2.1.3.

Mesh quality

The quality of the mesh was checked every time before proceeding with the simulation. This is important because a low quality mesh can negatively influence the accuracy of the solution or the convergence of the solution. A visual inspection of the mesh is performed to see if the guide vane is described with enough elements to ensure a smooth contour. Additionally, a number of mesh metrics are monitored to find problem areas and give an indication of the mesh quality. The main mesh metric that was considered is the skewness, which is the difference between the ideal and actual cell size, as depicted in figure 2.10. Even though the Green-Gauss node-based gradient approach is used interpolation errors or convergence problems can occur if the average and maximum skewness of the mesh is too high. Another mesh metric to consider is the aspect ratio, which is the ratio of the longest to the shortest side of a cell. When applying an inflation layer to the floor cells in the full-scale simulations, it was found that giving the entire bottom face of the domain an inflation layer resulted in unacceptable aspect ratios. This was caused by the combination of a low first cell thickness for the intended y^+ value and coarse mesh far away from the model. Therefore only the region of the bottom face overlapping with the outer refinement box was given a moving wall boundary condition and an inflation layer, while the rest of the bottom face was assigned a symmetry boundary condition and tetrahedral elements.

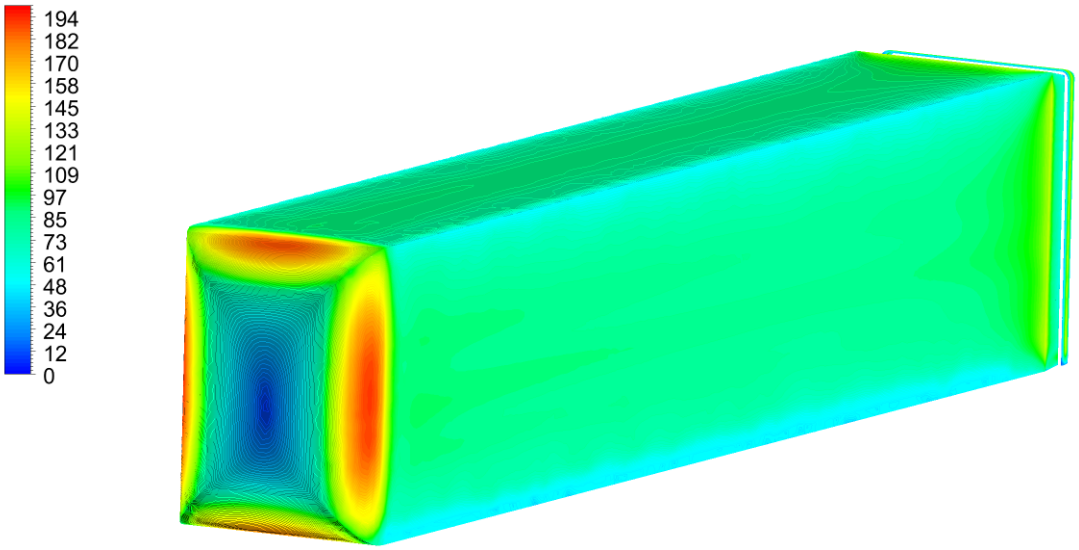

Figure 2.9: **Contours of y^+ on the full-scale GETS model with tail and guide vane**

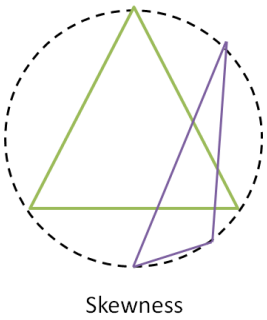

Figure 2.10: **Skewness compared to an equilateral triangle**

2.3. Mesh sensitivity study

A mesh sensitivity study was performed by increasing the number of cells in the mesh while observing the drag of the GETS model with a tail. This is important because the mesh should be fine enough to accurately predict the dominant flow phenomena and consequently the drag coefficient. However, if the mesh is made overly refined this increases the computational requirements. Therefore it is important to know the convergence behaviour of the drag coefficient with respect to the number of cells. This way a refinement can be chosen that is suitable for the application and in accordance with the available computational resources. The goal is to have a solution that is independent of the resolution of the mesh, to a certain degree.

2.3.1. Mesh refinement

The mesh sensitivity study is performed by stepwise reducing the element size in the two refinement boxes. A 1/15-scale GETS model with a tail is used in the mesh sensitivity study. The tail that was used in the mesh sensitivity study is different than the tail design that became the 'baseline configuration' in this thesis. The tail in the mesh sensitivity study also has a slant angle of $12°$, but features plates on all four edges of the base and has a length of $L_t = 0.091L_m$, or 0.1m in 1/15-scale. Because only $0°$ yaw angle flow is considered, a half model is used to save computational resources. The cell count in

table 2.3 and figure 2.11 should therefore be doubled when comparing to a full model. The mesh size in the outer domain was kept constant at a maximum of 150mm.

Table 2.3: **Overview of meshes used in grid refinement study, 1/15-scale**

Mesh	Outer box cell size [mm]	Wake box cell size [mm]	Cell count 10^6	C_T [-]
1	30	15	0.67	0.2082
2	20	10	1.11	0.2002
3	16	8	1.69	0.1943
4	14	7	2.25	0.1907
5	12	6	3.25	0.1872
6	12	5	4.51	0.1843
7	12	4	7.19	0.1826
8	10	4	7.96	0.1824

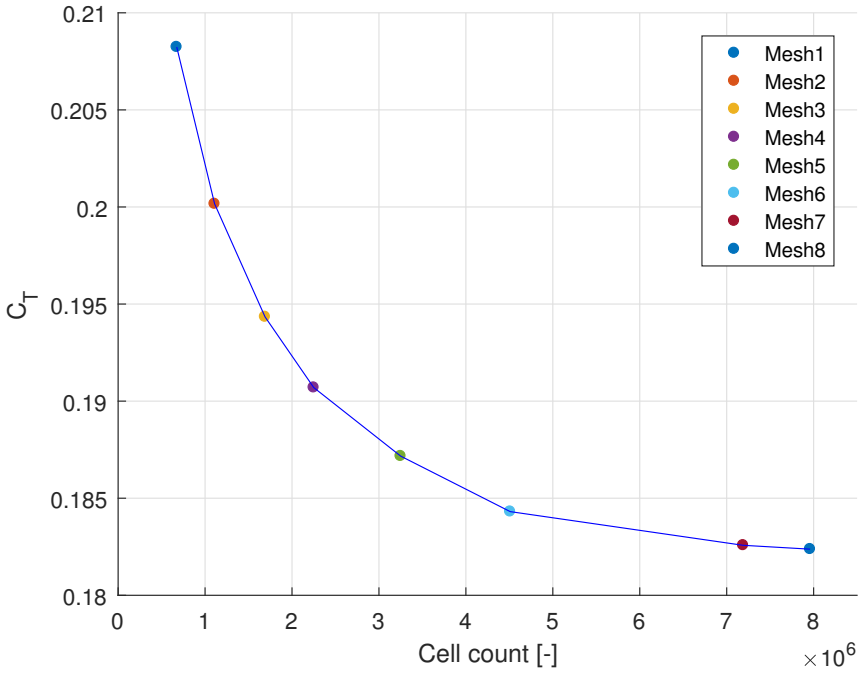

Figure 2.11: **Drag coefficient convergence versus the cell count of the various half-model meshes used in the mesh sensitivity study**

It can be seen in figure 2.11 that over the first 4 meshes where the cells in both the inner and outer boxes are refined the drag coefficient sharply drops with respect to the cell count. For meshes 5, 6 and 7 only the inner box is refined, which causes C_T to reduce further. In the case of mesh 7, the C_T value reduces with approximately 1%, but at the cost of more than 2.5 million additional cells. Between the last two meshes only the outer box is refined once more, but it can be seen that this has no significant effect. The numerical analysis in this thesis project aims to test many different drag reduction solutions and indicate trends rather than establish exact drag values. Therefore it is not feasible to use the most refined mesh, as this would lead to more than 15 millions cells on a full model that does not even include the drag reduction device yet. Therefore the refinement of mesh 4 is deemed acceptable, with an error of less than 5% with respect to the drag coefficient of the finest mesh. For the simulations that are performed on a model of a different scale, the cell size is scaled accordingly to yield roughly the same number of cells. Note that the size of the cells in the inflation layer does not scale accordingly as this is determined by the y^+ value, as was described in subsection 2.2.3. Moreover,

a refinement is applied to the curved faces of the guide vane to accurately describe the airfoil curvature.

Next to performing the sensitivity study of the C_T with respect to the cell count, some other parameters were varied to check the impact on the drag coefficient. For instance a simulation was performed on a full model with the same cell size as mesh 6, but this leads to a difference of around 1%, while using twice as many cells. This supports the decision to perform the mesh sensitivity study with only a half model. However, as was explained in subsection 2.2.2, the other symmetric simulations in this research are performed on a full model, because this allows the same mesh to be used for the crosswind simulations. The 'double precision' option in fluent was applied, but this leads to a difference of less than a drag count with respect to the 'single precision' while taking longer to converge. Also the difference between a moving and stationary wall boundary condition for the floor was investigated, but this yielded a difference of 2 drag counts, which is in line with what was found by Kruijssen. [34]

2.3.2. Uncertainty

Obviously choosing a lower mesh refinement for the simulations in this research than the finest mesh in table 2.3 introduces an error to the numerical results. To some extent this error is inevitable as the limited computational resources do not allow for all the configurations under consideration to be simulated with such a degree of refinement. It would have been possible to perform each simulation with higher accuracy, but this would have limited the number of parameters that could be investigated. So ultimately it is also a choice of accuracy versus design flexibility. Moreover, by choosing a highly simplified vehicle model (GETS) it has already been ruled out that the predicted C_T value will be close to that of an actual truck driving on the road. Therefore the focus in this study lies on discovering trends and understanding the working principle of a guide vane in combination with a tail, rather than predicting the C_T value to a high degree of accuracy. Yet it is still useful to estimate the magnitude of the discretisation error that is introduced by selecting this particular mesh refinement.

A procedure for estimation and reporting of uncertainty due to discretisation in CFD applications is described by Celik. [11] This work is also the recommended practise according to SAE J2966. [53] Here it is suggested that the uncertainty of CFD simulations is presented by means of the Grid Convergence Index (GCI). This requires a 'course', a 'fine' and a 'finer' grid to be defined, where the GCI of the fine grid is defined as:

$$GCI_{fine}^{ij} = \frac{1.25 e_a^{ij}}{r_{ij}^p - 1} \tag{2.10}$$

In this equation the GCI between the i^{th} and j^{th} grid is determined in terms of their respective approximate relative error e_a^{ij} and grid refinement factor r_{ij}. This is solved in an iterative process after assuming an apparent order of the grid convergence. In the mesh sensitivity study 8 different meshes have been used, whereas this method requires three meshes. This was handled by selecting meshes with numbers 1, 4 and 8 as the 'course', 'fine' and 'finer' meshes respectively to calculate the GCI. While determining the GCI it was observed that the extrapolated C_T value as predicted by Celik's method using three data points was not very accurate compared to the behaviour visible in figure 2.11. Therefore an extrapolated value of $C_{T,e} = 0.180$ based on all 8 meshes was used. Ultimately the GCI was determined, which estimates an uncertainty due to discretisation of 4.3%. A review of reported GCI values in literature revealed that these generally lie between 1 and 5%. That implies that the accuracy of the numerical simulations in the present study is on the low side of the acceptable range. It is argued that this is acceptable given the design context in which the simulations are used.

Strictly following the recommended practise in SAE J2966 would require error bars of this magnitude to be included in all numerical results. However, the author believes that this would not be beneficial for the readability of the figures in this thesis. Therefore error bars indicating the uncertainty due to

discretisation error are presented once in figure 2.12. Here the drag contributions of the GETS model fitted with a tail are shown, with error bars of 4.3% above and below each of the contributions and the total drag coefficient. It can be seen that the numerical uncertainty represents a significant portion of the drag coefficient, especially given the small delta's that make the difference in vehicle drag reduction. However, it is believed that despite this uncertainty, the numerical simulations are still able to indicate trends in the results. Oberkampf [46] argues that convergence of numerical error is more closely analogous to bias errors in experimental measurements rather than statistical uncertainty. The monotonic convergence of the drag coefficient presented in figure 2.11 provides confidence to regard it as such. If the error due to grid convergence is the same for configurations simulated in this research, the relative drag reductions should still provide grounds to draw conclusions. The observed behaviour of the results presented later in this report, like the trend lines and curves in figures 6.14, 6.14 and 6.16, do not indicate the presence of random fluctuations. However, it should be noted that Oberkampf's view of discretisation uncertainty is not shared by everyone. For example, Roache [52] does argue for the error due to grid convergence to be reported as a probability.

According to Celik [11] the iteration uncertainty induced by stopping the simulation after a number of iterations should at least be an order of magnitude smaller than the discretisation uncertainty. As was shown in figure 2.3 the drag coefficient converges to a steady value and shows no oscillatory behaviour. The iteration uncertainty was found to be less than 0.1% of the final C_T value. Ultimately the best way to address the problem of numerical uncertainty is to perform verification and validation procedures by comparing the results to previous work and the experimental data.

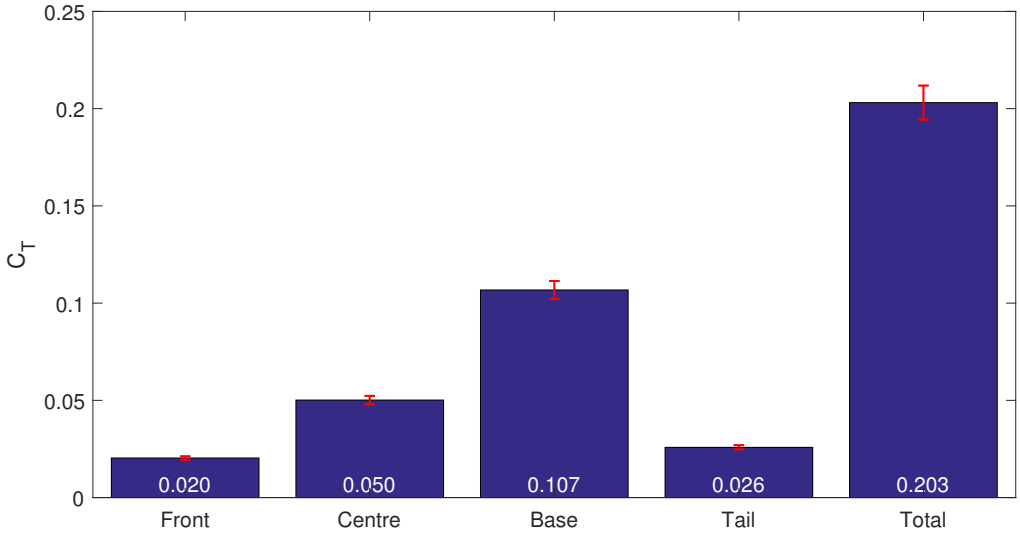

Figure 2.12: **Drag contributions of the GETS model with tail, with error bars representing GCI. Full-scale,** $V = 25m/s$, $(Re = 5.1 \cdot 10^6)$

3

Numerical results

In this chapter the results from the numerical analysis will be presented. First the GETS model without any drag reduction devices will be analysed in section 3.1. The baseline configuration against which the drag reduction devices designed in this study will be compared in the GETS model fitted with a tail with a full-scale length of 500mm. The drag and the flow field around this baseline model will be presented in section 3.2. The goal of this research is to improve the drag reduction that is achieved by a tail behind an HDV. In section 3.3 the results of placing a guide vane to the trailing edge of the tail are given. Finally it was investigated whether the performance of the tail could be improved by incorporating a slot in the design of the panels, which is presented in section 3.4. All force and moment coefficients presented in this report are normalised with respect to the free-stream dynamic pressure and the frontal surface area of the GETS model. Drag reductions are presented in drag counts, taking notice that in the automotive industry a drag count is defined as one thousandth of a drag coefficient or C_T = 0.001 = 1 drag count.

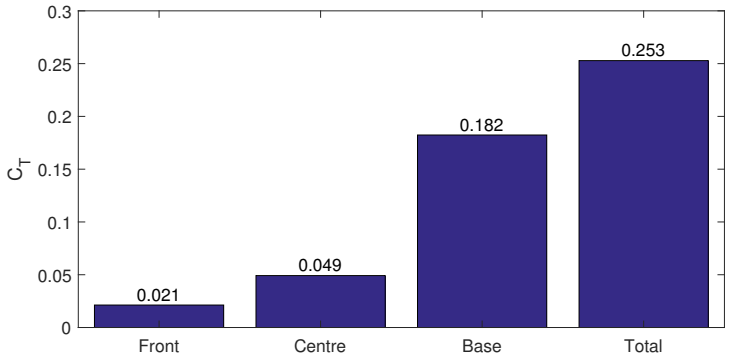

Figure 3.1: **Drag contributions of the GETS model without drag reduction devices. Full-scale,** $V = 25m/s$**,** $Re = 5.1 \cdot 10^6$

3.1. GETS model

The goal of this study is to improve the drag reduction of a tail behind the GETS model by combining it with a guide vane. Therefore the GETS model with a tail will serve as the baseline configuration. However, first the GETS model without any drag reduction devices is simulated. When the drag coefficient and flow field around the basic GETS model is known, this will put any drag reductions that are found on the baseline configuration into perspective. The simulations are performed using a full-scale model and a flow velocity of $25m/s$, resulting in a Reynolds number of 5.1 million based on

the square root of the frontal area. The drag coefficient of the full-scale GETS model at yaw angle $\Psi = 0°$ was found to be $C_T = 0.253$.

The drag contributions of the various parts of the model are given in figure 3.1, where it can be seen that the base is the main source of drag. It might seem counter-intuitive that the contribution of the front of the vehicle is so small, despite the large stagnation surface. This is because the rounded front edges with radius $R = 0.54m$ are also included in the front surfaces. When looking at figure 3.2 it can be seen that there is indeed a large high pressure zone in front of the vehicle due to the stagnation surface. But the flow then accelerates over the rounded front edges. This causes a low pressure and because these surfaces face forwards, results in a thrust force, which explains the small drag contribution for the front part as a whole. The contribution of the centre of the GETS model includes the top, bottom, left and right sides of the model starting directly after the curved front edge, as was defined in subsection 2.2.1.

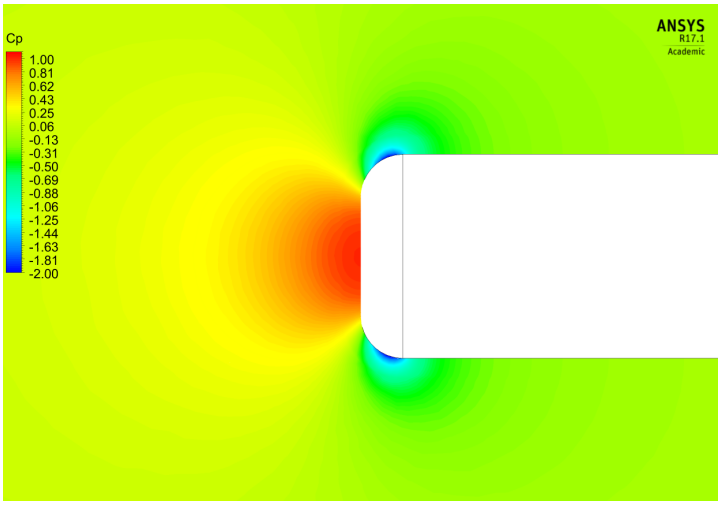

Figure 3.2: **Contour of Pressure coefficient over front part of GETS model in horizontal plane, z = 2.0 m. Full-scale,** $V = 25m/s$, $Re = 5.1 \cdot 10^6$

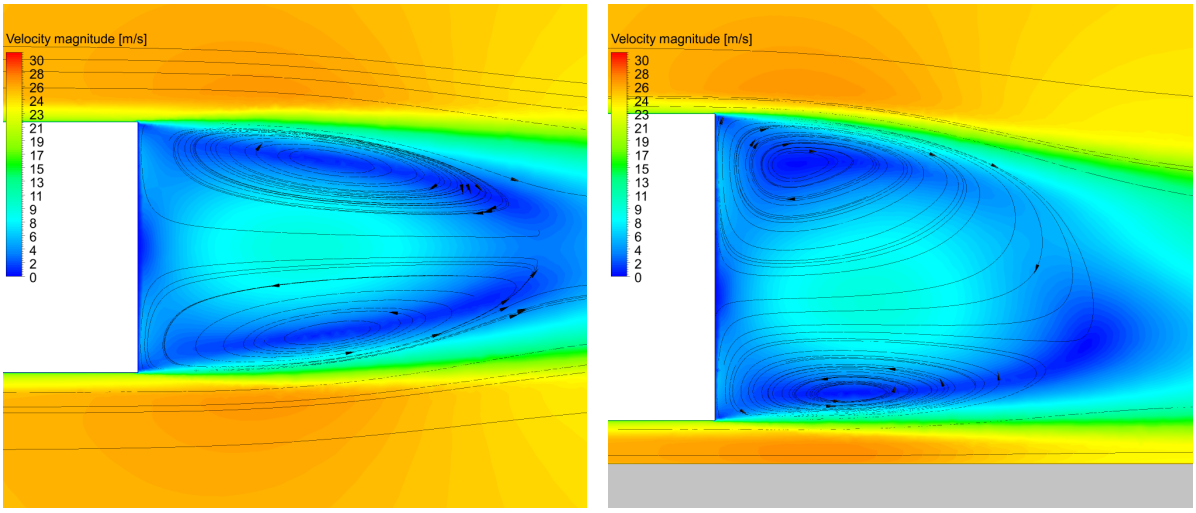

(a) Top view, z = 2m

(b) Side view, symmetry plane

Figure 3.3: **Velocity magnitude and streamlines in the wake of the GETS model. Full-scale,** $Re = 5.1 \cdot 10^6$

Fig. 3.3 shows the wake behind the GETS model that is the main source of drag. The streamlines in

both the top and side view show counter rotating vortices, that together form a vortex ring in the wake. The drag reduction devices that are investigated in this research rely on reducing the strength of this vortex ring to reduce the base pressure. This vortex ring can be visualised by plotting an iso-surface of constant C_p in the wake area. It can be seen in figure 3.4 that in the center of the ring vortex there is a backflow region. This causes the base pressure in this region to locally be higher than the surrounding area, as can be seen in figure 3.8. The lowest pressure on the base is found on the top half, which is closest to the large vortex that is shed from the top edge of the model.

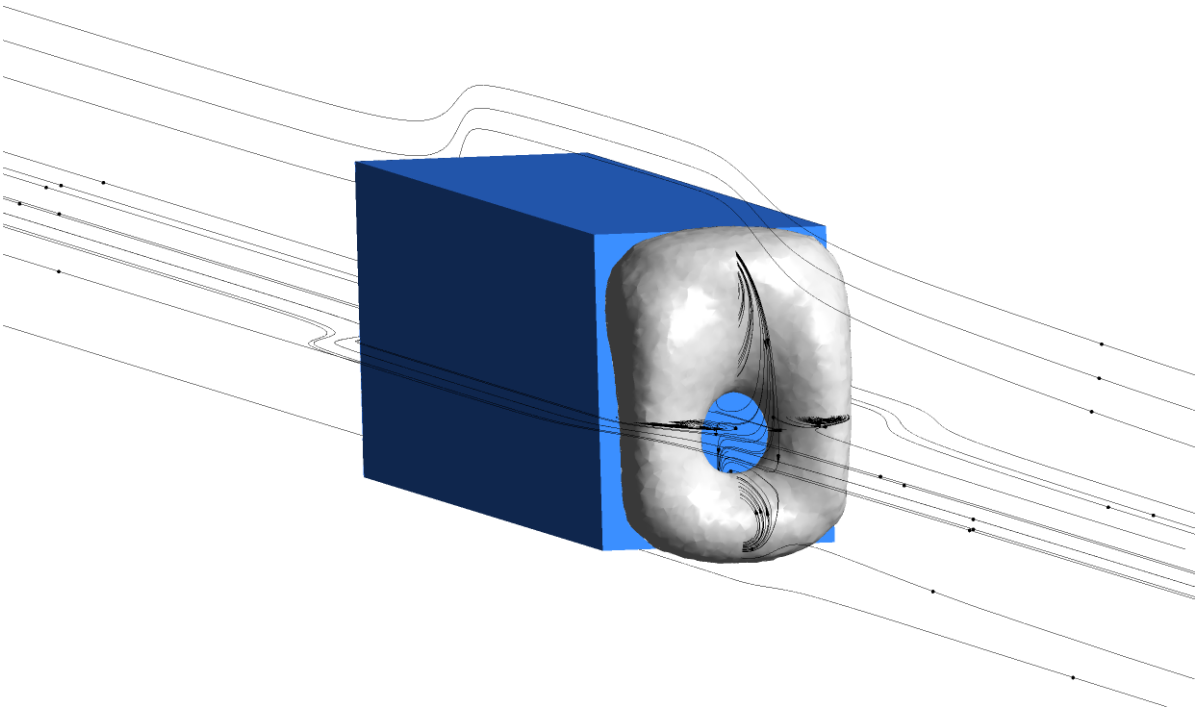

Figure 3.4: **Iso-surface of $C_p = -0.22$ behind GETS model with streamlines. Full-scale, $V = 25m/s$, $Re = 5.1 \cdot 10^6$**

3.1.1. Validation of GETS simulations

The benefit of using an existing generic vehicle model is that many previous studies have analysed it and therefore the results can be compared. The single GETS model has been analysed by two master thesis researches at the TU Delft by van Leeuwen [64] and Gheyssens [24] respectively. Gheyssens found the drag coefficient of the full-scale GETS model at $0°$ yaw angle to be 0.288, which is significantly higher than what was found in this study. Van Leeuwen found an even higher value of $C_T = 0.318$ for the full-scale GETS model. The largest difference between the simulations performed by van Leeuwen and this study is that he used the realisable $\kappa - \varepsilon$ turbulence model and SIMPLEC pressure velocity coupling. Comparing the drag contributions in table 3.1 it can be seen that van Leeuwen predicts a much higher front drag contribution than the other two studies. He notes that the stagnation pressure on the front surface $C_p = 1.02$ is higher than physically possible, which he attributes to a known error of the $\kappa - \varepsilon$ model according to Perzon et al. [48] Interestingly the side drag contributions of all three works are very close and consequently the viscous drag components show good agreement. Also the corrected C_T of the 1/15-scale GETS model as measured by van Raemdonck [65] in the wind tunnel is included in table 3.1. In terms of drag contributions only the pressure term of the base pressure is known, which is relatively close to the simulated value from the present study. Important to note is that the simulation models do not feature support legs, which the wind tunnel model does. These legs increase the C_T of the wind tunnel model, which partly explains the difference between the experimental C_T value and the one found in the present study.

Table 3.1: **Comparison of simulated C_T contributions of the GETS model compared to previous studies. Full-scale simulations, $V = 25m/s$, $Re = 5.1 \cdot 10^6$. Corrected 1/15-scale wind tunnel results, $V = 60m/s$, $Re = 0.83 \cdot 10^6$**

	Front	Centre	Base	C_T	Pressure	Viscous
Present study	0.021	0.049	0.182	0.253	0.198	0.055
Gheyssens	0.026	0.055	0.207	0.288	0.228	0.060
van Leeuwen	0.130	0.054	0.134	0.318	0.261	0.057
Wind tunnel	-	-	0.163	0.297	-	-

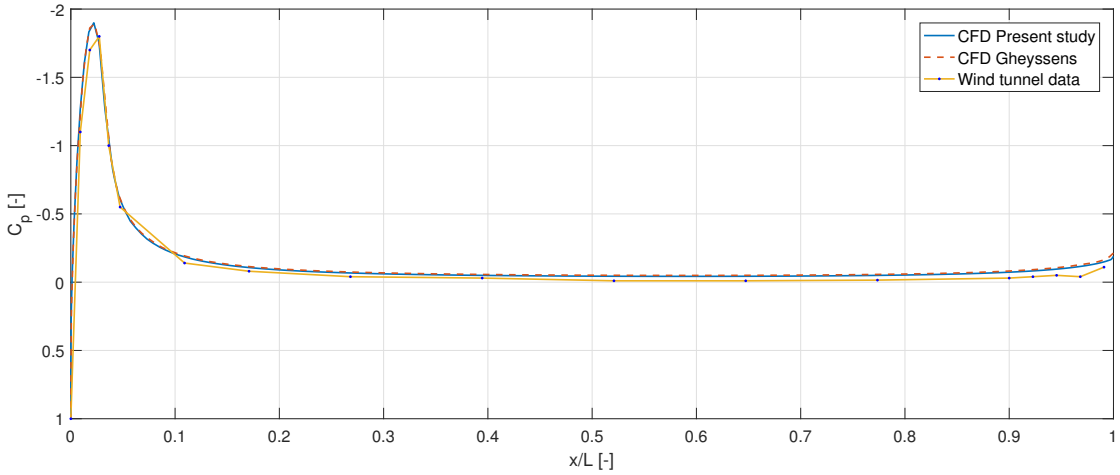

Figure 3.5: **C_p distribution over the top of the GETS model compared to CFD results of Gheyssens [24] and wind tunnel data of van Raemdonck and van Tooren [66]. Full-scale simulations, $V = 25m/s$, $Re = 5.1 \cdot 10^6$. Corrected 1/15-scale wind tunnel results, $V = 60m/s$, $Re = 0.83 \cdot 10^6$**

Comparing the drag contributions of this study to the work of Gheyssens reveals that the drag contributions of the front and side surfaces show good agreement. This is backed up by the C_p distribution over the top half of the GETS model presented in figure 3.5. Here it can also be seen that the C_p distribution agrees relatively well with the wind tunnel measurements by van Raemdonck. [65] The difference between the drag values is caused by the base drag contribution. Comparing the rear pressure distributions revealed that the difference could partly be traced back to a number of erroneous low pressure 'spots' on the base surface of Gheyssens. In figure 3.6 the base pressure coefficient is plotted against height, where the C_p values are averaged horizontally over all locations with the same z-coordinate. Here it can be seen that both simulated pressure distributions show the same S-shaped behaviour. The region of local higher pressure pressure due to backflow in the ring vortex is at the same location, but causes a larger peak in Gheyssens's simulations. The same is true for the regions of lower C_p near the top and bottom. Near the bottom the C_p distribution of Gheyssens shows some irregular behaviour, which is caused by one of the low pressure 'spots' mentioned earlier. When comparing the simulated to the experimental pressure distributions it can be seen that the wind tunnel model does not have an S-shaped profile. Also when looking at the C_p distribution over the whole base surface as shown in figure 3.8, this is not representative of the actual situation in the wind tunnel. This is due to the inaccuracy of the mean flow solution of the RANS simulations, as was indicated by, among others, van Raemdonck [65], Pointer [50] and Storms [57]. A better representation of the actual base pressure distribution can be achieved by performing LES, as was shown by Krajnovic [33]. What can be deducted from figure 3.6, however, is that over the top half of the base, the simulated C_p distribution of the present study is closer to the wind tunnel data than that of Gheyssens. Looking at the flow structure behind the wind tunnel model in figure 3.7 it can be seen that the size and shape of the top vortex is different than predicted by the simulation in figure 3.3b. This inability to accurately

simulate the flow structure in the wake and the different floor boundary condition are the cause of the discrepancy between the numerical and experimental C_p distribution over the lower half of the GETS model.

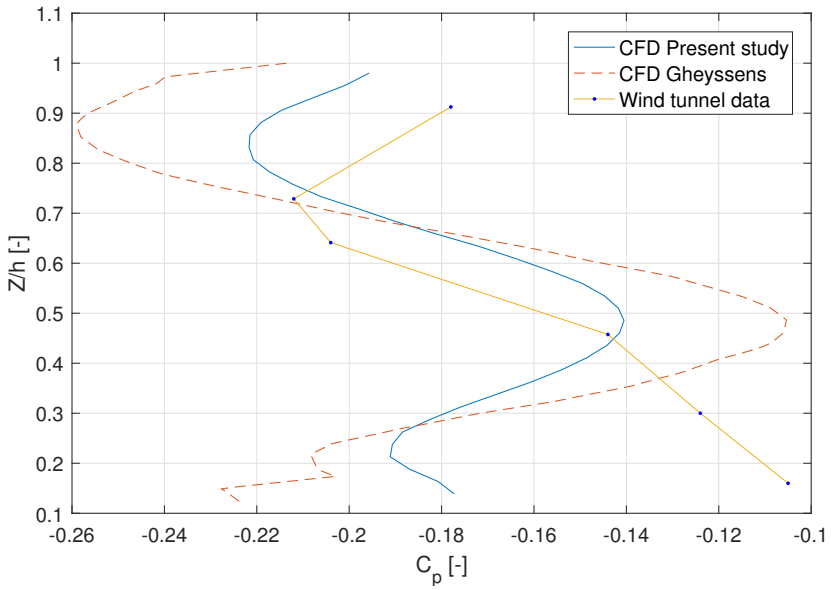

Figure 3.6: **Averaged horizontal C_p versus height on the base of the GETS model compared to CFD results of Gheyssens [24] and wind tunnel data of van Raemdonck [65]. Full-scale simulations, $V = 25m/s$, $Re = 5.1 \cdot 10^6$. Corrected 1/15-scale wind tunnel results, $V = 60m/s$, $Re = 0.83 \cdot 10^6$**

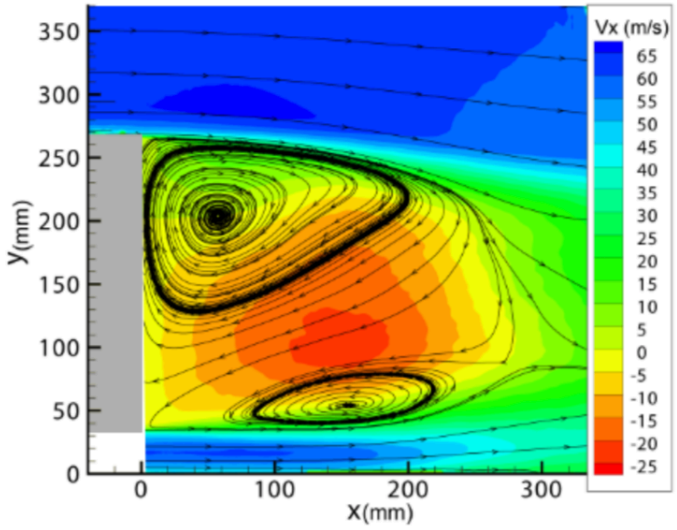

Figure 3.7: **Wake structure behind the 1/15-scale GETS model obtained by PIV measurements by van Raemdonck [65],** $V = 60m/s, Re = 0.83 \cdot 10^6$

3.2. Baseline configuration

The baseline configuration in this study is the GETS model fitted with a tail of length $L_t = 0.03L_m$ with a slant angle of $12°$ on the top and side edges of the base. This is representative of a commercially available tail [69] with a full-scale length of 0.5m behind the trailer as allowed in the European union since 2015. [18] The effect of the tail is that the drag contribution of the base is reduced. The tail itself produces a small amount of drag because of the low pressure acting on the outside of the panels, which face rearwards. The tail reduces the drag coefficient of the GETS model with 50 drag counts to $C_T = 0.203$, which is a 19.7% reduction. It can be seen in figure 3.9 that the contributions of the front and centre remains practically unchanged, while the base drag reduces with 76 drag counts and the tail panels add some drag. The simulated drag reduction of the tail is in accordance with other research. A tail with the same length and slant angle was analysed by Kruijssen [34] on a different vehicle model, where a drag reduction of approximately 60 drag counts was found. A commercially available tail of these specifications was tested in the wind tunnel at full scale on an actual semi-truck by Leuschen and Cooper [36]. They found a 51 drag count reduction using a similar tail and a reduction of 44 drag counts using an inflatable tail prototype. Fig. 3.8 shows the distribution of the pressure on the base of the GETS and baseline model plotted to the same scale. Here it is clearly visible that the tail causes an increase in base pressure, which leads to the lower drag coefficient.

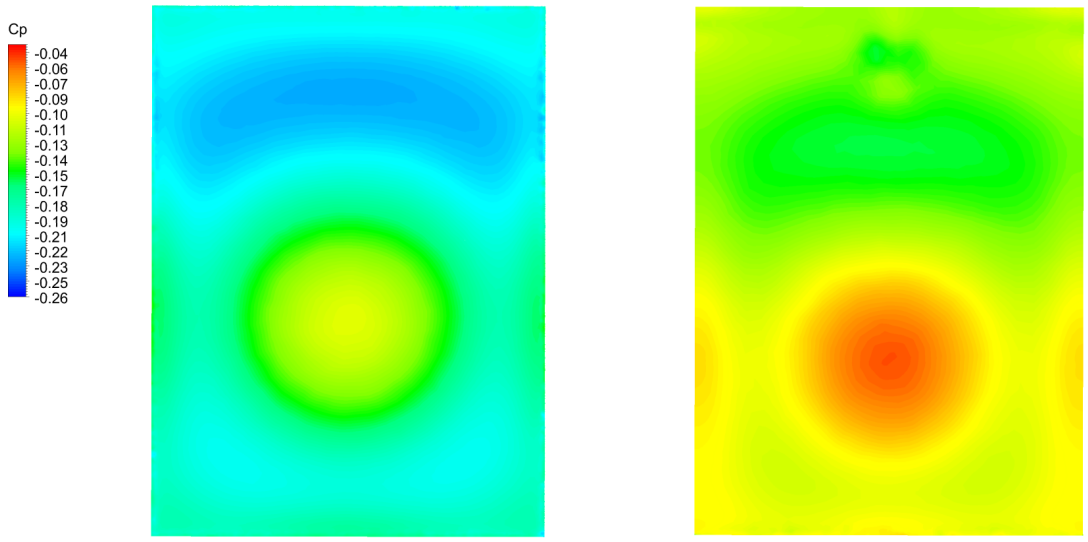

Figure 3.8: **Base pressure coefficient distribution on the GETS model without a tail (left) and with the baseline tail (right). Full-scale,** $V = 25m/s$**,** $Re = 5.1 \cdot 10^6$

The tail panels guide the flow behind the model inwards, which causes the wake to become smaller. When comparing figure 3.10 to figure 3.3 it can be seen that the wake behind the baseline model is narrower and shorter than behind the GETS model without tail. In the top view it is clearly visible that the reattachment point of the shear layers originating from the sides lies closer for the baseline model. Because the tail has no bottom plate, the bottom vortex stays approximately in the same place as for the GETS model, while the top vortex is shifted downwards by the top plate, which causes the reattachment point to be shifted downwards as well. This can also be seen in figure 3.8 where the centre of the high pressure region caused by the back-flow in the ring vortex is located lower for the baseline model.

3.2.1. Scaled simulations

At the start of the research simulations were performed on a 1/8-scale GETS model fitted with a tail and various guide vane and slot configurations. Evidently, the results of these simulations should be compared to the GETS and baseline model at the same scale for the comparison to be fair. The effect

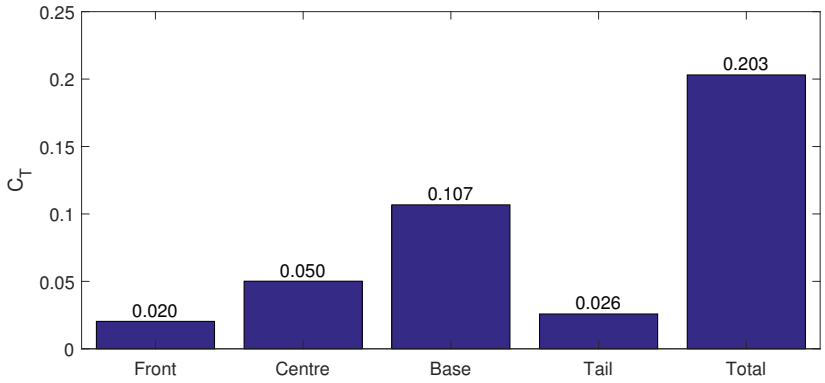

Figure 3.9: **Drag contributions of the GETS model with tail. Full-scale,** $V = 25m/s$**,** $Re = 5.1 \cdot 10^6$

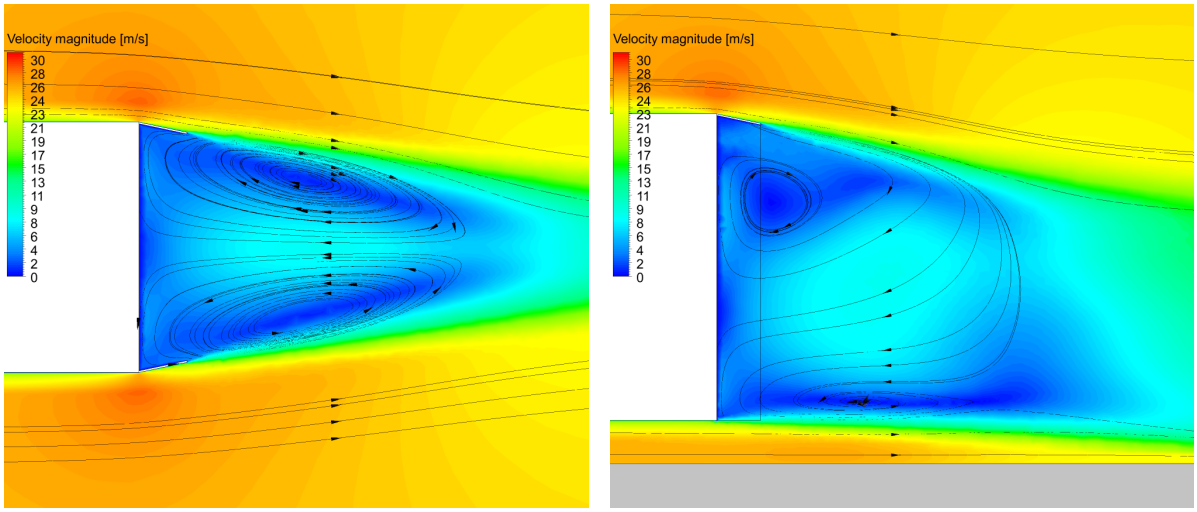

(a) Top view, z = 2m

(b) Side view, symmetry plane

Figure 3.10: **Velocity magnitude and streamlines in the wake of the baseline model**

of the change in scale on the drag of the GETS and baseline model and its contributions is presented in figure 3.11. The drag coefficient of both the GETS and the baseline model is higher in the 1/8-scale simulation compared to the full-scale. The higher drag of the scale model is caused by the higher contributions of the front and centre portion. Though what is interesting is that the contributions at the rear-end of the model, which are of interest in this study, do not significantly change with the scale. The base drag of the full-scale GETS model is 5 drag counts lower than the 1/8-scale model, as can be seen in table 3.2. The difference between the combined base and tail drag between the scaled and full-scale baseline model is just 2 drag counts. In the 1/8 scale as well as the full-scale simulation installing the tail on the GETS model has no effect on the drag contribution of the front and centre.

This indicates that in absolute sense the drag reduction achieved by a tail found in a scaled simulation can also be expected to be found on a full-scale truck. However, one should be careful when presenting a drag reduction as a percentage, as this will not translate to the full-scale when other drag contributions change. This is even more true for simulations on a generic vehicle model like the one used in this study. A real truck with a tractor-trailer gap, rotating wheels and axles, mirrors and many other geometric details will have a higher drag coefficient. Therefore the relative drag reduction of a tail on such a truck will be lower than what is found for the GETS model. As the drag reduction devices under investigation in this study only impact the rear drag contributions of the model, the contributions

of the front and centre will be omitted from bar graphs of drag contributions. This makes it easier to compare between simulations that are performed on a model of a different scale. The model scale will always be stated when presenting results in this thesis.

Table 3.2: **Comparison of the drag contributions of the GETS and baseline model at 1/8-scale and full-scale,** $V = 25m/s$

		Front	Centre	Base	Tail	Total	ΔC_T [DC]	ΔC_T [%]
1/8-scale	GETS	0.052	0.072	0.189		0.313	-	-
$(Re = 0.6 \cdot 10^6)$	Baseline	0.056	0.070	0.106	0.025	0.257	56	17.3 %
Full-scale	GETS	0.021	0.049	0.182		0.253	-	-
$(Re = 5.1 \cdot 10^6)$	Baseline	0.020	0.050	0.107	0.026	0.203	50	19.7 %

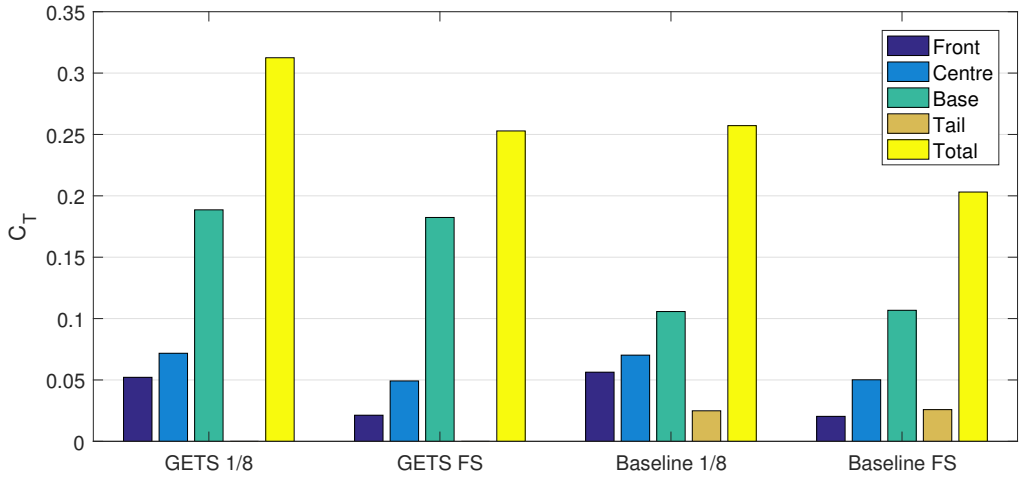

Figure 3.11: **Comparison of the drag contributions of the GETS and baseline model at 1/8-scale** $(Re = 0.6 \cdot 10^6)$ **and full-scale** $(Re = 5.1 \cdot 10^6)$**,** $V = 25m/s$

Changing the scale of the simulations has an influence on the boundary layer properties, which are listed in table 3.3. It can be seen that due to the lower Reynolds number in the 1/8-scale simulation, the relative thickness $(0.99u_0)$, as well as the displacement and momentum loss thickness of the boundary layer are higher. The normalised velocity profiles on the top side of the 1/8-scale and full-scale baseline model, $0.2L_m$ upstream of the base are shown in figure 3.12. Here it can be seen that the full-scale boundary layer profile is slightly 'fuller'. This translates to a higher shape factor, which is defined as $H = \delta^*/\theta^*$. Also visible in figure 3.12 is the way the boundary layers are modelled by Fluent using wall functions, with a clear linear sub-layer and log-law region. In the 1/8-scale simulation, the velocity profile in the log-law region is not entirely smooth, which is why the number of inflation layers was increased in later simulations. Ultimately the scale effects on the boundary layer properties result in the 1/8-scale simulation having more viscous drag.

Table 3.3: **Boundary layer properties on the top side,** $0.2L_m$ **upstream of the base of the 1/8-scale and full-scale baseline model,** $V = 25m/s$

	Re [-]	δ/h	δ^*/h	θ^*/h	H
1/8 Scale	$0.6 \cdot 10^6$	0.1	0.014	0.010	1.41
Full-scale	$5.1 \cdot 10^6$	0.056	0.009	0.006	1.45

The total drag coefficient of the GETS and the baseline model is split up into the viscous and pressure drag components at both scales in figure 3.13. It is clear that for all models the pressure is the main

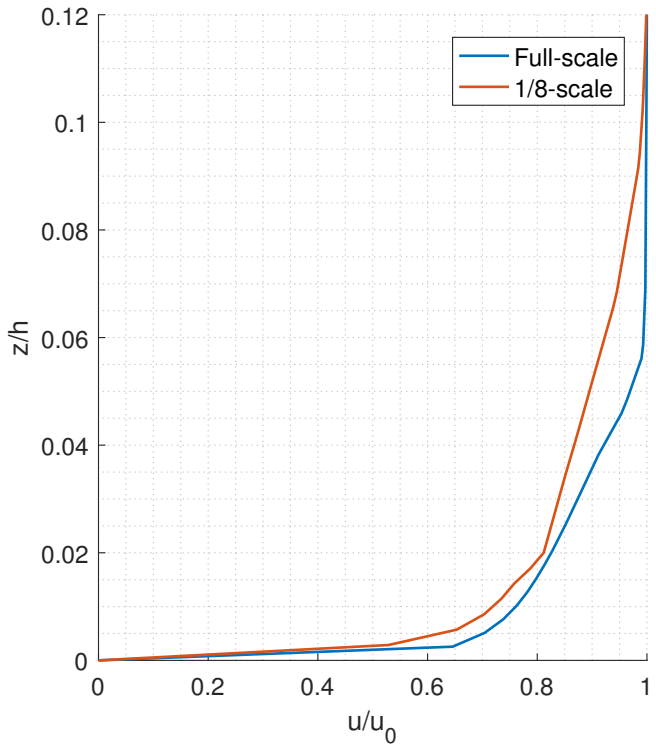

Figure 3.12: **Comparison of the boundary layer profile on the top side of baseline model $0.2L_m$ before the base at 1/8-scale $(Re = 0.6 \cdot 10^6)$ and full-scale $(Re = 5.1 \cdot 10^6)$, $V = 25m/s$**

source of drag. As can be seen in table 3.4, when moving from a 1/8-scale to a full-scale simulation both the pressure and the viscous drag decrease, but the percentage of pressure drag increases. The change in pressure drag is related to the front part of the model, while the viscous contribution originates from the large centre portion of the model. The tail on the baseline model reduces the pressure drag, while hardly adding any viscous drag. The latter might be explained by the fact that the slant angle of the tail is $12°$, which is close to the maximum angle the flow can deflect without separating. When the flow is on the verge of separation the coefficient of skin friction drops to zero, so this would explain the low viscous drag. Besides that the additional wetted area of the tail is small compared to the rest of the GETS model. The pressure drag originating from the base of the model is unaffected by scale effects because the sharp blunt edge of the GETS model results in a fixed separation point. So there is no transition to a different drag state as the Reynolds number is increased, like for a cylinder for example.

Table 3.4: **Pressure and viscous drag components of GETS and baseline model, 1/8-scale $(Re = 0.6 \cdot 10^6)$ and full-scale $(Re = 5.1 \cdot 10^6)$, $V = 25m/s$**

		Pressure	Viscous	Total	Reynolds nr
1/8-scale	GETS	0.232 (74.4%)	0.081 (26.1%)	0.313	$0.6 \cdot 10^6$
	Baseline	0.177 (68.7%)	0.081 (31.3%)	0.257	
Full-scale	GETS	0.198 (78.1%)	0.055 (21.9%)	0.253	$5.1 \cdot 10^6$
	Baseline	0.146 (71.6%)	0.058 (28.4%)	0.203	

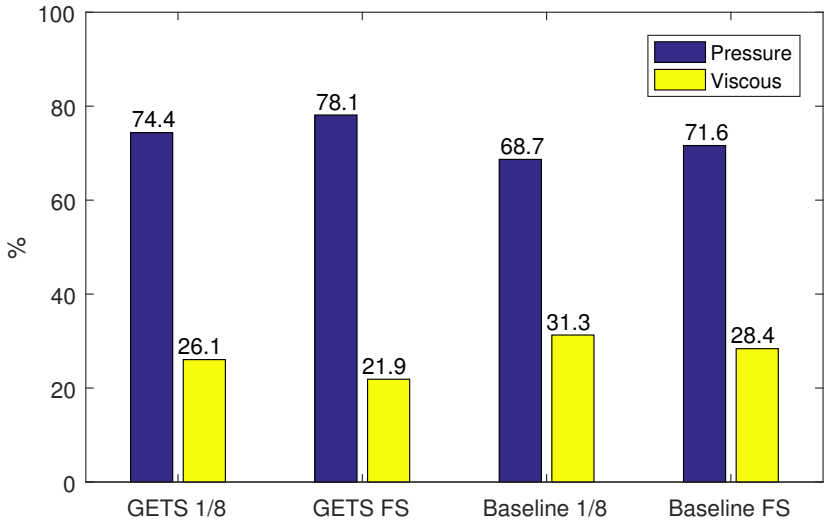

Figure 3.13: **Viscous and pressure drag components of the GETS and baseline model at 1/8-scale** $(Re = 0.6 \cdot 10^6)$ **and full-scale** $(Re = 5.1 \cdot 10^6)$**,** $V = 25m/s$

3.3. Guide vane

The guide vane configurations are created by extruding an airfoil profile along the three sides of the tail to form a 'U-shape'. In the simulations the guide vane 'hovers' a certain height above the tail and the corners are rounded with a radius equal to this height. Initially the longitudinal position of the vane is kept constant with the leading edge of the profile located right at the trailing edge of the tail. The design parameters of the guide vane that can be varied are the airfoil profile, the incidence angle, the gap height and the chord length, as was discussed in subsection 2.2.1. Note that the incidence angle is defined relative to the vehicle x-axis, which means that the chord line of a guide vane with $\alpha = 12°$ is parallel with the tail. Fig. 3.14 shows the streamlines around the GETS model fitted with a tail and a guide vane.

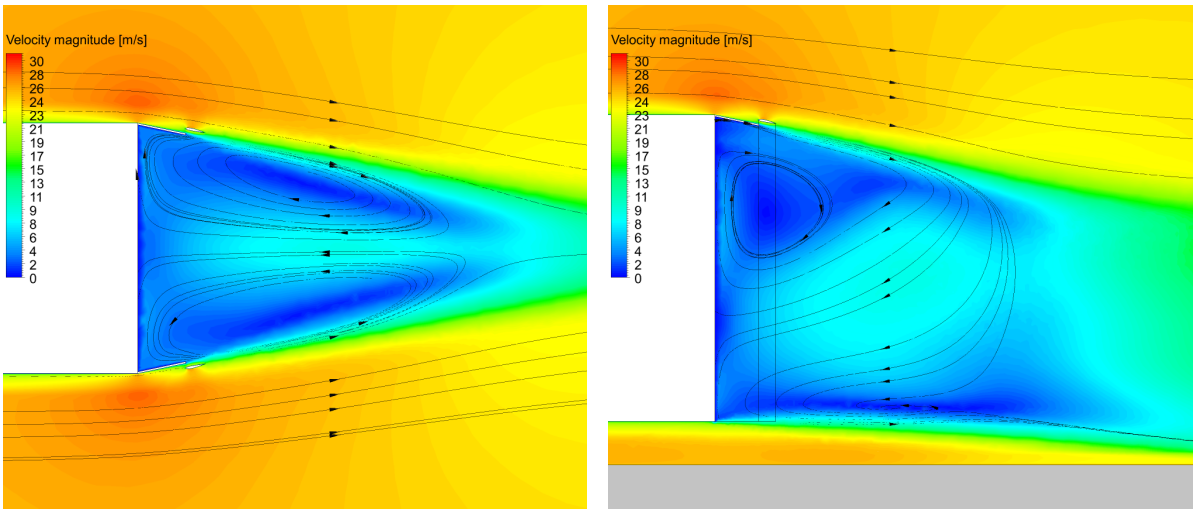

(a) Top view, z = 2m

(b) Side view, symmetry plane

Figure 3.14: **Velocity magnitude and streamlines in the wake of the GETS model with a tail and a NACA 2412 guide vane,** $\alpha = 14°$**,** $c = 0.4L_t$ **and gap height** $h_{gap} = 0.1L_t$ **. Full-scale,** $V = 25m/s$**,** $Re = 5.1 \cdot 10^6$

3.3.1. Incidence angle

The initial simulations are performed at a 1/8-scale with a NACA6415 airfoil profile for all configurations. This airfoil is selected because it was found by van Straaten to be the most effective for a guide vane placed at the trailing edge of the GTS model. [67] He found the highest drag reduction for an incidence angle of $\alpha = 12°$. It is important to note that the guide vane of van Straaten had a full-scale length of 500mm and was placed at the trailing edge of the GTS model, making it very similar in size to the tail used in this study. To investigate the optimal incidence angle for a guide vane placed on the trailing edge of a tail, an initial chord length of 1/5 the tail length (12.5mm for the 1/8 scale model) was selected. Van Straaten concluded that for the guide vane to be effective, high lift was more important than a high L/D ratio. [67] Therefore it was expected that the guide vane placed on the trailing edge of the tail would have to be placed at an angle with respect to the local flow. Simulations were performed at various incidence angles, mostly larger than $12°$. It can be seen in figure 3.15 that with increasing incidence angle the base drag steadily decreases. The drag of the tail is lower than for the baseline model, but does not change much with incidence angle. The drag of the guide vane itself increases with increasing incidence angle. However, surprisingly the lowest combined rear drag contribution is found for an angle of $\alpha = 8°$. At large incidence angles the additional drag on the guide vane itself does not outweigh the reduction in base drag that the vane causes. This indicates that unlike the guide vane of van Straaten, the L/D of the guide vane is more important than high lift alone. The drag reduction with respect to the baseline model that is achieved by the guide vane with $c = 0.2L_t$ at various incidence angles is presented in figure 3.16. The maximum drag reduction is 6.4 drag counts and is found at $\alpha = 8°$.

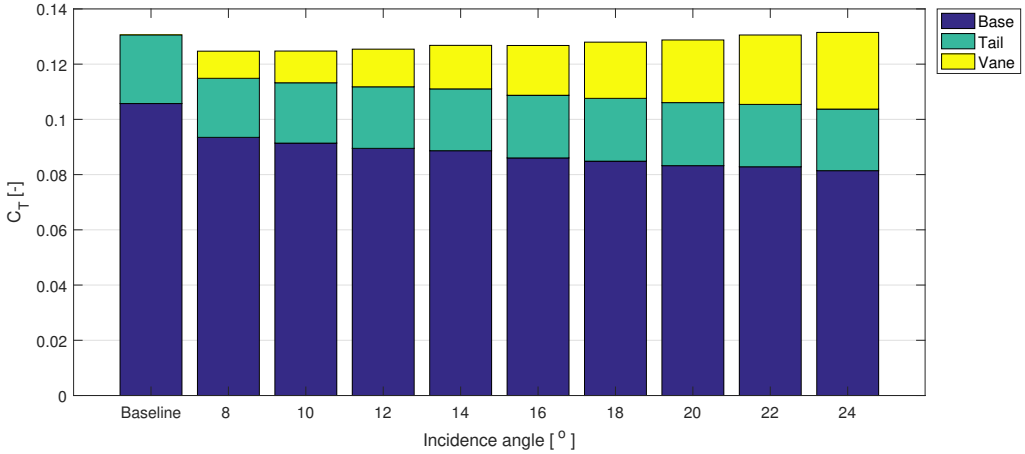

Figure 3.15: **Rear drag contributions of baseline model and NACA6415 airfoil at various incidence angles,** $c = 0.2L_t$**,** $h_{gap} = 0.2L_t$ **1/8-scale,** $V = 25m/s$**,** $Re = 0.6 \cdot 10^6$

3.3.2. Chord length

Given that aerodynamic devices for HDV's have a limited allowed length behind the vehicle as was explained in chapter 1, it is desirable to achieve a large drag reduction with the shortest possible guide vane. However, this research aims to validate the numerical results in the wind tunnel and the short vane simulated in subsection 3.3.1 would be difficult to produce at a 1/8-scale. With a chord length of 12.5mm and 15% thickness the guide vane would be less than 2mm thick. It was foreseen that this was too thin for a 3D-printed prototype to provide the required stiffness. Therefore a guide vane with twice the chord length ($c = 25mm = 0.4L_t$) was simulated at various incidence angles. Fig. 3.16 shows the drag reductions achieved by the long and short guide vane. Both curves show similar behaviour, but the curve of the $c = 0.4L_T$ guide vane is steeper and leads to a smaller drag reduction at the optimal angle of $\alpha = 8°$. The curves in figure 3.16 show some non-smooth behaviour between $10° < \alpha < 16°$. This is not to be expected when assuming a linear increase in lift coefficient with angle of attack and

a quadratic drag polar. It is believed that the non-smooth behaviour is caused by an insufficient mesh density on the leading edge of the guide vane surface. This leads to a sudden shift of the stagnation point from the bottom to the top side of the airfoil, which is supposed to be smooth for an airfoil with a rounded nose. This non-smooth behaviour is amplified for the larger guide vane.

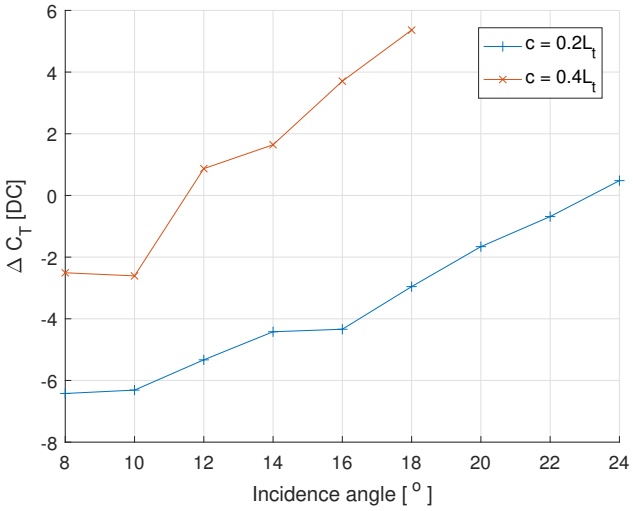

Figure 3.16: **Effect of chord length on the drag reduction of a NACA6415 profile guide vane with $h_{gap} = 0.2L_t$ at various incidence angles, 1/8-scale, $V = 25m/s$, $Re = 0.6 \cdot 10^6$**

When comparing the rear drag contributions of the configurations with the large guide vane in figure 3.17 with the same plot for the small vane in figure 3.15 the effect of changing the chord length can be explained. It can be seen that the drag contribution of the guide vane is approximately twice as large for the vane with chord length $c = 0.4L_t$ compared to the vane with $c = 0.2L_t$. This is logical as the chord length has doubled, which is proportional to the forces acting on the vane. The base drag contribution is smaller due to the larger guide vane, but this reduction is smaller than the increase in vane drag. So the increase in chord length has a larger negative effect on the vane drag than the additional base drag reduction it causes, which makes it not beneficial to install a larger vane. Especially when considering the length restrictions on aerodynamic add-on devices for HDV's, it is better to use a small guide vane.

3.3.3. Gap height

Next the effect of changing the gap height was investigated for both chord lengths and a fixed incidence angle of $\alpha = 10°$. When looking at figure 3.18, it is clear that a lower gap height leads to a larger drag reduction. The combination of the large vane and the largest gap height even leads to an increase in drag with respect to the baseline model. At the smallest gap height the difference between the large and small chord length diminishes and both vanes yield approximately the same drag reduction. It was argued by van Straaten that the guide vanes should be placed inside the boundary layer region. [67] He simulated a drag reduction on a 1/8-scale GTS model when reducing the gap height from 18.75mm to 4.85mm. Van Raemdonck performed full-scale circuit tests on a semi-truck fitted with guide vanes. The boundary layer profile was measured and the thickness was found to be larger than what would be expected from plate theory. A lower fuel consumption was measured when the gap height was increased from 15 to 20cm. [65] The thickness of the boundary layer was observed to vary depending on weather conditions, driving direction and location on the trailer. This shows on one hand the importance of placing the guide vane inside the boundary layer and on the other hand the difficulty of predicting the optimal position.

Looking at the rear drag contributions of the configurations plotted in figure 3.19 provides some more

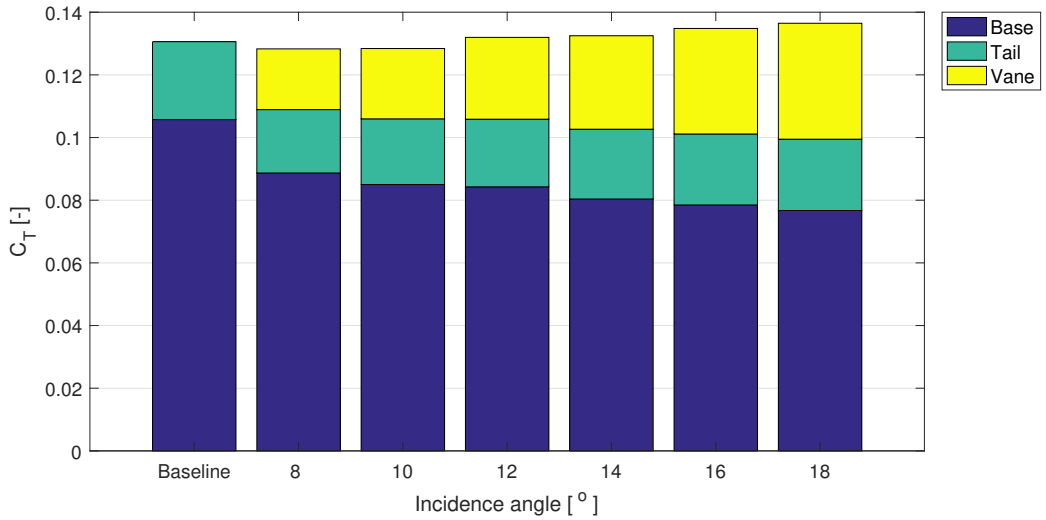

Figure 3.17: **Rear drag contributions of baseline model and NACA 6415 guide vane at various incidence angles,** $c = 0.4L_t$ **and gap height** $h_{gap} = 0.2L_t$**, 1/8-scale,** $V = 25m/s$**,** $Re = 0.6 \cdot 10^6$

insight in the effect of changing the chord and the gap height. It is clearly visible that the larger chord length results in a lower base drag contribution at the expense of a higher vane drag. An increase in gap height has very little effect on the base and tail drag contributions, but causes an increase in vane drag. This implies that when the guide vane is close to the tail surface and therefore more immersed in the boundary layer, this does not affect the vane's ability to direct the flow inwards. It does, however, encounter a lower local flow velocity and therefore produces a lower drag force. At the lowest gap height the higher vane drag of the vane with $c = 0.4L_t$ is nearly counteracted by the vane drag reduction caused by the lower gap height.

As the guide vane is placed inside the boundary layer of the GETS model, the ideal gap height depends on the boundary layer thickness. Therefore this is very dependent on Reynolds number effects. As the Reynolds number increases and the relative boundary layer thickness becomes lower, the vane should also be placed closer to the tail to have the same positions with respect to the boundary layer. As it was shown that a low gap height provides the largest drag reductions and taking this Reynolds number effect into consideration, all full-scale simulations were performed with the lowest gap height of $h_{gap} = 0.1L_t$.

3.3.4. Airfoil variation

In an attempt to find larger drag reductions, a different airfoil profile was used on the guide vane. The choice for the turbulent, high-lift NACA 6415 was based on the work of van Straaten, who argued that high lift was more important than L/D to reduce the drag of an HDV. But in the configuration where the guide vane is combined with a tail, it was found in subsection 3.3.1 that the highest drag reductions are found when the guide vane has a low angle of incidence with respect to the local flow. Therefore it was suspected that by selecting an airfoil with a lower drag coefficient better results can be achieved. The airfoil is still operating in the turbulent boundary layer around the GETS model, so it is not possible to make use of a 'low drag bucket' laminar airfoil to reduce the drag of the of the profile. Consequently the airfoil should still be designed for turbulent flow. The choice was made to select an airfoil from the same family of 4-digit NACA airfoils, but to reduce the maximum thickness and camber. The NACA 2412 airfoil was selected for this. The choice for this particular airfoil over another airfoil with lower camber and thickness than the NACA 6415 is arbitrary, but the point is to proof the potential of lowering the drag by changing the profile rather than finding an optimal airfoil. The two airfoil profiles that were used in the simulations are presented in figure 3.20.

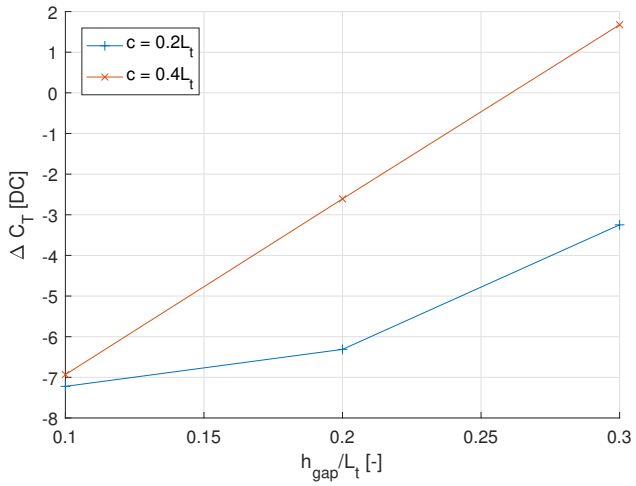

Figure 3.18: **Effect of chord length on the drag reduction of a NACA6415 guide vane with $\alpha = 10°$ at various gap heights, 1/8-scale,** $V = 25m/s$, $Re = 0.6 \cdot 10^6$

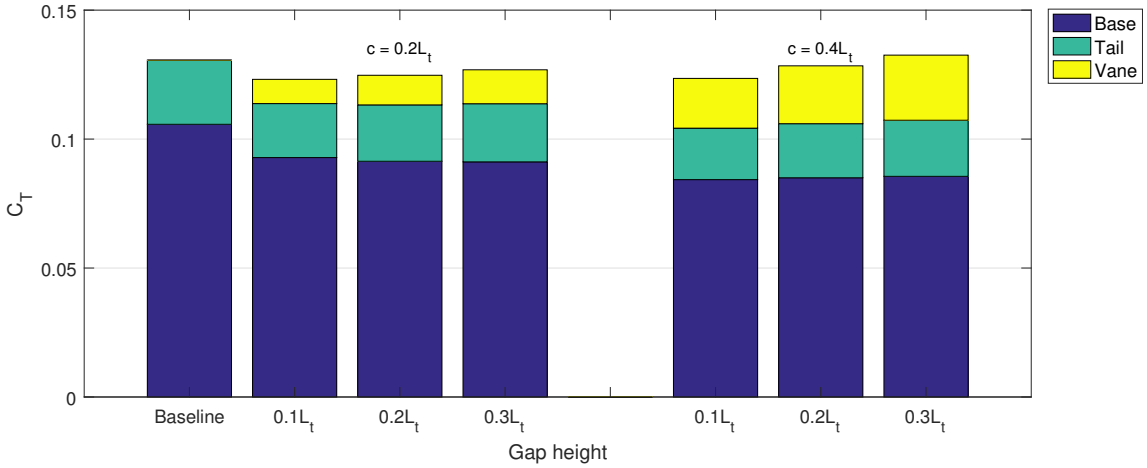

Figure 3.19: **Rear drag contributions of baseline model and NACA6415 guide vane at various gap height and chord lengths, 1/8-scale,** $V = 25m/s$, $Re = 0.6 \cdot 10^6$

The 2D lift and drag polars of the NACA 6415 and NACA 2412 airfoils as predicted by XFOIL are presented in figure 3.21, at a Reynolds number of $3.3 \cdot 10^5$ based on the chord length of the vane and the freestream velocity. By default XFOIL predicts the location of transition using the e^n method, but at the rear-end of an HDV the flow is assumed to be turbulent anyway. Therefore the flow in XFOIL is 'tripped' at the leading edge to have turbulent flow along the chord length. Due to the turbulence model in the RANS equations the flow is also turbulent in the entire domain, so these polars can be used as a reference. However, one should be cautious to extrapolate the results of these polars to the performance of the guide vane in the proximity of the tail. The guide vane is operating in the boundary layer of the tail, so will be subjected to a lower velocity than the freestream. Furthermore the flow behind the GETS model is curved inward by the tail, so the local angle of attack of the guide vane should be considered. This angle also depends on the position of the guide vane with respect to the tail and 3D flow effects. What is useful to read from figure 3.21 however, is that the drag of the NACA2412 profile is lower than the NACA 6415 airfoil over the whole range of angles of attack. The NACA 6415 airfoil is able to achieve a higher maximum lift coefficient and higher lift at 0 angle of attack.

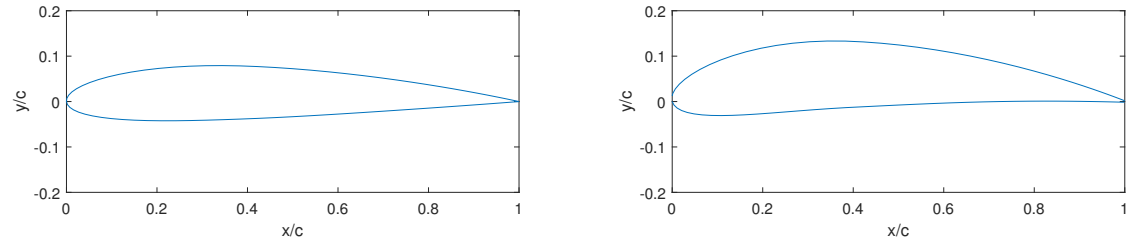

(a) NACA 2412 (b) NACA 6415

Figure 3.20: **Comparison of NACA 2412 and NACA 6415 airfoils**

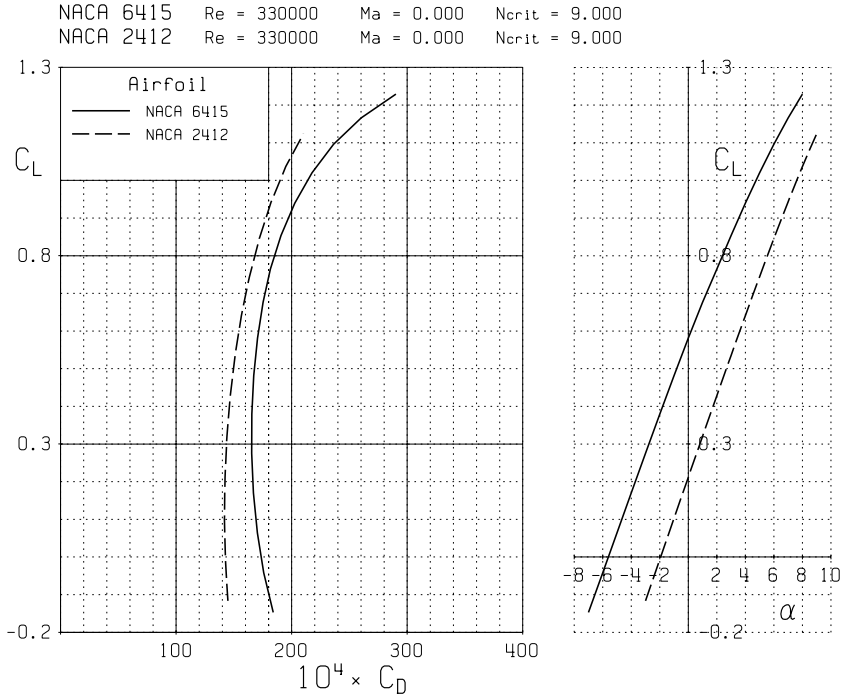

Figure 3.21: **Turbulent lift and drag polars of NACA 6415 and NACA 2412 airfoils calculated by XFOIL**

The results of changing the airfoil profile of the guide vane in terms of drag reduction can be seen in figure 3.22. These simulations are performed on a full-scale model and consequently the drag reductions are with respect to the full-scale baseline model. The chord length is 200mm or $0.4L_t$ and the smallest gap height of $h_{gap} = 0.1L_t$ is used. The panel density on the guide vane has been refined with respect to 1/8-scale simulations presented in figure 3.16. It can be seen that this leads to smooth, parabolic curves as would be expected.

The maximum drag reduction achieved by the NACA 6415 airfoil guide vane found in the full-scale simulations is 1.3 drag counts and occurs at an incidence angle of $6°$. For the less cambered NACA 2412 profile this optimum lies around $\alpha = 8°$ and a 3 drag count reduction is achieved. Assuming that the flow in front of the guide vane is aligned to the tail, which has an angle of $12°$, these optimum guide vane orientations have a slightly negative angle with respect to the local flow. Because they have a cambered profile they can still generate lift and direct flow into the near wake at this angle. When looking at the airfoil polars in figure 3.21 it can be seen that at these negative angles the airfoils produce zero or a low amount of lift and the profile drag coefficient is at a minimum. This confirms what was stated earlier, that when a guide vane placed at the trailing edge of a tail, low drag is more important than high lift.

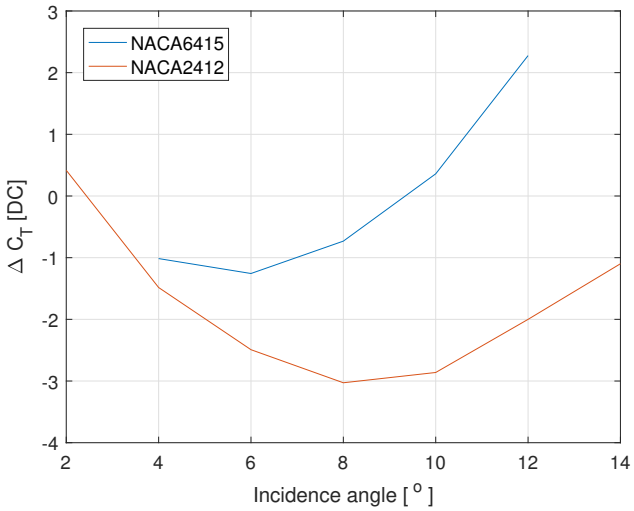

Figure 3.22: **Effect of airfoil profile on the drag reduction of a guide vane with chord length $c = 0.4L_t$ and gap height $h_{gap} = 0.1L_t$ at various incidence angles, full-scale, $V = 25m/s$, $Re = 5.1 \cdot 10^6$**

The rear drag contributions of the guide vane configurations with the NACA 6415 and NACA 2412 airfoils are presented in figures 3.23 and 3.24 respectively. It can be seen that as expected from the airfoil polars in figure 3.21 the vane drag contribution is smaller for the NACA 2412 airfoil. The more cambered NACA 6415 airfoil produces more drag, but also causes a higher base drag reduction at the same incidence angle. The tail contributions of both airfoils are approximately equal and increase with incidence angle. However, at low incidence angles the drag contribution of the tail is much lower than the tail drag of the baseline model.

The guide vane configuration with the NACA 2412 airfoil and incidence angle $\alpha = 4°$ is interesting. Due to the large negative angle of attack with respect to the local airflow the base drag component is actually slightly higher than for the baseline model. But the presence of the guide vane reduces the tail drag component, which combined with the low vane drag leads to a lower total drag. This is counterintuitive as the principle of the combined tail and guide vane design was to lower the aerodynamic drag by reducing the base drag. So it is striking to see that the NACA 2412 guide vane at $\alpha = 4°$ causes a larger drag reduction than the vane at $\alpha = 14°$ even though it increases the base drag contribution.

To better understand the working principle of the guide vane in combination with a tail it is useful to look at the C_p distribution on the base. The effect of the guide vane incidence angle on the base pressure is shown in figure 3.25, where the C_p distribution is averaged over horizontal and vertical lines respectively. Here it can be seen that the tail yields a large base pressure increase with respect to the single GETS model. The effect of the guide vanes with respect to the baseline model is relatively small, which is also caused by the small incidence angles that have been simulated for this airfoil profile. Furthermore due to the lack of a tail panel or guide vane on the lower edge of the base, installing a tail and increasing the vane incidence angle shifts the regions of low and high pressure down with respect to the single GETS model. The distribution in the horizontal plane shown in the right figure reveals that the guide vanes with $\alpha = 8°$ and $12°$ yield a constant C_p increase over the entire width. In the vertical plane the effect of changing the vane incidence angle is slightly more complex, with the increase in base pressure being higher in the top halve of the base. The guide vane with $\alpha = 4°$ causes a very small pressure increase on the top halve of the base, while lowering the pressure close to the road. In the right plot of figure 3.25, it can be seen that in the horizontal plane it yields a very small decrease in C_p. This causes the aforementioned base drag increase of this configuration, as was shown in figure 3.24.

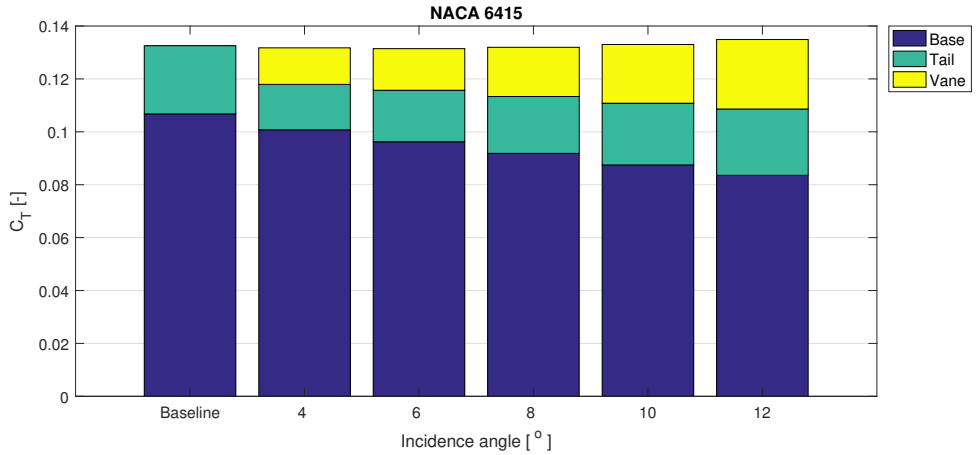

Figure 3.23: **Rear drag contributions of baseline model and NACA 6415 guide vane at various incidence angles,** $c = 0.4L_t$ **and gap height** $h_{gap} = 0.1L_t$**, full-scale,** $V = 25m/s$**,** $Re = 5.1 \cdot 10^6$

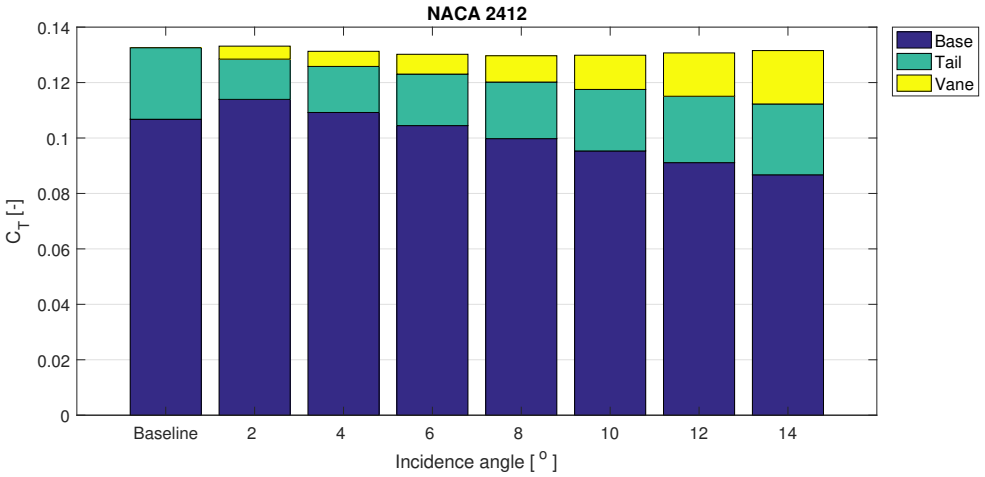

Figure 3.24: **Rear drag contributions of baseline model and NACA 2412 guide vane at various incidence angles,** $c = 0.4L_t$ **and gap height** $h_{gap} = 0.1L_t$**, full-scale,** $V = 25m/s$**,** $Re = 5.1 \cdot 10^6$

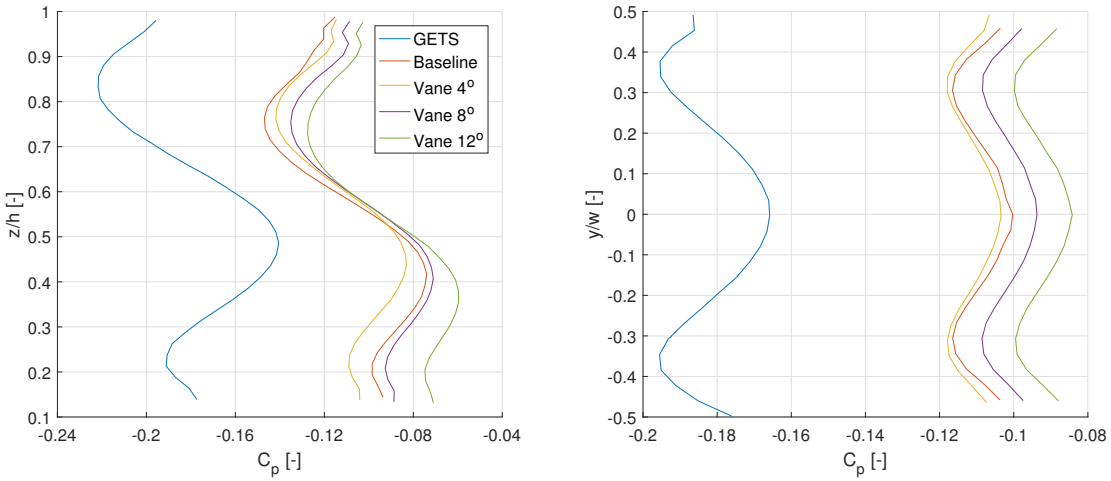

Figure 3.25: **Comparison of the** C_p **distribution on the base surface in the vertical (left) and horizontal (right) plane of the GETS and baseline model and NACA 2412 guide vane at various incidence angles,** $c = 0.4L_t$ **and gap height** $h_{gap} = 0.1L_t$**, full-scale,** $V = 25m/s$**,** $Re = 5.1 \cdot 10^6$

3.3.5. Effect of closing the tail cavity

The tail that is used as a baseline in this study consists of three panels that form a tapered elongation of the trailer. Inside of these panels is a cavity where the wake flow recirculates in. Other tail designs exist, however, where the tail shape is formed by an inflatable device. In this case the tail forms a solid shape and there is no cavity. For example, Leuschen and Cooper [36] performed full-scale wind tunnel tests on a number of commercially available HDV drag reduction devices, including an inflatable tail. In a scaled wind tunnel experiment, van Raemdonck [65] analysed open and closed-cavity tails with the same length and slant angle. He found that the open tail cavity resulted in a larger drag reduction for both the GETS model and a more realistic semi-trailer model, but that the differences were quite small. Though understandably, the flow structure in the wake and the locations of the vortex cores can change when the tail cavity is closed. Therefore it can be imagined that the effect of the guide vane changes with respect to an open cavity configuration, due to a different interaction with the wake flow.

A side view of the streamlines in the symmetry plane behind the GETS model with a tail featuring an open and closed cavity and a guide vane is presented in figure 3.26. When the tail cavity is closed, the bottom vortex core moves slightly more downstream, while the reattachment point in the wake does not change. The most notable difference between the wake structures with and without the closed tail cavity is that the top vortex core is translated upwards and downstream. The result is that it lies closer to the guide vane, which influences the interaction between the two.

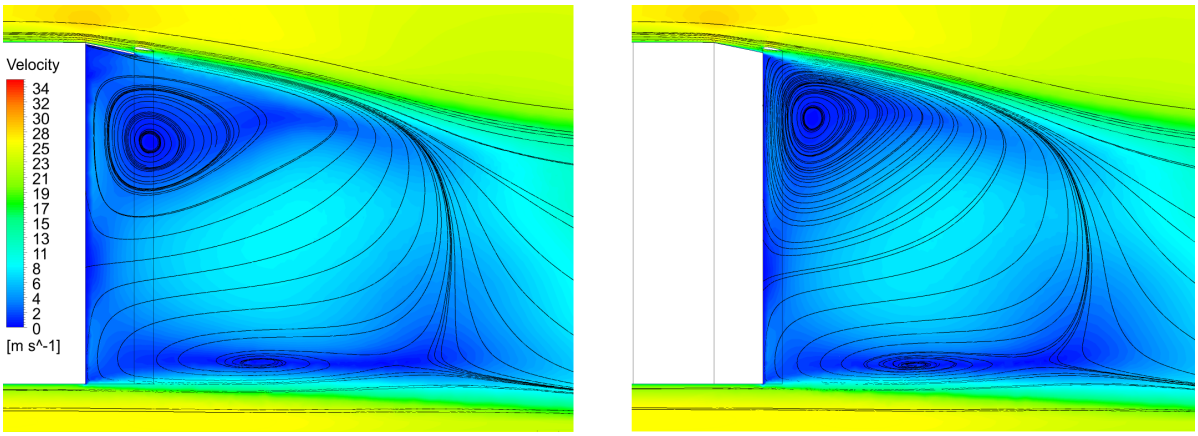

Figure 3.26: **Streamlines in the wake behind the full-scale GETS model with a tail featuring an open (left) and closed (right) cavity and a guide vane, as seen from the symmetry plane.** $V = 25m/s, Re = 5.1 \cdot 10^6$

The effect of closing the tail cavity on the rear drag contributions is shown in figure 3.27. Note that due to the closing of the cavity, the definitions of the various zone has slightly changed. For the zones with a closed cavity (labelled CC), the tail now only consists of the of the slanted outer faces. The base is the rearmost surface of the model, normal to the x-axis. Which means that compared to the baseline tail with a cavity, it is smaller and translated downstream. When comparing the two configurations without a guide vane, it can be seen that closing the cavity mainly 'shifts' some drag from the base to the tail. The decrease in base drag is caused by the smaller base surface, while the increase in tail drag is caused by the loss of the thrust component of the inside tail panels of the baseline tail. With $C_T = 0.204$, the drag of the Baseline CC configuration is 1 drag count higher the Baseline configuration with a cavity. This is in line with the observation of van Raemdonck [65] that closing the tail cavity does not yield a larger drag reduction. When the guide vane is added to the trailing edge of the closed cavity tail, it yields almost a 9 drag count reduction of the base drag. This particular guide vane configuration yields a base drag reduction of 7 drag counts for the standard tail. The reduction of the tail drag component caused by the guide vane is the same as for the tail with a cavity, while the vane drag is slightly larger. Ultimately, the guide vane with a NACA 2412 profile and an incidence angle of $8°$ yields the same drag

coefficient of $C_T = 0.200$ for the standard and closed cavity tail.

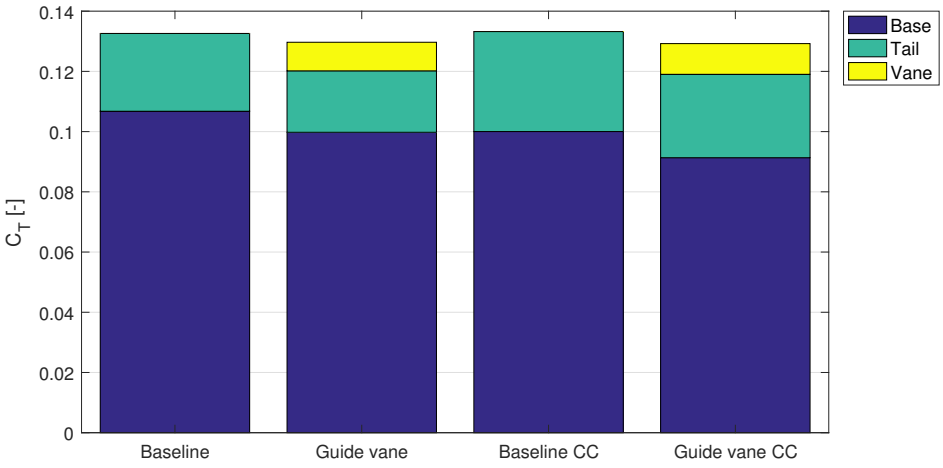

Figure 3.27: **Influence of a tail with a closed cavity (CC) on the rear drag contributions of the baseline model and the NACA 2412 $\alpha = 8°$ guide vane,$c = 0.4L_t$ and $h_{gap} = 0.1L_t$. $V = 25m/s, Re = 5.1 \cdot 10^6$**

3.3.6. Effect of yaw angle

Up till now, all presented simulations were performed at $0°$ yaw angle. However, in reality it will often occur that a truck experiences a yaw angle with respect to the incoming flow. This can be caused by a wind velocity that is not aligned with the driving direction. This crosswind combined with the tangential flow velocity in the driving direction leads to a yaw angle. During road tests it was found that 88% of the time the yaw angle is between -10 and 10 degrees. [66] In this thesis the focus was first to find a drag reduction at $0°$ flow before investigating the performance at yaw angles. Due to limited time and computational resources only yaw angles between 0 and 6 degrees have been considered. Simulating larger yaw angles would require a different mesh where the inner refinement box is elongated on the leeward side to capture the flow that is shed to the side of the model. Generating a new mesh is time consuming and it was decided to use the available time for other ends.

The behaviour of the total drag and sideforce coefficient of the GETS model versus yaw angle is presented in figure 3.28. In the same figure the C_T of the baseline model and the best performing full-scale guide vane configuration at various yaw angles is given. This guide vane configuration has a NACA 2412 profile guide vane with an incidence angle of $\alpha = 8°$, a chord length of $c = 0.4L_t$ and a gap height of $h_{gap} = 0.1L_t$. As the yaw angle increases the drag of all models increases as well. The drag reduction that the tail provides for the GETS model is larger at a yaw angle of 6 degrees, so it can be said to improve the crosswind performance of the GETS model. The drag reduction that the guide vane provides with respect to the baseline model does not change with yaw angle. Even though the differences are small, this does indicate that the additional drag reduction that a guide vane adds to a tail translates to crosswind conditions. The value of C_S increases almost linearly with the yaw angle over this range. It can be seen in figure 3.28b that the tail slightly reduces the side force on the GETS model, but that the additional guide vane has no effect on this.

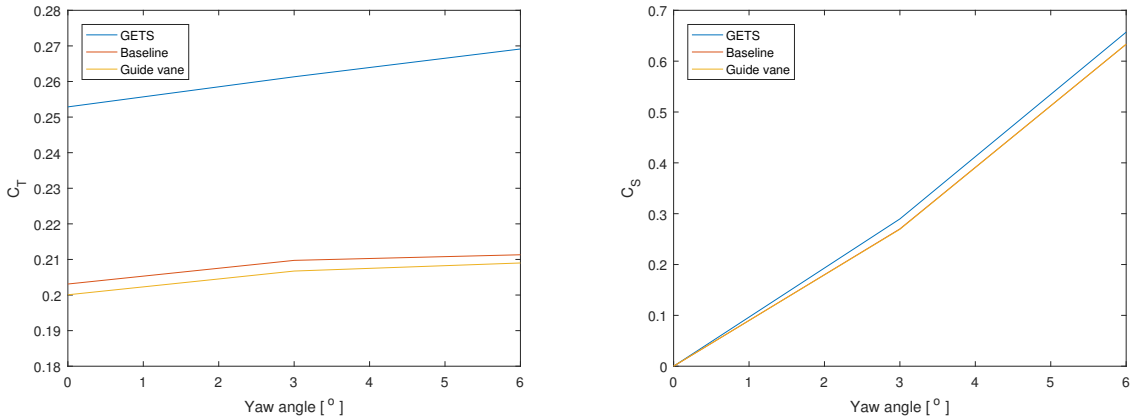

(a) Drag coefficient (b) Sideforce

Figure 3.28: C_T **and** C_S **of GETS, baseline and guide vane with chord length** $c = 0.4L_t$ **and gap height** $h_{gap} = 0.1L_t$ **at various yaw angles, full-scale,** $V = 25m/s$**,** $Re = 5.1 \cdot 10^6$

3.4. Slotted tail

The research into guide vanes in combination with a tail behind an HDV has shown that it is possible to reduce the base drag by guiding flow into the near wake region. However, an airfoil is a complex shape that is generally difficult to produce. Besides, the combined tail and guide vane configurations that were tested in this thesis are longer than what is currently allowed on the road in the EU. Therefore it would be preferred to improve the performance of a tail with a simpler shape and without making the tail longer. The research into tail designs featuring a slot aims to provide a solution for this. A number of slotted tail configurations were designed and simulated behind the 1/8-scale GETS model. Except for the final two configurations, all these tails have the same length as the baseline tail (62.5mm). An overview of the slotted tail designs that were tested is given in figure 3.29. These schematics show the cross-section of the tail that is extruded along the sides and top of the GETS model to form a tail with a slot. No structural connections between the tail panels have been modelled, so these tails actually consist of two separate parts. The idea behind the slotted tail was to direct more flow into the near wake than the baseline tail. Next to that it was be investigated whether the second tail panel can withstand a larger slant angle without separating, given that starts with a 'fresh' boundary layer.

Like for the guide vane configurations that were simulated, the slotted tails have no influence on the drag components of the front and centre of the GETS model, as can be seen in table 3.5. In figure 3.30 the rear drag contributions of the slotted tail configurations are presented next to that of the baseline tail. It can be seen that most slotted tail configurations are indeed able to reduce the base drag contribution. However, by doing so the tail drag contribution also increases. Especially the highly curved second tail plate of Slot9 and Slot10 causes a large reduction in base drag, but flow separation over the curved surface adds a lot more drag to the tail in return. Therefore an attempt was made to streamline these configurations to end up at Slot13 and Slot14. This slightly reduces the tail drag contribution, but still results in a much higher drag coefficient than the baseline tail. The net effect of adding a slot to the tail is negative in terms of drag reduction for almost all tails. The Slot1 and Slot11 configurations, that both feature a curved end of the first plate and a small vertical gap, have a zero net effect on the drag of the baseline model. It was found that rounding the front edge of the second tail plate sometimes has an effect on the drag. In the simulation the flow would separate over this edge and lead to higher tail drag. With rounding and possibly better positioning of the second element, configurations Slot1 and Slot11 might be able to yield a small drag reduction. However, for the rest of the research and mainly the wind tunnel experiment it was decided to focus on the guide vane as this shows more promise as a drag reduction device for HDV's.

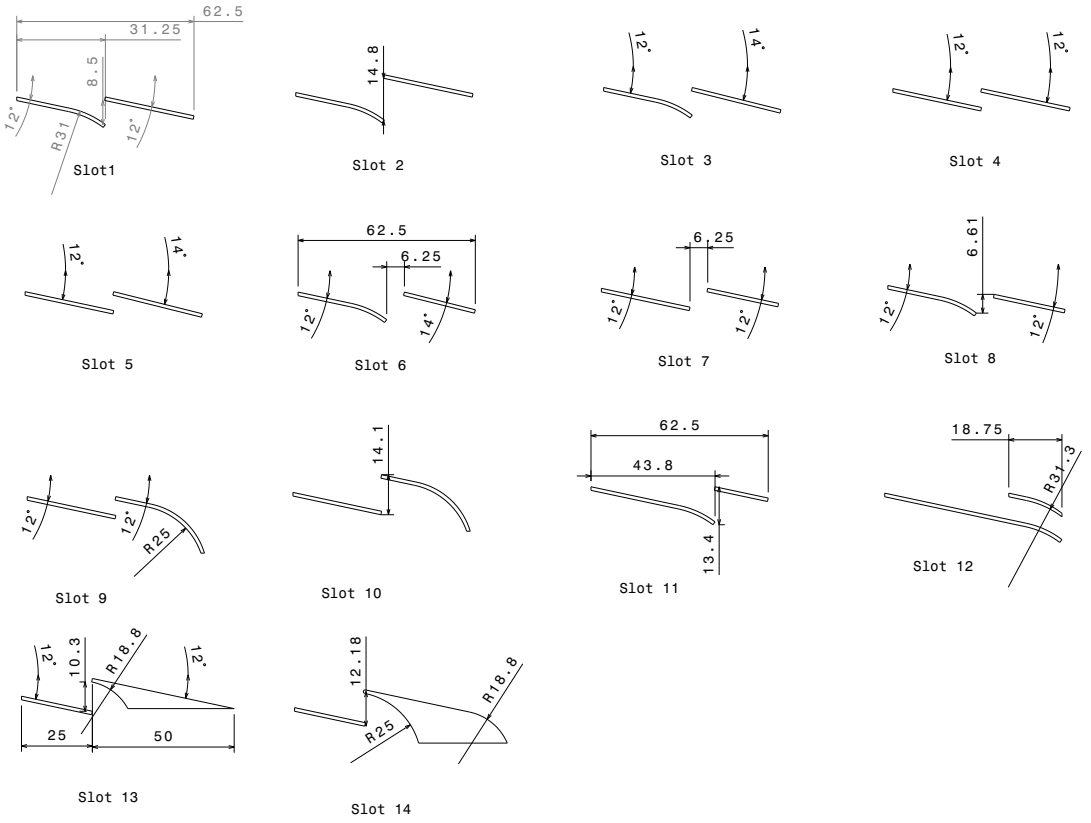

Figure 3.29: **Overview of simulated slot configurations**

Table 3.5: **Overview of of drag contributions of slotted tail configurations, 1/8-scale,** $V = 25m/s$**,** $Re = 0.6 \cdot 10^6$

	Description	Front	Centre	Base	Tail	C_T	$\Delta C_T[DC]$
Baseline	GETS with tail	0,056	0,070	0,106	0,025	0,257	
Slot1	Curved end of first plate	0,057	0,069	0,099	0,032	0,257	0,0
Slot2	Slot1 with bigger vertical gap	0,057	0,069	0,099	0,037	0,263	5,5
Slot3	Second plate $14°$	0,057	0,070	0,097	0,036	0,260	2,4
Slot4	Both plates flat, $12°$	0,057	0,069	0,102	0,031	0,259	1,8
Slot5	Both plates flat, second $14°$	0,058	0,069	0,102	0,034	0,262	4,8
Slot6	Slot 1 with horizontal gap	0,057	0,069	0,099	0,034	0,261	3,5
Slot7	Slot 4 with horizontal gap	0,058	0,069	0,104	0,029	0,259	1,8
Slot8	Slot6 with smaller vertical gap	0,057	0,070	0,105	0,027	0,260	2,5
Slot9	Large curvature second plate	0,058	0,069	0,095	0,061	0,283	25,9
Slot10	Slot9 with bigger gap	0,058	0,069	0,078	0,108	0,314	56,7
Slot11	Slot1 with second plate shorter	0,057	0,070	0,098	0,033	0,257	0,1
Slot12	turning vane at end	0,057	0,069	0,090	0,050	0,266	8,8
Slot13	'Streamlined' slot10	0,058	0,069	0,104	0,047	0,278	20,4
Slot14	Slot13 with more downwash	0,058	0,069	0,091	0,077	0,295	37,8

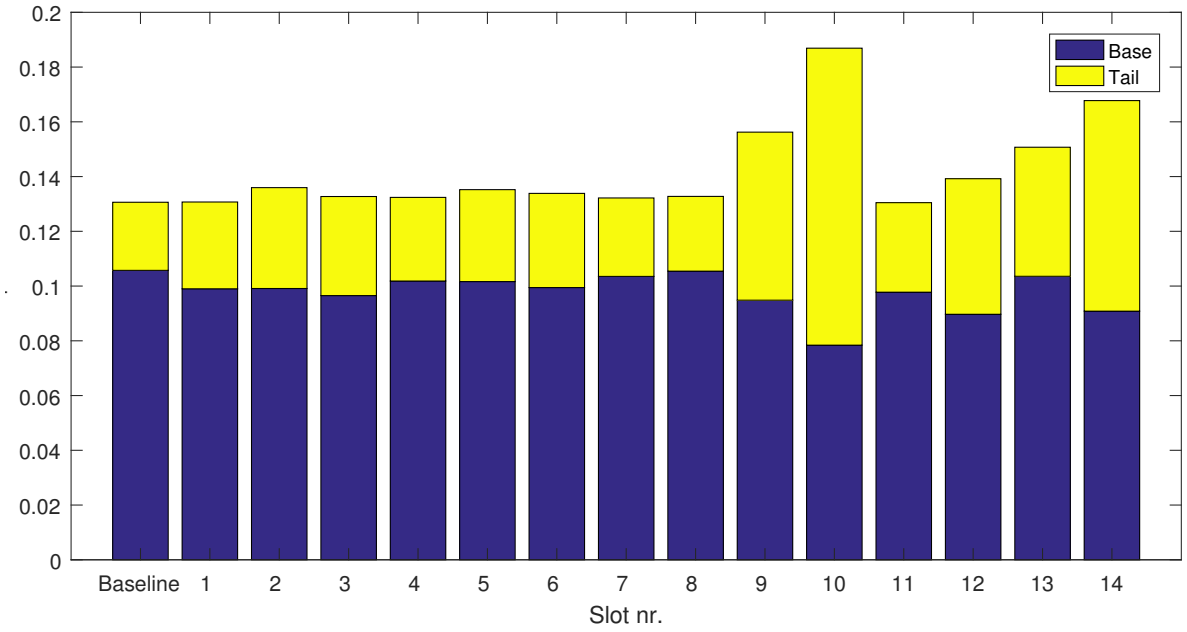

Figure 3.30: **Rear drag contributions of baseline model and slot configurations, 1/8-scale,** $V = 25m/s$**,** $Re = 0.6 \cdot 10^6$

4

Experimental set-up

No matter the advancements made in the capabilities of CFD simulations, wind tunnel testing remains an indispensable part of aerodynamic research. To validate the findings of the numerical simulations a wind tunnel experiment was conducted in the Open Jet Facility (OJF) of the TU Delft. A schematic of the OJF is given in figure 4.1. This wind tunnel campaign was performed in conjunction with a master thesis research investigating the unsteady flow around a platoon of HDV's. This chapter will describe the set-up of the experiment, as well as the steps taken in post-processing the acquired data.

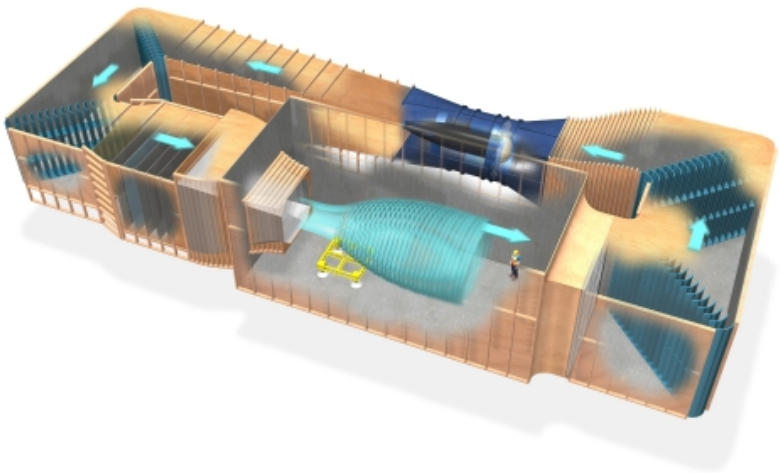

Figure 4.1: **Schematic of the TU Delft OJF facility source:TU Delft**

4.1. Wind tunnel model

A $1/8$ scaled version of the GETS model was designed and constructed to be used in the experiment. The model consists of three parts: the GETS model itself, a tail and a guide vane, which can be seen in figure 4.2

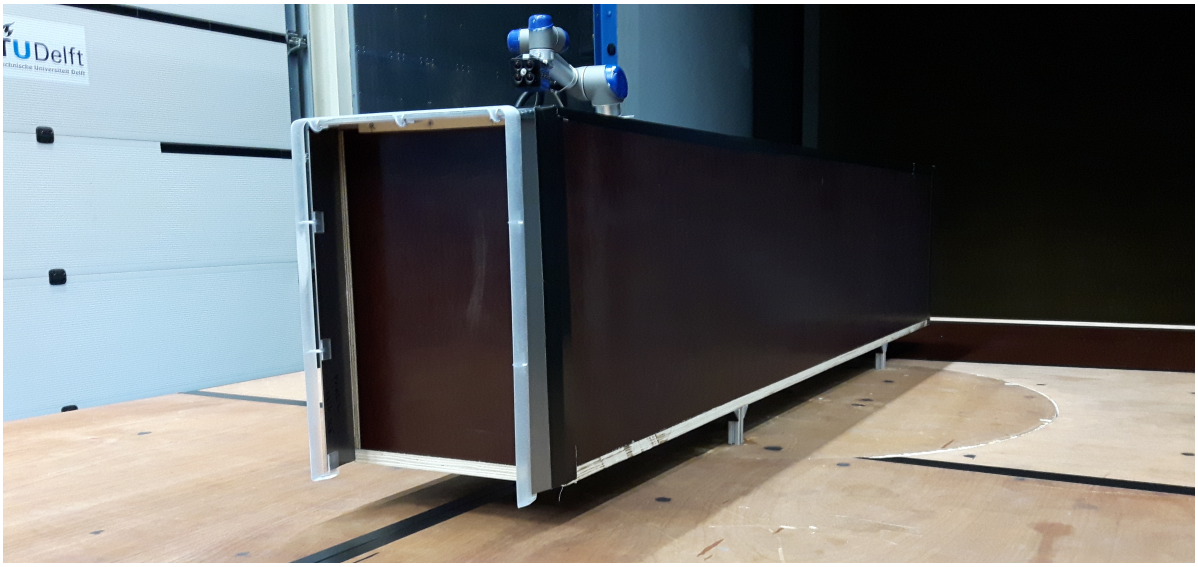

Figure 4.2: **1/8 scale GETS model with tail and guide vane standing in OJF facility**

4.1.1. GETS model

The GETS model is constructed out of 12mm thick wooden plates that are screwed together to form a box. A type of plywood with a water-resistant epoxy coating called 'betonplex' is used to give the model a smooth finish. The rounded nose of the model is milled out of foam and bolted to the front of the wooden box. It is possible to mount noses with a different radii to the model, but in this experiment only the nose with 68mm radius was used. The small gap between the foam nose and the wooden box is taped to smoothen any misalignment, also the other edges of the model are taped to improve the smoothness of the model. The required ride height of the model is provided by four aluminium profiles of 20x20mm cross-section that are placed in brackets and screwed to the bottom of the wooden box. The bottom of the legs feature a screw thread so the model can be bolted to the turning disk.

4.1.2. Tail

The tails are constructed out of 1,5 mm steel plate, from which they are cut and bent into the required shape. Even though all tails have the same shape, six tails are constructed so each guide vane can be mounted to a separate tail. This way the entire tail assembly can be interchanged, making configuration changes much faster so the limited time in the wind tunnel can be used efficiently. A small piece of wood is screwed to the top edge of the model base for the tail to rest on when they are taped to the model. With every configuration change, care was taken to ensure that the alignment between the model and all three sides of the tail was good.

4.1.3. Guide vanes

Out of all the guide vane configurations that were simulated only a select number could be produced to be tested in the wind tunnel because of time and cost constraints. Five guide vane designs were selected and the properties of each configuration are given in table 4.1. Some parameters were kept constant, such as the chord length (25 mm) and the horizontal position of the leading edge.

The guide vanes were 3D-printed using a stereolithography procedure at the Belgium based company Materialise. In stereolithography, the model is produced layerwise by selectively applying a laser to a UV-sensitive liquid resin. After the liquid resin has hardened, the model is lifted out of the resin to form the next layer until the complete model is 'pulled' out of the resin. This technique was selected because it results in a strong, high-quality model with a smooth finish. The guide vane in the initial simulations only consisted of the airfoil profile and was just 'floating in space'. So for the wind tunnel models of

Table 4.1: **Properties of guide vane wind tunnel models**

#	NACA profile	$\alpha[^\circ]$	$h_{gap}[mm]$
1	2412	6	6.25
2	2412	8	6.25
3	2412	12	6.25
4	2412	8	12.5
5	6415	6	6.25

the vanes to be produced, supporting legs and mounting points needed to be designed. First it had to be determined how many supports were required to make the tail-vane assembly strong enough to withstand the forces that occur during the experiement. The mid-span deflection of the vane under the lift and drag forces was estimated using standard beam deflection formulae. Taking one support at each corner as a minimum, the number of additional supports midway of the top and side vanes was varied. The resulting maximum deflections and bending stresses are shown in table 4.2. The trailing edge was found to be the location where the maximum bending stresses occur. It can be seen that for all cases the maximum bending stess is well below the maxium flexural strength, which is 64.1-74.2 MPa according to Materialise. [38] It was also clear that additional supports were required to keep the bending deflection acceptable. In the end it was decided to give all wind tunnel models two additional supports on each side vane and one on the top vane, which should yield a maximum deflection of around 0.1 mm. To minimise the effect of the support legs on the aerodynamics of the guide vane they were given an elliptical profile. At the end of each support leg is a rectangular mounting plate where the guide vane is attached to the inside of the tail using double sided tape. Fig. 4.3 shows a close-up of the streamlined support legs and the mounting plates on two guide vanes. The support on the bottom of the side vane acts as an end plate, but due to the high aspect ratio of the vane it is not expected to yield a reduction in induced drag.

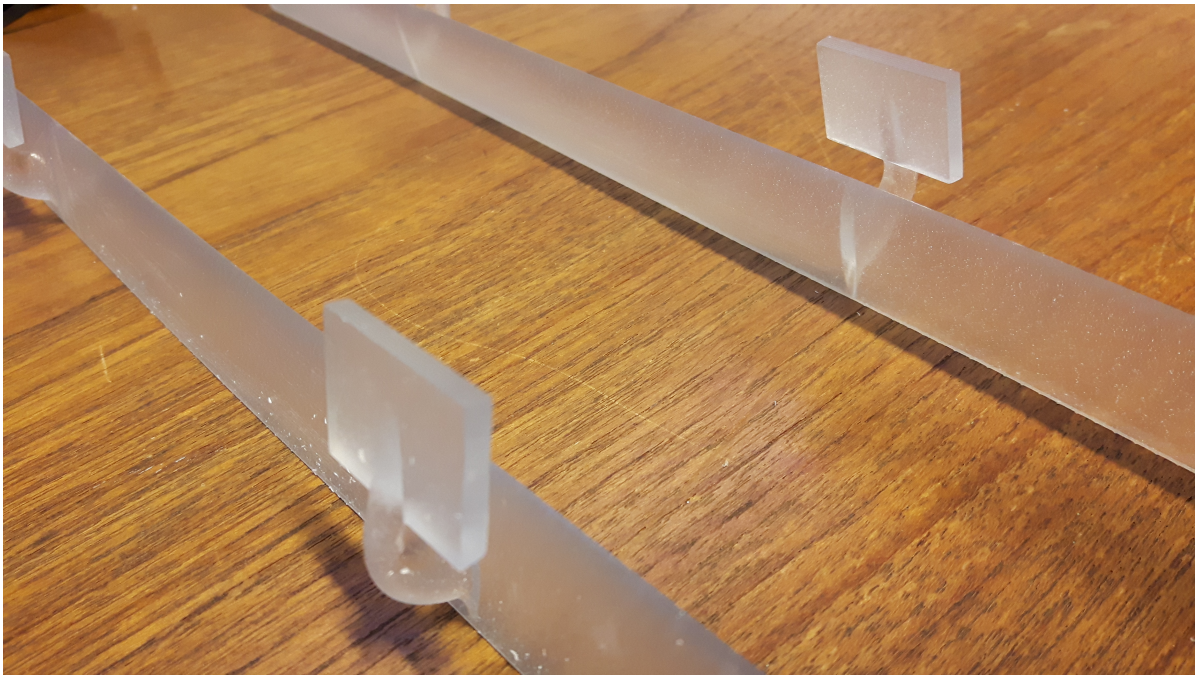

Figure 4.3: **Close-up of the support legs and mounting plates on two 3D-printed guide vanes**

Table 4.2: **Maximum deflection and bending stresses of 3D printed guide vane**

	Top vane		Side vane		
Nr of mid supports	0	1	0	1	2
Unsupported length [mm]	274	137	437	218	146
Deflection [mm]	1.4	0.1	8.6	0.5	0.1
Bending stress [Mpa]	-7.7	-1.9	-19.5	-4.9	-2.2

4.1.4. Ground board

Around the model and turning disk a ground board is constructed to emulate a road underneath the model in the jet stream of the OJF. Part of the ground board construction, as well as the turning disk itself were re-used from previous wind tunnel experiments conducted by Mulkens [42] and Kruijssen [34]. The total ground board was 4.5m long and 2.4m wide and was built onto the pneumatic movable table in the OJF. The challenge in constructing the ground board was to build a stable construction that fitted tightly around the turning disk, without touching it. During the wind tunnel campaign it occurred a number of times that the turning disk would touch the surrounding ground board and lead to erroneous balance measurements. Each time this was noticed immediately so the balance could be freed before proceeding with the next measurement.

4.2. Measurement techniques

4.2.1. Qualitative flow assessment

After building the experimental set-up, a visual inspection under operating conditions was performed to check the set-up for vibrations or installation errors. Next some critical areas were inspected for unwanted flow separation. The front edge of the ground board was inspected for the presence of a separation bubble using a woollen tuft and a microphone and was adjusted to have stable attached flow over the entire length of the ground board. Also the rounded front edges of the GETS model were inspected for separation at various flow velocities. A test velocity of 15 m/s was selected for the wind tunnel experiment, which will further explained in subsection 5.1.2.

4.2.2. Balance measurements

The measurements are performed using the 6-component external balance that was developed for the OJF by the NLR. The maximum error of each component was determined by Alons [2] in a calibration experiment and are given in table 4.3. During the design of the wind tunnel model it was determined that the maximum simultaneous loads in table 4.3 would not be exceeded despite the model and tails being relatively heavy. The balance was mounted on a rotation device such that the x-axis was aligned with the wind direction. The exact alignment of the set-up was performed with a laser alignment tool after the turning disk and model had been mounted on the balance. The balance measurements are acquired with a sampling rate of 2000 Hz and are averaged over a 60 s period to yield one measurement. This signal averaging is required because the unsteady data from the balance shows high frequency oscillations. Moreover the drag of a bluff body varies over time due to unsteady aerodynamic effects, which need to be averaged out. The model was rotated clockwise with 3 degree steps to simulate crosswind conditions. Unfortunately the rotation device was not able to achieve negative yaw angles. Apart from the six force and moment components, the atmospheric and dynamic pressure, temperature and wind speed are measured for each data point.

Table 4.3: **Errors and maximum simultaneous load of the OJF external balance. Source: NLR [2]**

Force			Moment		
	ϵ_{max} [%]	F_{max} [N]		ϵ_{max} [%]	F_{max} [Nm]
F_x	0.06	250	M_x	0.05	500
F_y	0.23	500	M_y	0.05	250
F_z	0.16	500	M_z	0.25	50

4.3. Post-processing

The data collected during the wind tunnel experiment needs to be post-processed before the results can be analysed. As explained in section 4.2 the measurements from the force balance are averaged over a 60 second period to account for fluctuations. Two corrections need to be applied to arrive at the non-dimensional force and moment components: accounting for the drag of the turning disk and wind tunnel blockage corrections.

4.3.1. Turning disk drag

The model and the turning disk are mounted onto the balance that measures the aerodynamic forces and moments. However, only the forces acting on the model are of interest, so the contribution of the turning disk needs to be subtracted. It is important to note that due to the layout of the OJF the balance itself is also partially subjected to the airflow, so the drag of the balance is also included in the turning disk drag. To minimize this contribution the balance is shielded from the airflow by means of a wooden plate that is mounted underneath the ground board. Before and after performing the measurements on the GETS model the aerodynamic forces are measured without the model in place. The drag force of the turning disk and the balance is non-dimensionalised and subtracted from the drag coefficient of each measurement.The drawback of this method is that interference effects between the model and the turning disk are not included, but there is no straighforward way to do that. The effect of the yaw angle on the drag of the turning disk was checked, but the effect turned out to be negligible.

4.3.2. Wind tunnel blockage corrections

In wind tunnel testing corrections should be made to account for the effect of the walls and the model on the air flow. More specifically the change of the flow velocity between the station where it is determined and the model should be accounted for. Classical wall and blockage corrections for closed section wind tunnels can not be used because the OJF is an open section tunnel and the blockage effects are generally of opposite sign. AGARDograph 109 describes the appropriate blockage corrections for tunnels with an open test section. [13] For these equations to be valid it is assumed that the ground board is level with the bottom of the OJF, while in reality it was raised slightly higher to be outside of the boundary layer of the tunnel wall. Two blockage corrections are applied: nozzle blockage ϵ_n that accounts for the velocity increase due to the model blocking the nozzle and solid blockage ϵ_s accounting for the increased flow angle due to the over expansion of the flow because it has to move around the model.

Nozzle Blockage

The nozzle blockage correction factor ϵ_n given in equation (4.1) is derived from the potential flow of placing a point source representative of the model in the nozzle flow. [13] The result is a semi-infinite body of revolution with a stagnation point that coincides with the front of the model at x_m.

$$\epsilon_n = \epsilon_{qn}\left(\frac{R_n^3}{(x_m^2 + R_n^2)^{3/2}}\right) \tag{4.1}$$

Where:

$$\epsilon_{qn} = \frac{\left(\frac{S}{2C}\right)\left(1 + \frac{x_s}{\sqrt{(x_s^2 + R_n^2)}}\right)}{1 - \left(\frac{S}{2C}\right)\left(1 + \frac{x_s}{\sqrt{(x_s^2 + R_n^2)}}\right)} \tag{4.2}$$

The distance between the nozzle and the point source x_s is negative and is given by equation (4.4). Whereas the hydraulic diameter of the nozzle R_n depends on the duplex nozzle area C:

$$R_n = \sqrt{\frac{C}{\pi}} \tag{4.3}$$

$$x_s = -x_m + \frac{L_m}{2} + \sqrt{\frac{S}{2\pi}} \tag{4.4}$$

Solid blockage

The second correction term ϵ_s accounts for the effect of solid blockage and is given by equation (4.5). Here it is assumed that the tunnel cross-section is square, while in reality the corners have a fillet to form an octagonal section. [13]

$$\epsilon_s = a\sqrt{\frac{V_m}{l_m}}\left(\frac{S}{\sqrt[3]{\frac{C}{1+\epsilon_{qn}}}}\right) \tag{4.5}$$

Where V_m is the volume of the model and the value of constant τ is set to -0.238 as recommended by AGARDograph 109 for sections with $w/h = 1$. [23]

Total blockage effect

The effects of the nozzle and solid blockage are combined into a single correction factor ϵ_t as shown in equation (4.6). The blockage correction is performed by multiplying each velocity measurement with $(1 + \epsilon_t)$. It follows that the corrected dynamic pressure is obtained by multiplying with $(1 + \epsilon_t)^2$

$$\epsilon_t = \epsilon_n + \epsilon_s = 0.0074 \tag{4.6}$$

4.3.3. Wind-averaged drag coefficient

The performance of a road vehicle over a range of crosswind conditions can be described using the wind-averaged drag coefficient $\bar{C}_T$, which is defined by SAE J1252 as: [12]

$$\bar{C}_T(V_T) = \frac{\bar{D}(V_T)}{1/2\rho {V_T}^2 S} \tag{4.7}$$

For a limited number of (n) yaw angles this can be approximated by:

$$\bar{C}_T(V_T) = \frac{1}{n\bar{M}} \sum_{j=1}^{n} M(j) C_T(j) \tag{4.8}$$

In this equation $M(j)$ is a factor that depends on the wind velocity V_W, the tangential velocity V_T and the j^{th} crosswind angle Φ according to equation (4.9). $C_T(j)$ is the drag coefficient in the vehicle axis

system measured at the j^{th} crosswind angle.

$$M(j) = 1 + \left(\frac{V_W}{V_T}\right)^2 + 2\left(\frac{V_W}{V_T}\right)\cos\Phi(j) \tag{4.9}$$

$$\Phi(j) = \left(\frac{180j}{n}\right) - \frac{90}{n} \tag{4.10}$$

$$\Psi(j) = \tan^{-1}\left(\frac{\frac{V_W}{V_T}\sin\Phi(j)}{1 + \frac{V_W}{V_T}\cos\Phi(j)}\right) \tag{4.11}$$

The procedure for calculating the wind averaged drag coefficient in the context of this thesis is somewhat different than for a road test where there is a constant vehicle velocity V_T. For the numerical simulations as well as the wind tunnel experiment the model is yawed by an angle $\Psi = 0, 3, 6°$ with respect to the airflow. This means that with regard to figure 4.4, velocity V is constant. The value of Φ follows from equation (4.10), after which the values of corresponding V_T and V_W can be determined using equation (4.11) and trigonometric rules.

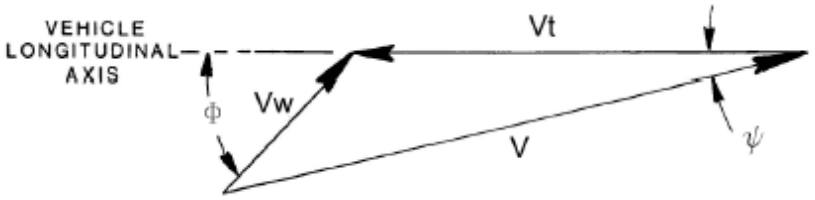

Figure 4.4: **Relative airspeed vector diagram. Source: SAE J1252 [12]**

5

Experimental results

In this chapter the results from the experimental campaign will be presented. These experimental results consist of the forces and moments that have been collected using the external balance. All forces and moments have been normalised using the the frontal area of the wind tunnel model and the corrected freestream flow velocity. Details of the experimental set-up can be found in chapter 4. First the results of the set-up validation are presented in section 5.1. Next the experimental results are presented in section 5.2.

5.1. Set-up validation

A few steps were taking before starting the actual measurements to validate the wind tunnel set-up. First it was ensured that the selected operating point was representative by performing a Reynolds sweep. Also the uncertainty of the experimental setup was determined, which is described in subsection 5.1.3.

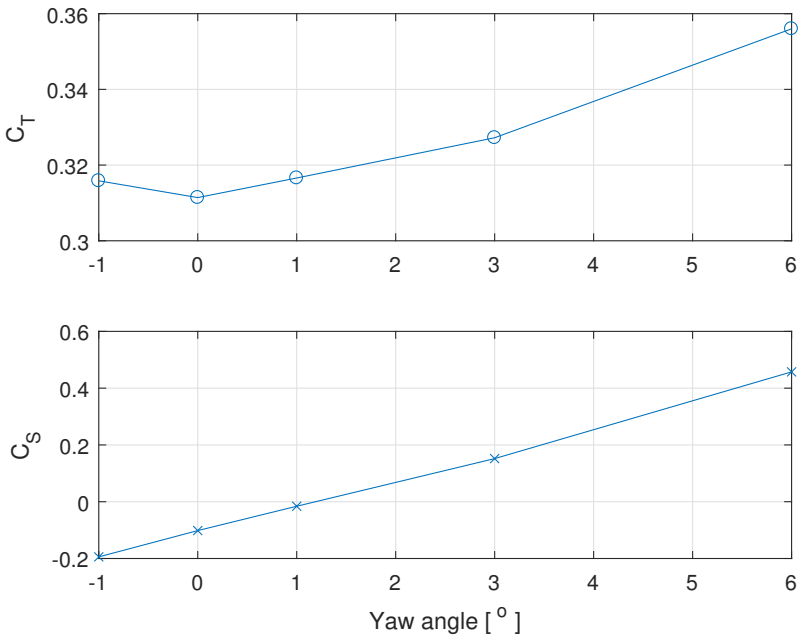

Figure 5.1: **Experimental drag and side force coefficient of the 1/8 scale GETS model with zigzag tape,** $V = 15m/s$**,** $Re = 3.8 \cdot 10^5$

5.1.1. Model Alignment

While building the wind tunnel set-up it was required to pay close attention to the alignment of the model. Placing the pneumatic table, building the ground board and installing the model was all done by hand, so it was easy to introduce misalignments. After building the wind tunnel set-up a laser alignment tool was used to align both the ground board and the model with the centreline of the OJF. After that the tunnel was started to determine the aerodynamic alignment of the model by measuring the drag and side force over a range of yaw angles. As was mentioned in subsection 4.2.2 it was not possible to achieve negative yaw angles with the rotating device that was used. However, while aligning the model using the laser tool, the disk had to be rotated a small (positive) amount to be in line with the tunnel. This made it possible to include a negative yaw angle of $-1°$, which led to the yaw angle range of $\Psi = -1, 0, 1, 3, 6°$.

It can be seen in figure 5.1 that the drag coefficient is at a minimum for $\Psi = 0°$. This indicates that the model is indeed aligned geometrically as well as aerodynamically. The behaviour of C_S with yaw angle looks like what would be expected from the simulations in subsection 3.3.6. But it is peculiar that the side force coefficient is not zero at $\Psi = 0°$. Looking at the bottom plot in figure 5.1 would indicate that the model is aligned at a yaw angle of $\Psi = -1°$. It is also possible that multiple factors are at play and for example the model is slightly asymmetric as well as misaligned. The wind tunnel model was constructed by hand, so it can be imagined that the nose is not exactly centered or the center of gravity is not at the vehicle centreline. The offset in C_S is also observed for other tested configurations, so it is also possible that there is an offset in the balance measurements of the side force. However, this is unlikely as the balance was 'biased' before starting each measurement while the tunnel was still off. In the worst case there was a $-1°$ misalignment in the wind tunnel set-up. Given that the drag coefficient is the main parameter of interest in this research, it was decided to keep the alignment of figure 5.1 as C_T showed a clear minimum for $\Psi = 0°$.

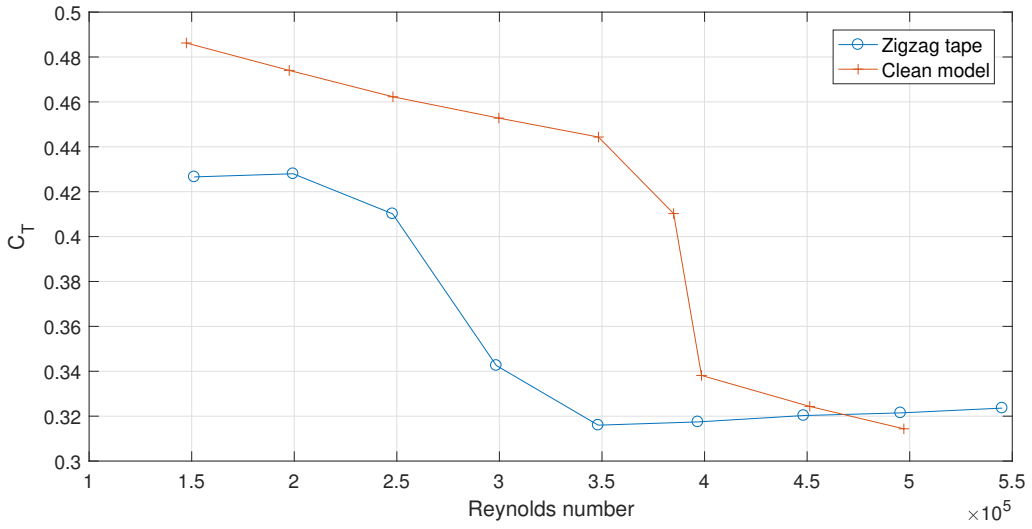

Figure 5.2: **Influence of the Reynolds number on the drag of the 1/8 GETS model with and without zigzag tape**

5.1.2. Reynolds sweep

Before starting the measurements of the tail and guide vane configurations, the effect of the Reynolds number on the drag of the GETS model is investigated by stepwise increasing the tunnel velocity in a Reynolds sweep. Initially the front of the GETS model was clean and the investigation with the microphone indicated that a separation bubble was present over the curved part of the nose at lower flow velocities. Fig. 5.2 shows the behaviour of the drag coefficient throughout the Reynolds sweep

with and without zigzag tape. Normally the OJF can run up to 27 m/s, but as the wind tunnel time was shared with another master thesis research, a PIV test setup was installed in the tunnel. This meant that, among others, the computers for PIV data acquisition and controls of the PIV equipment were standing in the tunnel room, which practically limited the testing velocity to $15m/s$. Using the square root of the cross sectional area of the model as a reference, this yields a Reynolds number of $3.8 \cdot 10^5$. It can be seen in figure 5.2 that without zigzag tape, this Reynolds number corresponds with the region of the 'drag crisis'. Testing at this velocity would make the results unpredictable and not representative of a fullscale model. Therefore two layers of zigzag tape were applied on the stagnation surface, approximately 1cm before the start of the rounded edge to force the flow transition and stay attached over the curved surface. With the zigzag tape applied the drop in drag coefficient occurs at a lower Reynolds number, making it possible to conduct the test at 15 m/s. This is also the case when the model is placed at a yaw angle, which can be seen in figure 5.3.

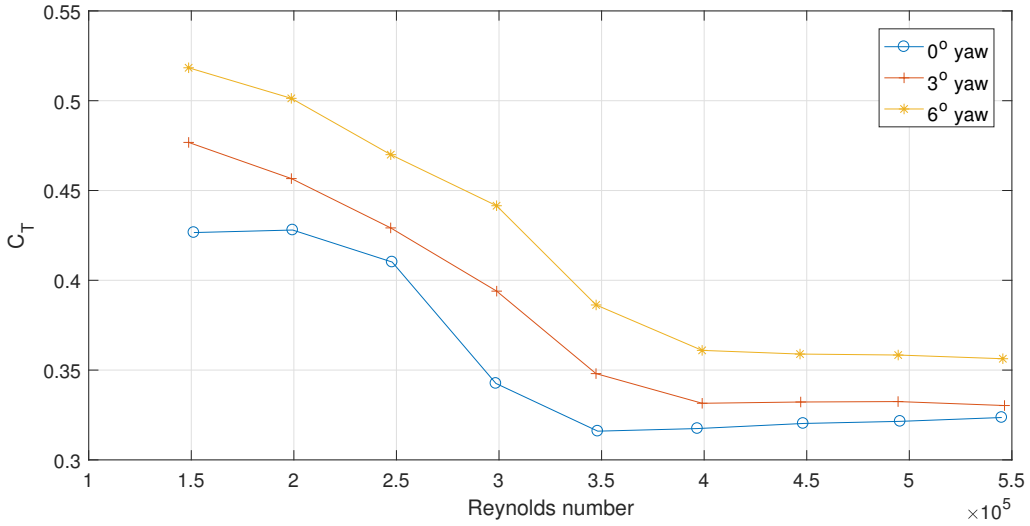

Figure 5.3: **Influence of the Reynolds number on the drag of the 1/8 GETS model with zigzag tape at various yaw angles**

5.1.3. Drag uncertainty

Over the span of multiple days the single GETS model without drag reduction devices was tested to determine the drag uncertainty of the experimental setup. As can be seen in table 5.1 there is some variance between the six measurements of the same model, which leads to a standard deviation of 7 drag counts. This is approximately 2% of the total drag of the GETS model. The difference between this drag uncertainty and the value given in table 4.3 can be caused by a number of factors such as handling the model between configuration changes, accuracy of the rotation device and vibrations in the experimental setup.

Table 5.1: **Experimental drag uncertainty of the 1/8-scale GETS model without drag reduction devices,** $V = 15m/s$**,** $Re = 3.8 \cdot 10^5$

Run	1	2	3	4	5	6	Mean	σ
C_T	0.3234	0.3114	0.3199	0.3230	0.3300	0.3296	0.3229	0.0069

5.2. Experimental results

In this section the results from the wind tunnel experiment will be presented. All figures showing drag coefficient results are fitted with error bars that represent 1 standard deviation of the measurement uncertainty as was determined in subsection 5.1.3. This corresponds to the 68% confidence interval

of the results. An overview of all C_T measurements of the various configurations is given in table 5.2. A short description of each configuration is included in the table, the design parameters of the five 3D-printed guide vanes can be found in more detail in table 4.1 of the previous chapter.

Table 5.2: **Overview of measured C_T values of the 1/8 scale wind tunnel models at various yaw angles and calculated wind-averaged drag coefficient, $V = 15m/s$, $Re = 3.8 \cdot 10^5$**

	$0°$	$3°$	$6°$	$\bar{C}_T$	Description
GETS	0.323	0.327	0.356	0.337	Single GETS
Baseline	0.277	0.291	0.305	0.292	GETS + tail
Print1	0.272	0.288	0.306	0.290	NACA2412, $6°$
Print2	0.275	0.288	0.302	0.290	NACA2412, $8°$
Print3	0.283	0.296	0.308	0.297	NACA2412, $12°$
Print4	0.275	0.290	0.305	0.293	Print2 with larger gap
Print5	0.277	0.295	0.309	0.295	NACA6415, $6°$

5.2.1. Effect of tail

The effect of adding a tail to the GETS model on the drag coefficient is presented in figure 5.4. Note that for the value of C_T for the single GETS model at $\Psi = 0°$ the mean of the measurements presented in table 5.1 has been used. This is why the value is different from the value in figure 5.1 that was used for aligning the model. It can be seen in figure 5.4 that the tail of the baseline model offers a significant drag reduction with respect to the GETS model for all yaw angles. The effect is largest at $\Psi = 6°$, where the tail reduces the drag with 51 drag counts. As can be seen in table 5.2 the wind averaged drag reduction is 45 drag counts. The drag of the baseline model increases linearly with yaw angle. The curve of the GETS model shows some different behaviour, but the error bars in figure 5.4 suggest that these differences might also be caused by the measurement uncertainty. What is clear, however, is that the drag reduction caused by the tail is well outside the bounds of uncertainty and can therefore be regarded significant.

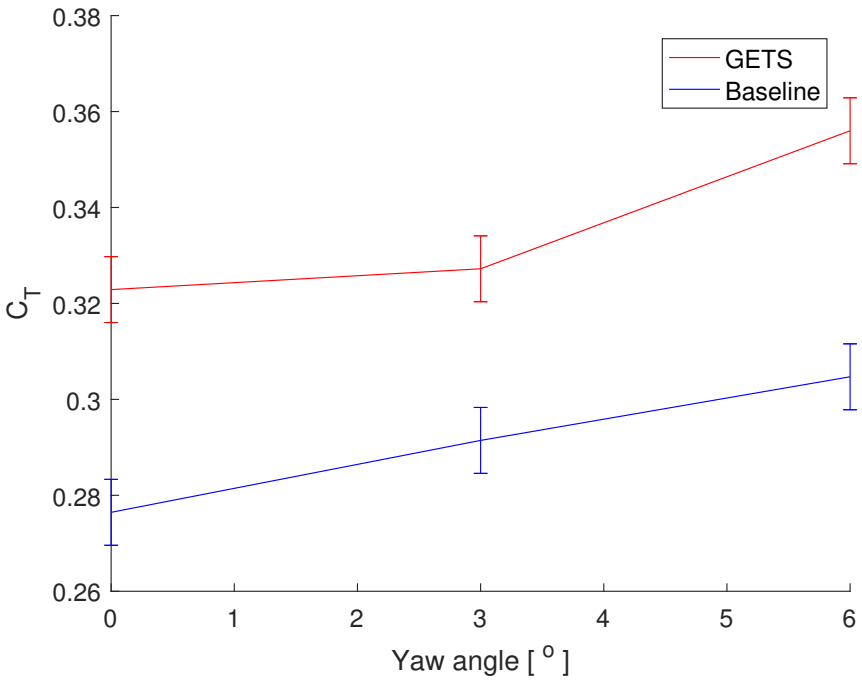

Figure 5.4: **C_T of the GETS and the baseline model at various yaw angles, $V = 15m/s$, $Re = 3.8 \cdot 10^5$**

5.2.2. Effect of guide vanes

The effects of adding a guide vane to the trailing edge of a tail was tested in the wind tunnel for five designs. In the wind tunnel there is no straightforward way to determine the drag contributions of different parts of the model, so only the effect of the guide vanes on the total drag coefficient can be measured. As the guide vanes aim to improve the performance of the tail behind the GETS model, the drag reductions are measured relative to the C_T of the baseline model at the corresponding yaw angle. The same logic is applied to the wind-averaged drag reduction of the guide vanes. The drag reductions of the five guide vanes configurations for each yaw angle and the wind-averaged reduction are presented in figure 5.5.

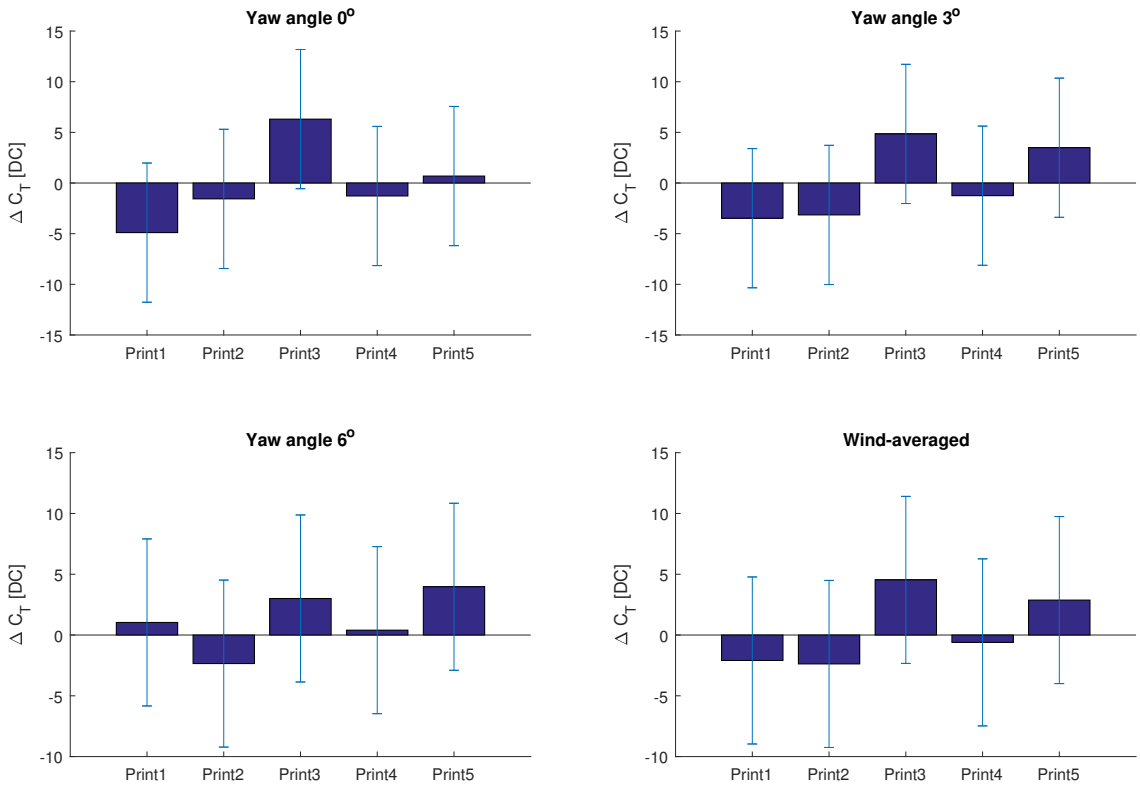

Figure 5.5: **Drag reduction of the five guide vanes with respect to the baseline model per yaw angle,** $V = 15m/s$, $Re = 3.8 \cdot 10^5$

A few things stand out when looking at figure 5.5. First of all it can be seen that for all configurations the error bars are larger than any drag reductions or additions that are found. This makes it difficult to make any definitive statement about these results. Still an attempt will be made to identify trends in the results. Starting with guide vane labelled 'Print1', which has a NACA2412 profile, an incidence angle of $6°$ and a gap height of $0.1L_t$. The guide vane provides the largest measured drag reduction of all configurations at $\Psi = 0°$, but this drag reduction reduces with yaw angle to finally become a drag increase for $\Psi = 6°$. This is peculiar because in the numerical simulations the additional drag reduction of a guide vane on a tail was found not to change with yaw angle. The wind-averaged drag reduction of this guide vane is 2.4 drag counts reduction relative to the baseline model. This result is only surpassed by 'Print2', which has the same airfoil profile and gap height, but an incidence angle of $8°$. 'Print2' is the design that based on the numerical simulations would be expected to yield the best results, which it does in terms of $\bar{C}_T$. Besides it is the only guide vane that yields a drag reduction for all

yaw angles. Guide vane number 3 also has the same profile and gap height, but an incidence angle of $12°$. Surprisingly this design increases the drag of the model by a fair amount for all yaw angles. Based on the simulations it was expected to perform less than the vanes with incidence angle $6°$ and $8°$, but not as poorly as the experimental results suggest. 'Print4' is the same as 'Print2', but has a gap height that is twice as large. It was suspected that the guide vane would perform less than the counterpart with a smaller gap height and the results seem to confirm this. This is interesting because in the wind tunnel experiment due to the lower Reynolds number and the zigzag tape on the front of the model the boundary layer can be assumed to be thick. But still in the experiment the guide vane with the lowest gap height was found to be the most efficient. The drag of the model equipped with this guide vane is approximately equal to the baseline model, providing a wind-averaged drag reduction of less than a drag count. Finally 'Print5' was the most effective guide vane with a NACA 6415 profile in the full-scale simulations. This guide vane has an incidence angle of $6°$, but a thicker and more cambered profile. From the simulations it was expected to perform less than the NACA 2412 profiles, but to provide a small drag reduction. The experimental results suggest that it only increases the drag of the GETS model, even though it is not the worst performing guide vane.

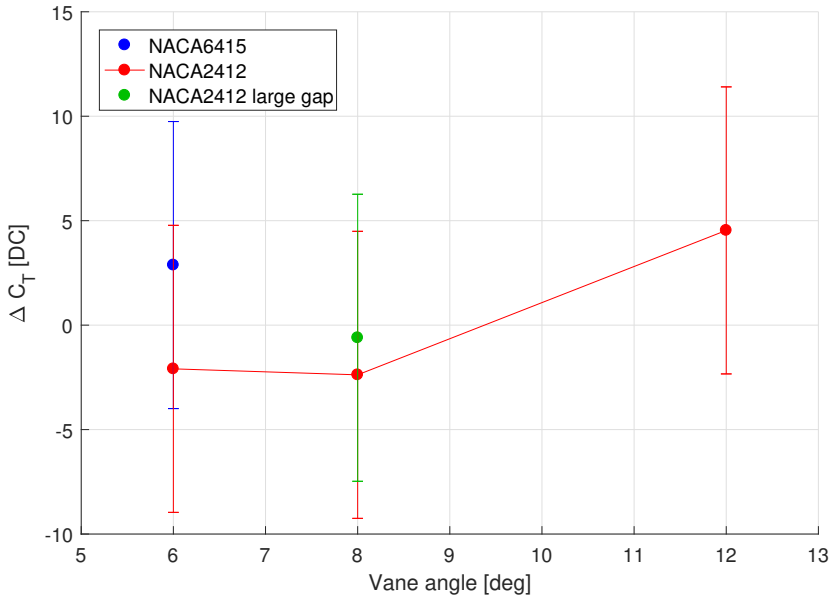

Figure 5.6: **Wind-averaged drag reduction of the five guide vanes with respect to the baseline model,** $V = 15m/s$, $Re = 3.8 \cdot 10^5$

In figure 5.6 the experimental wind-averaged drag reduction results are plotted versus the incidence angle of the guide vane. In this way the experimental results can be compared to figure 3.22 from the numerical results. Here it can be seen that the NACA 2412 guide vanes show a very similar behaviour with incidence, but due to the poor performance of the $12°$ guide vane the curve seems much steeper. The maximum drag reduction is found for $\alpha = 8°$, but one should be careful with such claims given the small differences and the large uncertainty of the results. For the yaw angle of $\Psi = 0°$ this particular curve would look different, but due to the large differences between yaw angles it seemed appropriate to average the results over the crosswind angles. The experimental and simulated drag reduction of each yaw angle will be compared in chapter 6. Looking at the guide vane with the NACA 6415 airfoil, in the full-scale simulations it provided a drag reduction of just over 1 drag count for this incidence angle. In the wind-tunnel experiment it seems to be performing less, but since it is the only data point for this airfoil it is difficult to make any statement about the possible cause. The larger gap height seems to reduce the performance of the guide vane. This could be caused by a larger vane drag contribution, as

was found in the numerical simulations. However, one should also not forget that the guide vanes in the wind tunnel model featured support legs that produce a small amount of drag themselves. These legs were streamlined to reduce their impact on the flow. In any case these support legs were larger to accommodate the larger gap height of this particular guide vane, which also increases the drag of the legs.

6

Discussion of results

In this chapter the results of the numerical simulations and the experimental campaign will be further discussed. First the methodology will be validated by comparing the experimental results to a new set of numerical simulations that match the conditions in the wind tunnel in section 6.1. Next a reflection on the concept of combining a tail and a guide vane will be given to better understand the observed behaviour, which can be found in section 6.2.

6.1. Validation

In this section the results from the numerical simulations will be compared to the experimental results. As mentioned before the main purpose of the wind tunnel experiment was to serve as a validation tool for the CFD simulations. Given the small amount of different configurations that could be tested in the wind tunnel, the experimental results are better suited as reference than to make deductions from.

6.1.1. Changes to numerical simulations

To make the comparison between the simulations and the experiment valid, the conditions should also be the same. For that purpose a new set of numerical simulations, the 'Validation runs', have been performed. The main differences between these simulations and the work presented in chapter 3 are the following:

- Velocity is reduced to 15 m/s to match the tunnel speed
- Turbulence intensity is set to 0.3% to match the tunnel value [6]
- The small metal legs of the GETS model have been modelled
- Support legs of the guide vanes have been partially modelled
- The ground board on the bottom of the domain is modelled as a stationary wall with the same size as the ground structure in the wind tunnel

As a result, the Reynolds number of the validation simulations matches that of the wind tunnel experiment at $Re = 3.8 \cdot 10^5$, based on the square root of the frontal area. The reason for only partially modelling the support legs of the guide vane is that otherwise the meshing software would run into trouble. When the mounting plate was also modelled this led to tight corners near the interface of the tail and the guide vane that the meshing software could not deal with. Therefore it was decided to only keep the parts of the support legs that were exposed to the airflow from the tail. The mounting plate that was omitted is located in the wake region and is expected to have little influence on the drag. The

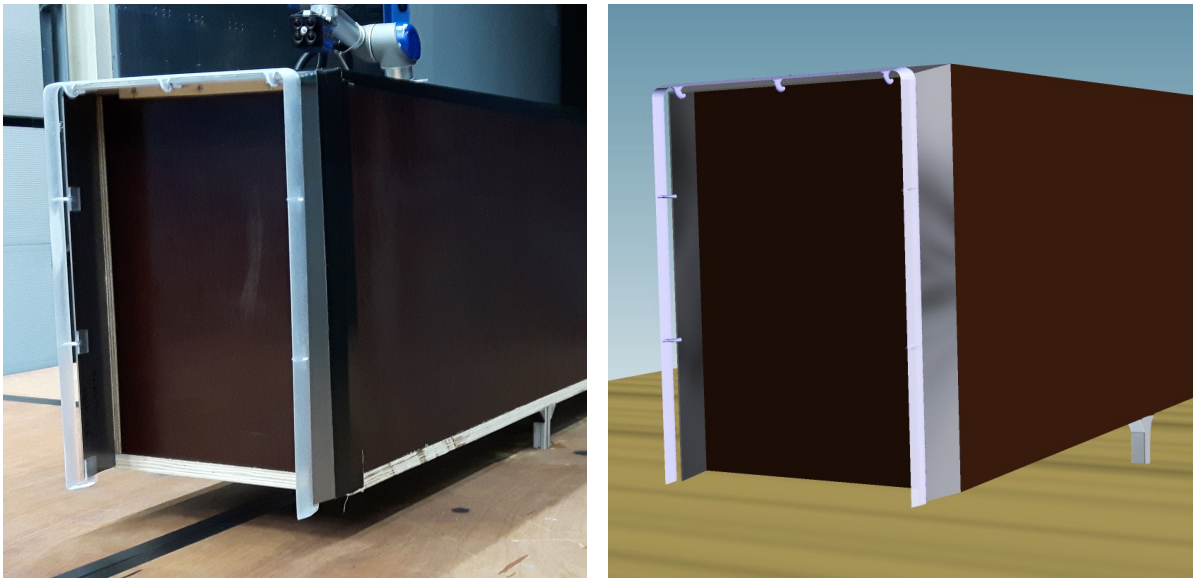

(a) Wind tunnel model (b) Validation simulation

Figure 6.1: **Comparison of the wind tunnel model and the validation simulation**

shape of the metal legs of the GETS model has been simplified to accommodate meshing. In the wind tunnel the ground structure consisted of a separate rotating disk and the rest of the ground board, but in the simulations these are modelled as one. A side by side comparison of the model in the wind tunnel and in the validation simulation is shown in figure 6.1. Here the partially modelled vane support legs and simplified model supports can be seen.

6.1.2. Comparison between the numerical and experimental results

An overview of all the measured and simulated drag coefficients of the seven wind tunnel configurations (GETS, baseline and 5 guide vanes) is given in table 6.1. The difference between the experimental and simulated values is reported in drag counts.

Table 6.1: **Comparison of experimental results and validation simulations. 1/8-scale,** $V = 15m/s$**,** $Re = 3.8 \cdot 10^5$

Ψ		GETS	Baseline	Print1	Print2	Print3	Print4	Print5
0°	$C_{T,exp}$	0,3229	0,2765	0,2716	0,2749	0,2828	0,2752	0,2771
	$C_{T,sim}$	0,3390	0,2833	0,2825	0,2819	0,2827	0,2832	0,2834
	$\Delta C_T[DC]$	16,1	6,8	10,9	7	-0,1	8	6,3
3°	$C_{T,exp}$	0,3272	0,2914	0,2880	0,2883	0,2963	0,2949	0,2949
	$C_{T,sim}$	0,3496	0,2913	0,2906	0,2898	0,2903	0,2911	0,2914
	$\Delta C_T[DC]$	22,4	-0,1	2,6	1,5	-6	-3,8	-3,5
6°	$C_{T,exp}$	0,3560	0,3047	0,3057	0,3024	0,3077	0,3051	0,3087
	$C_{T,sim}$	0,3654	0,2992	0,2998	0,2983	0,2980	0,3	0,3
	$\Delta C_T[DC]$	9,4	-5,5	-5,9	-4,1	-9,7	-5,1	-8,7
Wind-averaged	$\bar{C}_{T,exp}$	0,3374	0,2924	0,2903	0,2901	0,2970	0,2933	0,2953
	$\bar{C}_{T,sim}$	0,3528	0,2921	0,2919	0,2909	0,2912	0,2924	0,2925
	$\Delta \bar{C}_T[DC]$	15,4	-0,3	1,6	0,9	-5,8	-0,9	-2,8

Uncertainty

When looking at the differences in table 6.1 in general, it can be seen that C_T is both over- and under-predicted by CFD. There is no structural difference between the experimental and numerical results. The average relative difference between the experimental and numerical drag coefficient is equal to

2.3%. In absolute this is 6.8 drag counts, which is approximately equal to the drag uncertainty in the wind tunnel.

Note that this does not mean that the difference between the numerical and experimental results is only caused by the measurement uncertainty in the wind tunnel. Earlier in subsection 2.3.2, the uncertainty in the numerical simulations in terms of the error due to discretisation was discussed. The numerical uncertainty related to the grid convergence, GCI, was found to be 4.3%. Based on the C_T of the baseline model found in the validation simulation of 0.2833, this translates to an uncertainty of 12 drag counts, or almost twice the experimental uncertainty. The difficulty in interpreting those uncertainties is that they appear so different in nature. The experimental uncertainty is seemingly random, giving different drag values when measuring the same configuration at a different time. Where the numerical simulation will converge to the same drag coefficient every time, but the mesh sensitivity study indicates that the drag will decay asymptotically as the grid is refined. The most important thing to keep in mind is that both these uncertainties exist and as a result, the conclusions must be drawn accordingly. For example, based on the uncertainty of the methodology and the drag reductions found in this thesis, it could be concluded that the tail achieves a significant drag reduction with respect to the GETS model, whereas the reduction of the guide vane relative to the baseline model is not significant.

In a certain sense, the uncertainty of the numerical simulations was deliberately chosen in a trade-off between accuracy and computational time. The used refinement allowed a large number of different designs to be analysed and the accuracy is apparently not much lower than the accuracy of the wind tunnel experiment. Therefore this calls for a critical review of the wind tunnel set-up, as it does not provide the high accuracy required to prove the small drag reductions provided by the guide vane. In order to prove aerodynamic improvements in the order of percentages, one would desire a higher accuracy from the experimental set-up.

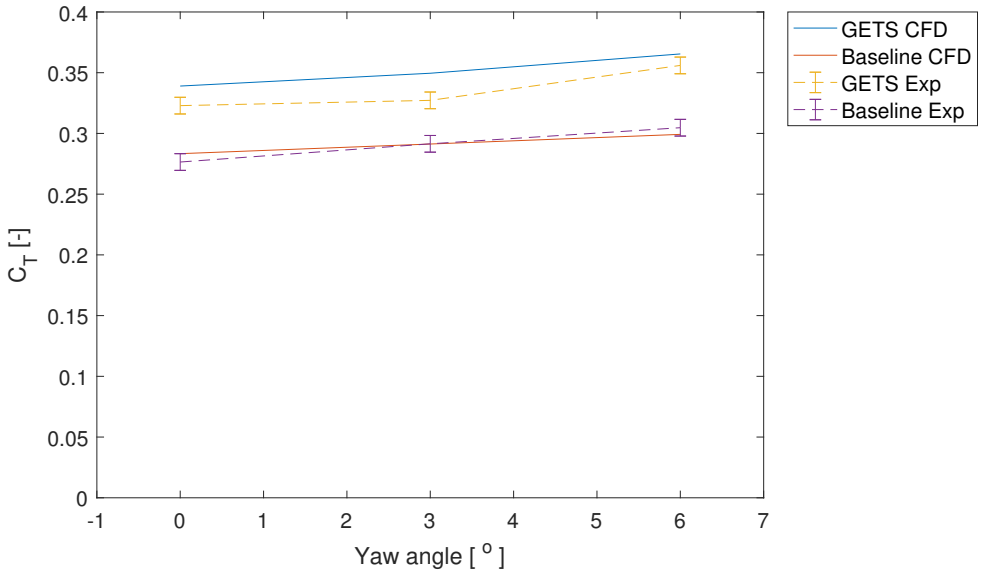

Figure 6.2: **Simulated and experimental C_T value of the GETS and the baseline model at various yaw angles. 1/8-scale, $V = 15m/s$, $Re = 3.8 \cdot 10^5$**

GETS and baseline model

Looking at table 6.1, what stands out is that the largest differences are found for the GETS model, where the C_T is over-predicted by the simulations for all yaw angles. This is peculiar because the differences are much larger than for the GETS model fitted with a tail. Fig. 6.2 shows the numerical

and experimental drag coefficient of the GETS and the baseline model versus yaw angle. Here it can be seen that the drag of baseline model is very well predicted by the simulations, while the CFD simulation overestimates the drag of the GETS model. Possibly the difference is caused by the Reynolds decomposition that is introduced by the RANS equations. In the RANS simulations an average solution is calculated by decomposing the flow variables in a mean and a time-varying component. The measured wind tunnel value is an average of a set of instantaneous measurements. So it is possible that there is an unsteady flow phenomenon like 'bubble pumping' [17] that is not captured by the RANS simulations that is causing the difference. It is known that the tail stabilises the wake of the HDV by capturing the vortices between the tail panels, so this might explain why the difference between the experimental and simulated drag coefficient is smaller for the GETS model with a tail.

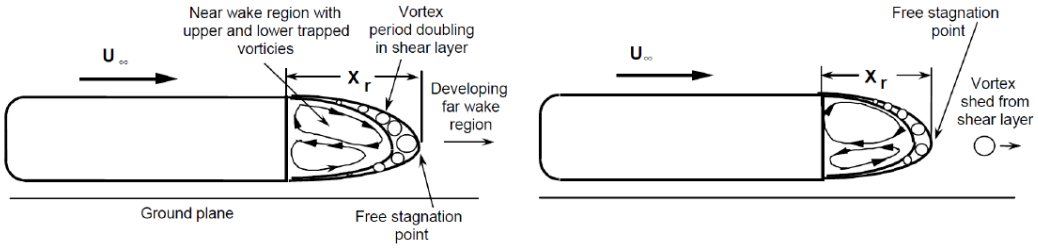

Figure 6.3: **Unsteady wake behind an HDV as seen from the symmetry plane with bubble pumping phenomenon. Source: Duell & George [17]**

Effect of yaw angle

When looking at the difference between the numerical and experimental C_T values of the other tested configurations in table 6.1 and taking notice of the change with yaw angle, something else stands out. For $\Psi = 0°$ and $3°$ the differences between the numerical and experimental results is both positive and negative. But for $\Psi = 6°$ the numerical simulations predict a too low C_T for the baseline model and all guide vanes. This behaviour is more clearly visible in figures 6.4 to 6.6 where the numerical and experimental results are plotted side by side. It seems that the numerical simulations are not able to accurately predict the increase in drag coefficient when the model is yawed. Considering that the simulations generally predict a too high C_T for $\Psi = 0°$ and a too low value for $\Psi = 6°$, the increase in drag with yaw angle predicted by the simulations is very low compared to the experimental results. This might indicate that the mesh that was used to simulate all conditions is not valid for the largest yaw angle. With regard to future work, it is recommended to investigate whether the simulation results of $\Psi = 6°$ better correspond with the experimental results if the refinement box is extended on the leeward side of the model.

Guide vanes

When focussing on the curves of the NACA 2412 profiles in figures 6.4 to 6.6 the influence of the vane incidence angle and yaw angle can be investigated. The obvious discrepancy between the numerical and experimental results is found for the vane angle of $12°$, which slightly reduces the drag of the baseline model in the simulations, but does the opposite in the experiment. The NACA 2412 profile with $\alpha = 6°$ yields a large drag reduction for $\Psi = 0°$, which is lower for $\Psi = 3°$ and becomes a drag increase for the largest yaw angle. Interestingly a similar behaviour is predicted by the numerical simulations, though the differences are much smaller. When looking at the numerical results of the guide vane with $\alpha = 12°$ for the different yaw angles, it can be seen that the drag reduction relative to the baseline model increases with yaw angle, though the differences are very small. A look in the drag contributions reveals that the guide vane with $\alpha = 6°$ hardly causes a base drag reduction when the model is yawed, which is caused by the leeward side of the guide vane losing effectiveness. Before it was stated in subsection 3.3.6 that the drag reduction that the guide vane provides with respect to the baseline model does not change with yaw angle. These findings imply, however, that this is only true

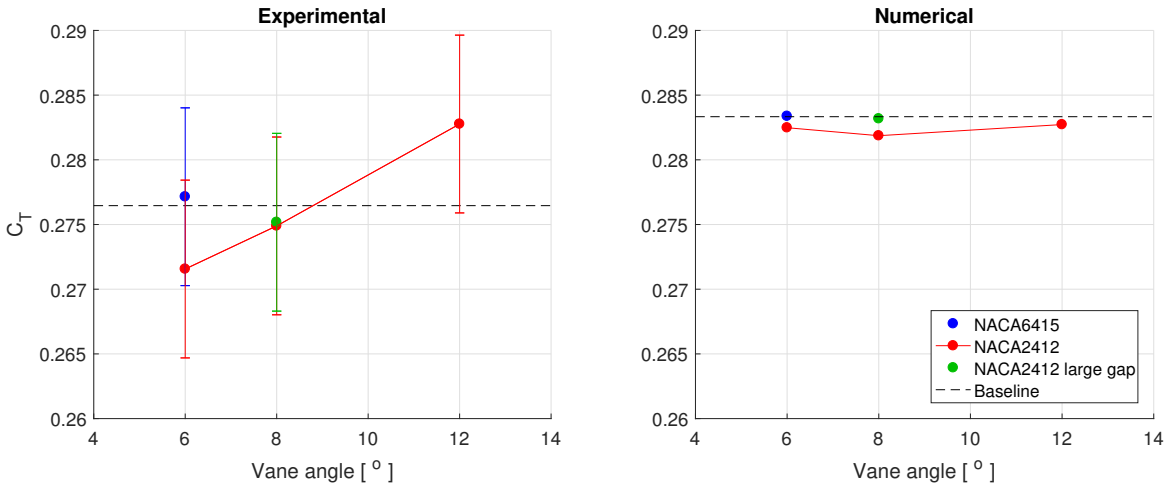

Figure 6.4: **Simulated and experimental C_T value of the baseline model and guide vane configurations at $\Psi = 0°$**

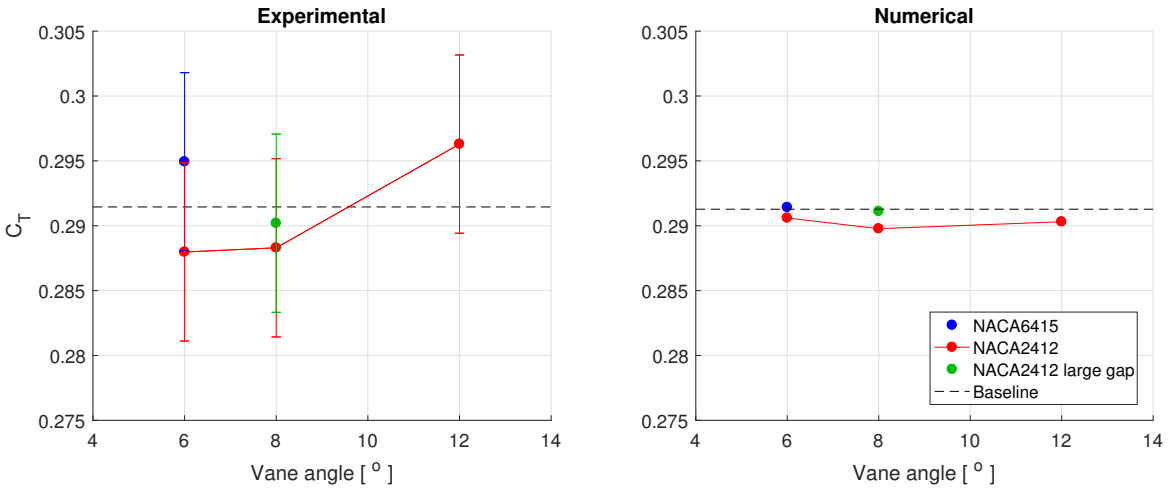

Figure 6.5: **Simulated and experimental C_T value of the baseline model and guide vane configurations at $\Psi = 3°$**

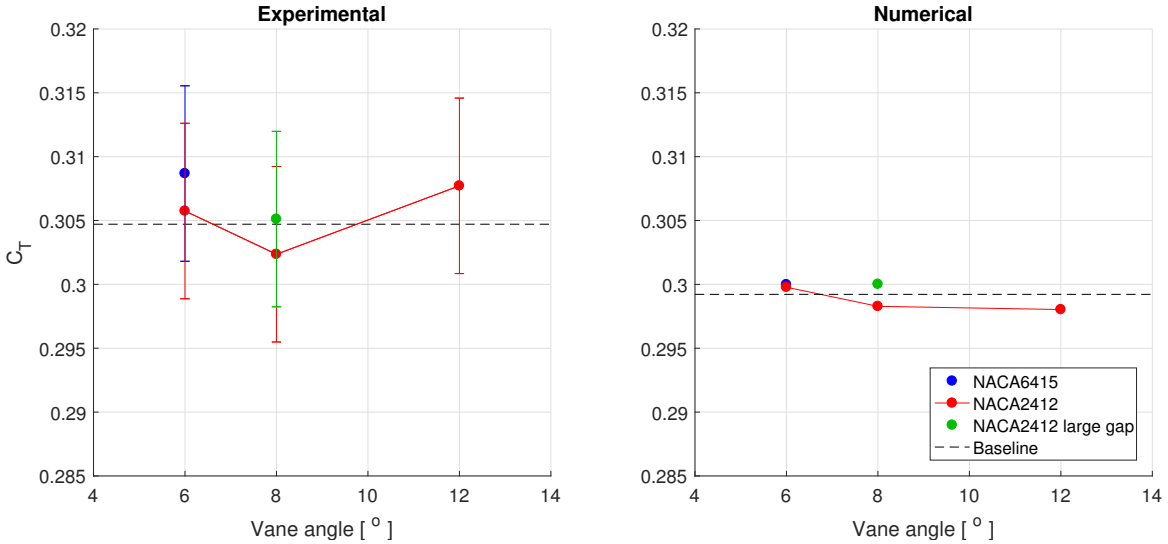

Figure 6.6: **Simulated and experimental C_T value of the baseline model and guide vane configurations at $\Psi = 6°$**

for the guide vane with the 'optimal' incidence angle of $\alpha = 8°$ that was simulated in subsection 3.3.6. For a smaller incidence angle the drag reduction reduces with yaw angle due to the leeward guide vane losing effectiveness. A guide vane with a higher than optimal incidence angle starts performing better when the model is yawed.

For the guide vane with a NACA 2412 profile and a larger gap height (Print4) there are some differences between the simulated and experimental drag coefficients. However, it is interesting to see that when looking at the drag reduction of this guide vane configuration relative to the baseline model the CFD simulations and the wind tunnel experiment are in good agreement. Both methods agree that the effect of adding this guide vane to the tail is close to zero. To some extent the same can be said for all tested guide vanes: The experimental and numerical C_T values might differ, but the drag reduction effect of a guide vane relative to the baseline configuration found by both methods is approximately equal. Also the difference between the wind-averaged drag coefficient of the model as predicted by the numerical simulations and by the wind tunnel experiment is small. This is mainly due to the positive difference at $\Psi = 0°$ and the negative difference at $\Psi = 6°$ being averaged out.

To conclude, there are some discrepancies between the numerical and experimental results, especially in terms of the absolute drag values. But the CFD simulations seem to predict similar trends as the wind tunnel experiment and there is good agreement between the drag reductions of a guide vane relative to the baseline model. The are some discrepancies in the yaw angle behaviour, but the wind-averaged drag coefficients found by the numerical and experimental analysis agree very well. The average difference between $\bar{C}_{T,exp}$ and $\bar{C}_{T,sim}$ being 3.9 drag counts or 1.2%. Unfortunately only the total drag of the model could be measured in the wind tunnel, so the CFD's capabilities of predicting drag contributions, boundary layer profiles or for example the base pressure could not be validated.

6.1.3. Reflecting on initial 1/8-scale simulations

In chapter 3, some of the presented results were from the initial 1/8-scale simulations, while others were from full-scale simulations performed later in the research. The effect of scale on the GETS and baseline model has been discussed in subsection 3.2.1, but there were also some modelling differences between these initial and later simulations. Some inconsistencies between the results of the 1/8-scale and full-scale guide vane simulations were present, that can be related to those differences. Fig. 6.7 shows drag reductions of the NACA 6415 guide vane with a chord of $c = 0.4L_t$ at various incidence angles, found by the 1/8-scale and full-scale simulations relative to their respective baseline model. Note that apart from the difference in scale, the relative gap height of the full-scale guide vane in figure 6.7 is smaller.
It can be seen that in the full-scale simulation, the curve shows clear parabolic behaviour with a maximum drag reduction of 1.2 drag counts at $\alpha = 6°$. The scaled simulation shows a much more irregular curve and seems to indicate a maximum drag reduction at $8°$ or $10°$ which 2.5 drag counts. The curves are expected to be smooth when assuming a linear increase in lift coefficient with incidence angle and a quadratic drag polar. This is why the panel density at the leading edge of the guide vane was refined when moving to the full-scale simulations. In the initial simulation the insufficient panel density leads to a sudden shift of the stagnation point from the bottom to the top side of the airfoil, causing the irregular behaviour.

Next there is the difference in drag reduction predicted by the simulations. The curves in figure 6.7 represent different gap heights, making it difficult to compare. However, there was one NACA 6415 guide vane with $c = 0.4L_t$, $\alpha = 10°$ that has been simulated at 1/8-scale with a smaller gap height of $h_{gap} = 0.1L_t$. This suggested a 7 drag count reduction, which is a much larger difference to the results of the full-scale simulation. Now this can be compared to the results of both the wind tunnel experiment and the validation simulations presented in figures 6.4 to 6.6. Here the NACA 6415 $6°$ guide vane yielded a drag increase or a neutral drag effect at best. This is much more in line with the full-scale

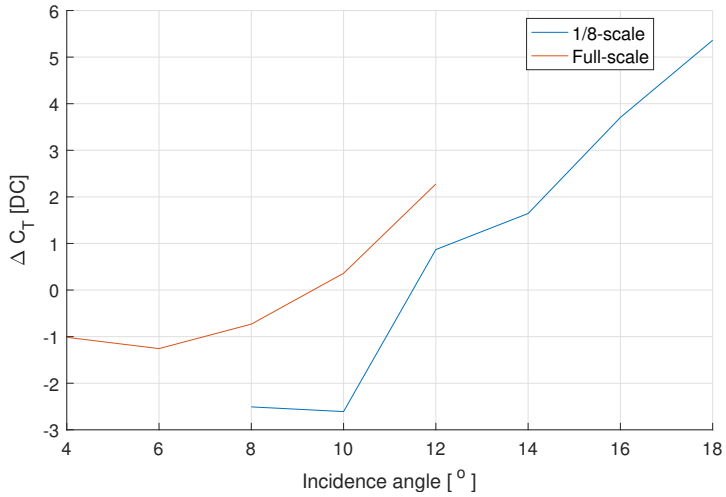

Figure 6.7: **Comparion of the drag reductions of a guide vane with NACA 6415 profile and chord length** $c = 0.4L_t$, $V = 25m/s$**. 1/8-scale simulation:** $h_{gap} = 0.2L_t$ **and** $Re = 0.6 \cdot 10^6$**. Full-scale,** $h_{gap} = 0.1L_t$, $Re = 5.1 \cdot 10^6$

simulation, so the results found in the 1/8-scale simulations seem to be erroneous. The cause of this error is that in the 1/8-scale simulations, the boundary layer is not modelled with enough inflation layers.

In the initial simulations the boundary layer was modelled with 5 prism layers and a growth factor of 1.2. The full-scale and validation simulations have a growth factor of 1.1 and as much layers as is required to reach the theoretical turbulent flat plate boundary layer thickness at the corresponding Reynolds number. A comparison of the boundary layer profiles calculated by the initial 1/8-scale, full-scale and validation simulations is given in figure 6.8. Here it can be seen that a linear velocity profile is modelled by fluent in the viscous sub-layer, which is thicker if the Reynolds number is lower. Next in the log-law region, it is clearly visible that the velocity profile of the initial 1/8-scale simulation shows non-smooth behaviour due to the insufficient number of inflation layers. Furthermore, the boundary layer is thicker than in the validation simulation, even though it has a lower Reynolds number than the initial simulation. However, this can not simply be blamed on the number of inflation layers, because both simulations have a different turbulence intensity, which influences mixing and the thickness of the boundary layer. To conclude, the initial scaled simulations did contain some modelling errors, which led to some inaccurate results. However, they have helped in the understanding of the guide vane concept and aided towards the design of later guide vane configurations, which is why they have been included in this thesis. But the conclusions and the analysis in the remainder of this chapter are based on the full-scale or validation simulations.

6.1.4. Wake analysis

As was explained at the beginning of this section, the validation simulations aim to match the conditions in the wind tunnel experiment as closely as possible. However, the support legs of the guide vane were not completely modelled. It was argued that this would have little influence on the drag, as the omitted parts are located on the inside of the tail panels. But as can be seen in figure 6.1, the supports on the bottom of the side vanes act as end plates. Also in all other simulations, no supports were present at the end of the guide vanes. Without the supports, the flow can travel around the tips of the guide vane, as well as the tail panels. This leads to tip vortices and can induce additional drag on the model. Note that in terms of drag contributions, the total drag of a vehicle is the combination of viscous and pressure drag. The vortex drag associated with the tip effects and other sources is just another way of decomposing the total drag to gain insight in the drag associated to lift. On generic vehicle models, the longitudinal vortices formed over the slanted backlight surface can cause a significant amount of drag,

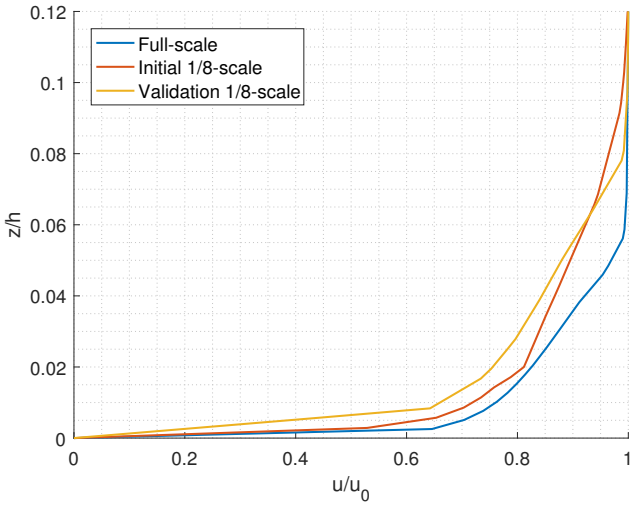

Figure 6.8: **Comparison of the boundary layer profiles calculated by the initial 1/8-scale simulation** $V = 25m/s$, $Re = 0.6 \cdot 10^6$**, full-scale** $V = 25m/s$, $Re = 5.1 \cdot 10^6$ **and 1/8-scale validation simulation** $V = 15m/s$, $Re = 3.8 \cdot 10^5$

as was shown for a fastback model by Howell and Le Good [28], the Ahmed body by Beaudoin and Aider [9] and the Davis model by Fuller and Passmore [22]. These vortices travel downstream and can be visualised on a crossflow plane far away from the model. It was not possible to test the influence of these end plates in the wind tunnel, but analysing the induced wake velocities in the CFD results will provide insight in the error introduced by not modelling them and potentially reveal other sources of vortex drag.

The tip vortices are visualised in figure 6.9 on a plane located mid-chord of the guide vane. Here it can clearly be seen how the flow curves around the tips of the guide vane due to the pressure difference between the inner and outer side. Although it is not presented here, the same vortices can be observed behind the baseline model (without a guide vane). The tail panels have a similar pressure difference between the inner and outer side, causing flow to travel around the tip. So the vortices in figure 6.9 are the combined effect of the tip losses of the tail and guide vane.

In figure 6.10 the transverse velocity components 4 vehicle lengths downstream of the model with a tail and guide vane are shown. Here it can be seen that when there is no crosswind, a pair of counter rotating vortices forms behind the model. However, note that the velocity vectors in figure 6.10 have been enlarged for readability and the transverse velocities are very small in magnitude. The wake structure is very similar to what has been observed behind the Ahmed body by Beaudoin and Aider [9]. When the model is placed at a $3°$ yaw angle, there is only one vortex on the leeward side. As the model is yawed, the airflow rolls over the sharp edges of the side of the model, which creates vortices. Note that in figure 6.10b, the lateral component of the incoming flow is first subtracted, to only show the induced transverse velocity components. Paying attention to the different colour scale in each of the figures, it can be seen that the vortex caused by the crosswind is much stronger than the trailing vortices of the tail and guide vane.

It is possible to compute the value of induced drag component from the transverse velocity components in the wake plane. This is done by taking a control volume around the body with the wake plane sufficiently downstream and computing the momentum integral in x-direction. Assuming that far downstream the streamwise velocity perturbations have disappeared, the induced or vortex drag can be described as: [68]

$$D_i = \frac{\rho}{2} \iint_S \left(v'^2 + w'^2\right) dS \tag{6.1}$$

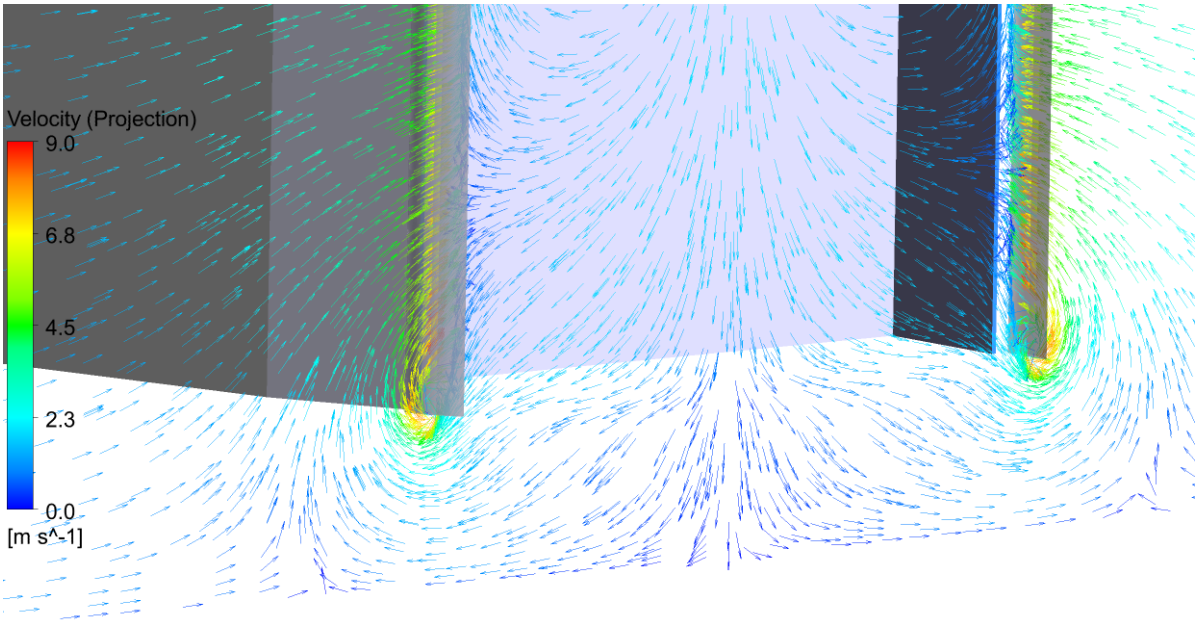

Figure 6.9: **Tip vortices on crossflow plane $0.5x/c$ behind the leading edge of the guide vane, $\Psi = 0°$**

This integral was computed on the plane 4 vehicle lengths downstream of the model, which was shown in figure 6.10. The results are presented in table 6.2 expressed in drag counts. The results confirm what was observed in figure 6.10; that the transverse velocity components are very small, which results in low induced drag. Moreover, the vortex drag in the yawed simulation is much larger than the drag caused by the counter rotating vortices in the symmetric case. Even though the values are very small, it can be seen in that adding the tail to the GETS model increases the induced drag. A guide vane configuration with high vane lift, the NACA 6415 profile with $\alpha = 12°$, was included to investigate the effect on the induced drag. It can be seen that this leads to a large increase relative to the baseline model and the other guide vane configuration, but that the magnitude of the induced drag is still very small. In the yawed case, the induced drag is much higher and the increase due to the tail and guide vanes relative to the GETS model is smaller, indicating that it originates from different sources. Due to time constraints, the NACA 6415 guide vane was unfortunately not simulated at a yaw angle.

Table 6.2: **Induced drag components computed 4 vehicle lengths downstream of the model at $0°$ and $3°$ yaw angle. Full-scale, $V = 25m/s$, $Re = 5.1 \cdot 10^6$. *this case was not simulated**

Configuration	Induced drag [DC]	
	$\Psi = 0°$	$\Psi = 3°$
GETS	0.007	1.2
Baseline	0.020	1.5
NACA 2412, $8°$	0.021	1.4
NACA 6415, $12°$	0.037	$(-)^*$

While performing the wake analysis, it was observed that the outcome of the momentum integral on the wake plane depended heavily on the distance behind the model. When the crossflow plane was moved more upstream, it led to larger induced drag results, but the plane would then intersect with the outer wake of the model. Further downstream, towards the end of the computational domain, the transverse flow velocities and resulting induced drag values would be close to zero. This is probably caused by artificial dissipation of the wake, which is a known issue when using a far-field analysis combined with a Navier-Stokes solver [68]. Also in experimental analyses there is a transfer of wake energy from rota-

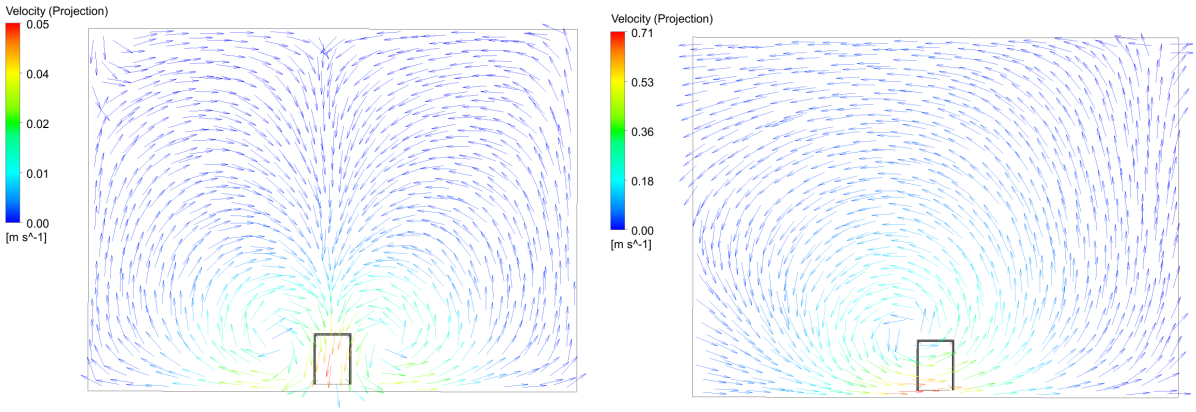

(a) $\Psi = 0°$ (b) $\Psi = 3°$

Figure 6.10: **Transverse velocity components 4 vehicles lengths behind the GETS model with a tail and a NACA 2412 airfoil at $\Psi = 0°$ and $3°$**

tional to longitudinal components according to Howell and Le Good [28]. This is why they determine the vortex drag by assuming a quadratic drag polar, instead of looking at the wake velocities. The induced drag values from the wake analysis in table 6.2 should therefore be seen more as an indication of the influence of the tail and guide vane on longitudinal vortices being formed.

It seems, however, that it can be assumed that tip losses of the NACA 2412 guide vane with an incidence angle of $8°$ do not add much vortex drag relative to the baseline model. This is logical, given that the U-shaped guide vane is a very slender wing and should therefore not suffer from tip losses. Furthermore, this guide vane has a small negative angle of attack with respect to the flow over the tail and produces only a small amount of lift.

6.2. Reflecting on guide vanes

The goal of this research was to improve the drag reduction achieved by a heavy duty vehicle tail by combining it with a guide vane. In the numerical as well as the experimental analysis, it was shown that adding a guide vane to a tail can lead to a larger drag reduction, but this does not tell the whole story. In this section a reflection on the concept of combining a tail and a guide vane will be given and the results that have been found so far will be put into context. The effect of combining a tail and a guide vane will be further investigated in order to give an answer to the research question.

The results demonstrate that the guide vane can provide additional drag reductions relative to the baseline model, but these are in the order of a few drag counts. The largest drag reduction that was found using the full-scale simulation was 3 drag counts. In the wind tunnel experiment all drag reductions that were measured were smaller than the drag uncertainty of the experimental set-up. The largest drag reduction measured in the wind tunnel was approximately 5 drag counts. In the field of aerodynamics a drag reduction of just a few drag counts can have a large impact, but one should also consider the practical implications of adding a guide vane to a tail. First of all a multi-element tail configuration such as investigated in this thesis makes the tail more complex. Moreover a guide vane with an airfoil profile is a complex shape that is difficult to produce. Most importantly the guide vane makes the tail assembly longer by 40%, which would require a type approval under current regulations. [18] Taking this into consideration, it would only make sense to implement a guide vane if it is more effective than simply elongating the tail by the same amount. This longer tail was simulated and the rear drag contributions are presented next to the GETS and baseline model and the best performing guide vane in figure 6.11. Here it can be seen that the longer tail with a length of 700mm yields a larger base drag reduction than

the guide vane. Despite the tail drag contribution of the longer tail being larger than the combined tail and guide vane drag, this leads to a lower drag coefficient for the GETS model. The longer tail yields a reduction of 6 drag counts relative to the baseline model, which is twice as large as the reduction by the guide vane.

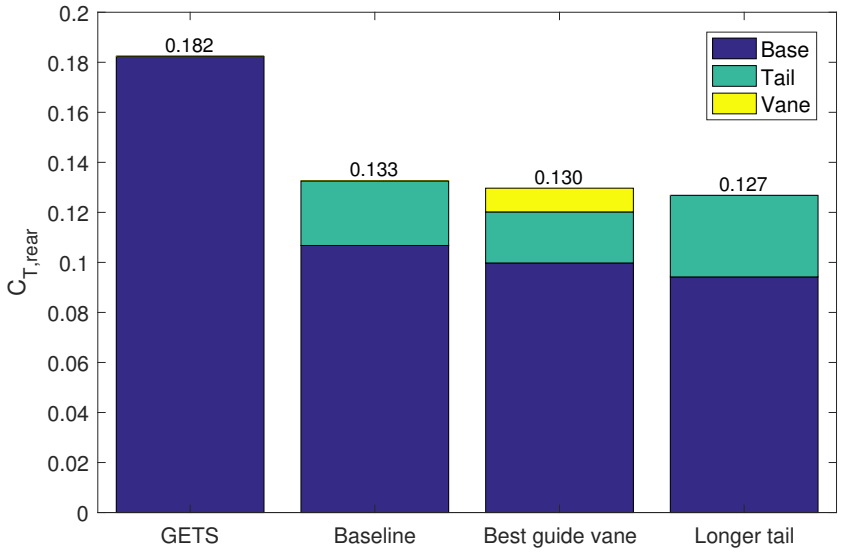

Figure 6.11: **Rear drag contributions of the GETS, baseline model, the NACA 2412 guide vane with $\alpha = 6^\circ$ and $c = 0.4L_t$ and a tail with length $L = 1.4L_t$. Full-scale $V = 25m/s$, $Re = 5.1 \cdot 10^6$**

This seems to indicate that the benefits of the guide vane and the tail, which by themselves have both been proven to be effective drag reduction devices for HDV's by van Straaten [67] and van Raemdonck [65], can not be added when they are combined. The results did show that the guide vane can further reduce the base drag component, but when doing so the additional vane drag counteracts any drag reductions. This asks for a further investigation on the working principle of the guide vane in combination with a tail in order to explain the unsatisfactory performance of the guide vane. The principle of the guide vane placed at the trailing edge of a tail is to direct the airflow behind the HDV inwards to reduce the size of the near wake and increase the base pressure by reducing the strength of the ring vortex in the wake. To direct the flow inwards the vane needs to produce lift and consequently it also produces a drag force. The results presented in this thesis have shown that this vane drag force limits the drag reduction that can be achieved by the guide vane. Airfoil profiles are known to produce lift at the expense of just a small amount of drag. So to understand the problem of vane drag one should consider the axis transformation from the guide vane to the vehicle axis system depicted in figure 6.12. As can be seen from the streamlines in figure 6.12 the flow is deflected downwards by the top tail panel and has an angle θ with respect to the driving direction, which is the vehicle's x-axis. It is customary to express the lift and drag of an airfoil in the axis system of the incoming flow, which is denoted with x'. The airfoil has an angle of attack with respect to the local flow and the lift is defined as the force component perpendicular to the flow velocity vector, which is the z'-axis. The guide vane in figure 6.12 produces an arbitrary resultant force $\vec{F}$, which can be decomposed in a lift component C_L and a small drag component C_D in the $x'z'$ axis system. However, the axis system that is of interest in this thesis is the vehicle axis system xz, as this is the direction in which the vehicle must overcome the drag force while driving. To avoid any confusion with the force coefficients normal and tangential to the chord of a wing, the force coefficients on the guide vane in the vehicle axis system will be called C_X, C_Y and C_Z. To complete the transformation from the $x'z'$ to the xz axis system one has to rotate over the flow angle θ. It can be seen in figure 6.12 that when the guide vane's resultant force $\vec{F}$ is decomposed in the vehicle

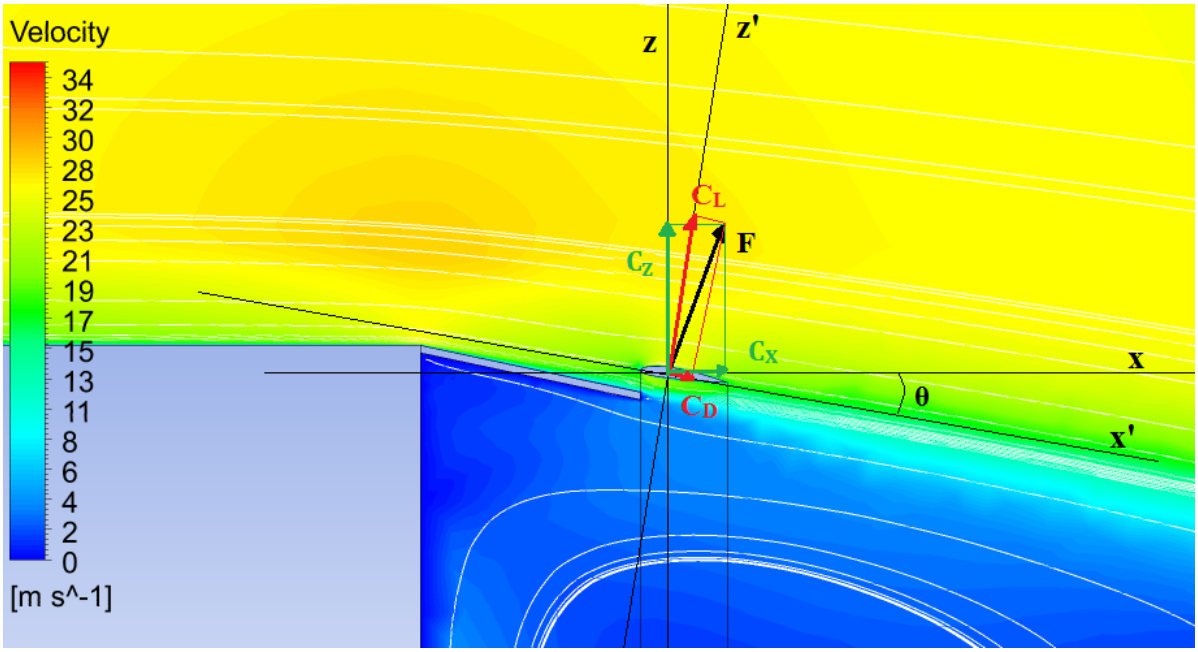

Figure 6.12: **Schematic of forces acting on the guide vane in the symmetry plane**

axis system, the drag component C_X is larger than C_D because of the component of C_L that points in the x-direction. The components attributing to the vane drag coefficient in the vehicle axis system C_X can be expressed as follows:

$$C_X = C_D \cos\theta + C_L \sin\theta \tag{6.2}$$

This force decomposition confirms the statement made earlier in this thesis, that for the guide vane placed at the trailing edge of a tail, low drag is more important than high lift. A component of the lift that is produced by the vane to guide the flow into the wake region, $C_L \sin\theta$, lies in the driving direction. So a part of the lift of the guide vane acts as a drag force on the vehicle. In order to understand the performance of the guide vane, it is important to know the value of θ in front of the vane. It can be seen in figure 6.12 that the flow angle in front of the vane is not the same everywhere. The flow is not separated, so it follows from the wall boundary condition that at the tail surface the flow angle $\theta = 12^\circ = \alpha_{tail}$. It can be seen that when moving away from the tail the flow angle becomes lower, until in the freestream $\theta = 0^\circ$. To estimate the flow angle in front of the guide van four lines are drawn parallel to the tail at different heights and the value of θ along these line is reported in figure 6.13. The small gap height $(h_{gap} = 50mm)$ is used in the full-scale simulations, so the leading edge of the guide vane is located at $x = -0.500m, h = 50mm$. At this height a value of $\theta = 10^\circ$ is found a chord length in front of the leading edge.

With the flow angle and consequently the component of the vane lift in the vehicle axis system known, the effect of the guide vane on the drag of the vehicle can be further analysed. If the effect of the vane lift on the rear drag contributions of the vehicle is known, it can be estimated what kind of L/D ratio is required from the airfoil profile to achieve a larger drag reduction in the vehicle axis system. This will reveal how much the guide vane can be improved by using a more efficient airfoil profile. To analyse this, the C_L of each vane is determined in its own axis system and added together in equation (6.3). In this way a single parameter of the inward flow deflection of the guide vane is created, as if the 'U-shaped' guide vane is folded into a single plane.

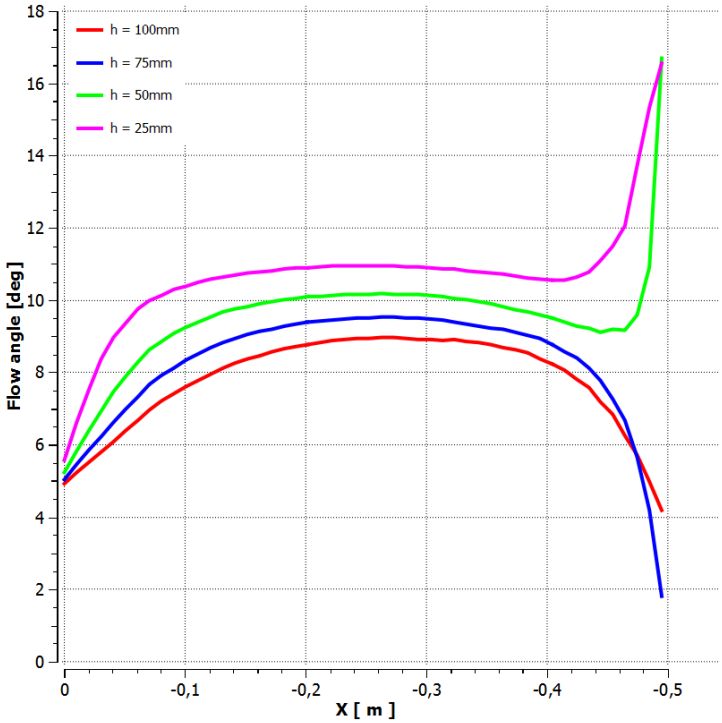

Figure 6.13: **Flow angle in front of the guide vane on lines parallel to the tail at various heights,** $h_{gap} = 50mm$

$$\begin{aligned} C_{L,vane} = \quad & C_{Z,top}\cos\theta + C_{X,top}\sin\theta \\ + \quad & C_{Y,left}\cos\theta + C_{X,left}\sin\theta \\ - \quad & C_{Y,right}\cos\theta + C_{X,left}\sin\theta \end{aligned} \tag{6.3}$$

This parameter is computed for the NACA 6415 and NACA 2412 guide vanes at the various incidence angles that were simulated in this thesis. The effect of $C_{L,vane}$ on the C_T of the base and the tail is presented in figure 6.14. Here it can be seen that for both airfoil profiles a linear relation seems to exist between $C_{L,vane}$, $C_{T,base}$ and $C_{T,tail}$. Therefore trend lines are plotted through the data points of the NACA 6415 (*) and NACA 2412 airfoil (x). It can be seen that, as expected, $C_{T,base}$ reduces with an increase in vane lift, whereas $C_{T,tail}$ increases with $C_{L,vane}$. It should be noted, however, that the presence of the guide vane initially reduces the tail drag contribution. The trend lines of both airfoils have an offset relative to each other. The NACA 2412 profile causes the same base drag reduction at a lower $C_{L,vane}$, but has a higher tail drag contribution. When both trend lines of each airfoil are added together, it can be seen that the net effect is very similar. Therefore it is assumed that the relation between $C_{T,rear}$ and $C_{L,vane}$ is independent of the airfoil, which makes it possible to consider the 'potential drag reduction' that could be achieved by an airfoil with a higher L/D ratio.

In figure 6.15 the trend lines of $C_{T,rear}$ have been averaged into a single line. Next to that, the component of the vane lift that lies in the tangential direction from equation (6.2), $C_{L,vane}\sin\theta$ is plotted. If these two lines are summed, it represents all the drag contributions of the guide vane configuration, except $C_{D,vane}$. The difference between this line and $C_{T,rear}$ of the baseline model, represents the drag 'potential drag reduction' that could be achieved if the guide vane produces no drag in its own axis system.

When zooming in on this potential drag reduction in figure 6.16, it can be observed that it increases

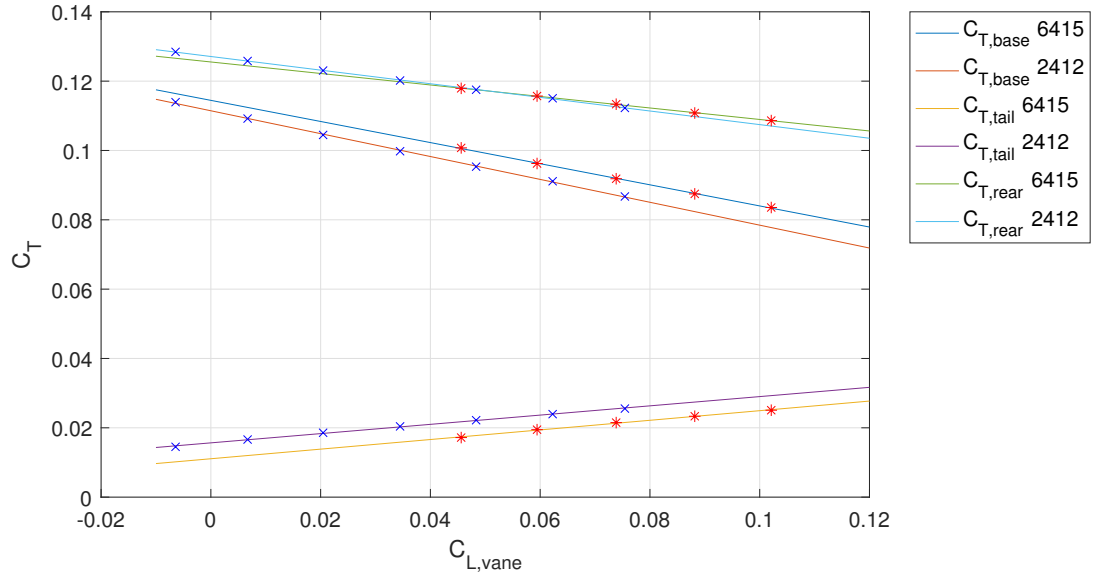

Figure 6.14: **Relation between $C_{L,vane}$ and base and tail drag contributions for the NACA 6415 NACA 2412 airfoils**

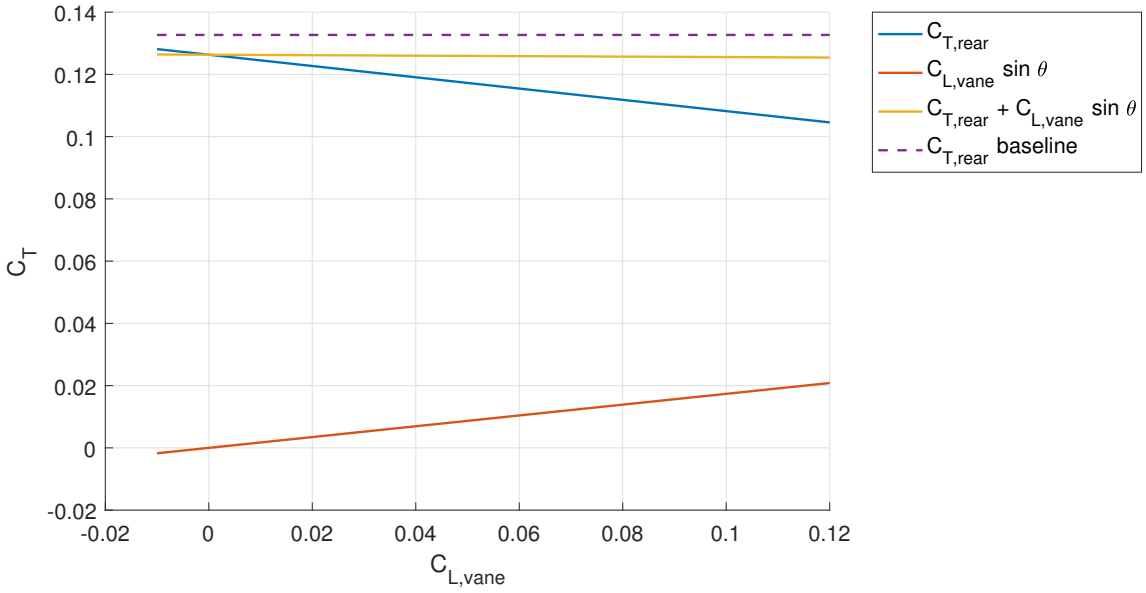

Figure 6.15: **Rear drag contributions of the guide vane configuration and baseline model, excluding $C_{D,vane}$**

by a small amount with $C_{L,vane}$. For this range of $C_{L,vane}$ the potential drag reduction that could be achieved by a perfect airfoil (producing no drag) is between 6 and 7 drag counts. The $C_{D,vane}$ curves of the two airfoils that have been tested in this thesis are plotted in figure 6.16. The drag reduction that is achieved by these profiles is the difference between the lines, which is highest for the NACA 2412 profile at an incidence angle of $8°$. Given that the potential drag reduction line is nearly horizontal, generally speaking the maximum drag reduction will be found for the airfoil with the lowest C_D. This means that in the search for an improved airfoil, rather than focussing on L/D, one should look for an airfoil with the lowest drag coefficient. Important to note is that it is impossible for $C_{D,vane}$ to become zero when changing the airfoil profile. A part of the $C_{D,vane}$ is viscous drag, which depends on the wetted area of the guide vane. Given that the boundary layer at the rear-end of an HDV can be assumed turbulent, this is also a considerable amount. In the simulation of the NACA 2412 guide vane

with incidence angle $8°$, 1.7 drag counts of $C_{T,vane}$ is viscous drag. It was not possible to compute the viscous drag in the vane axis system, but it can be assumed to be very similar because the contribution $C_{L,vane} \sin\theta$ is a pressure drag. If the 1.7 drag counts viscous drag are deducted from the potential drag reduction, this leaves around 5 drag counts. Compared to the 3 drag count reduction that was found using the NACA 2412 profile, it can be concluded that finding a more efficient airfoil will have a minimal effect on the drag reduction that can be achieved using a guide vane in combination with a tail.

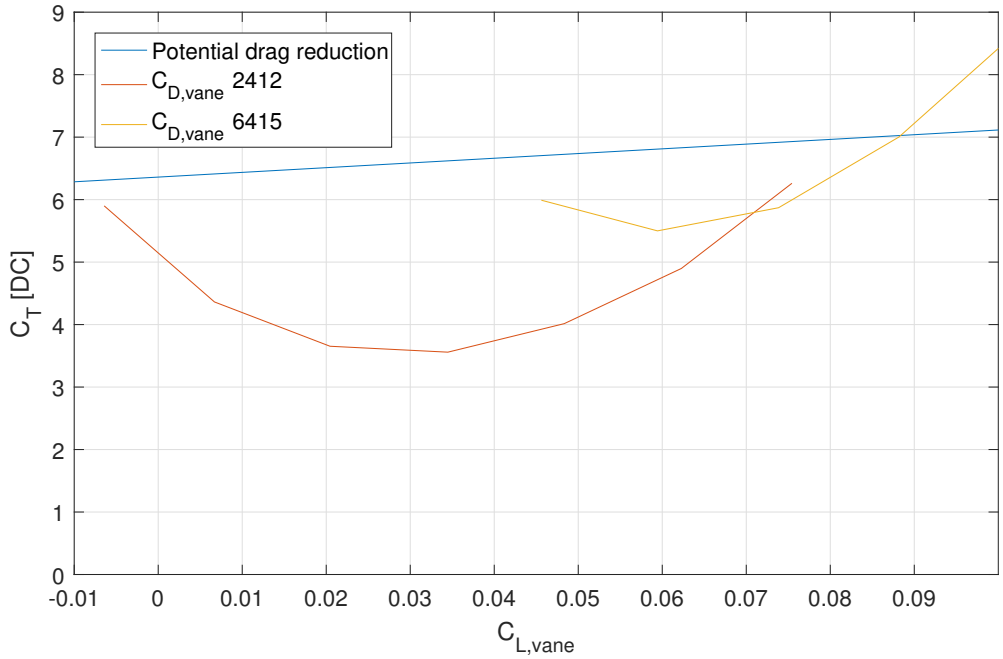

Figure 6.16: **Potential drag reduction that can be achieved by a guide vane versus the $C_{D,vane}$ of the NACA 6415 and NACA 2412 guide vanes**

The above analysis of the potential drag reduction of the guide vane concept showed that changing the airfoil can only provide a minimal improvement relative to the current best performing guide vane. This will still not be enough to give the guide vane concept an edge over the tail elongation. In an ultimate attempt to find a larger drag reduction, the influence of the guide vane on the tail drag was investigated. In figure 6.14 it was found that the presence of the guide vane initially reduces the tail drag contribution, after which $C_{T,tail}$ increases as $C_{L,vane}$ is increased. In figure 6.17 the influence of $C_{L,vane}$ on the tail drag components is split between the inside and outside tail panels and the small rear trailing edge of the tail. It can be seen that when $C_{L,vane} = 0$, the vane reduces the tail drag with approximately 10 drag counts, which is almost exclusively caused by the outside panels producing less drag. As the incidence angle and consequently $C_{L,vane}$ increases, the drag of the tail rises until at the largest simulated incidence angle $C_{T,tail}$ is approximately equal to the baseline value. The inside tail panels also see a small rise in drag as $C_{L,vane}$ increases, while the effect on the small rear edge of the tail is negligible.

A closer look at the pressure distribution over the baseline tail and a guide vane configuration reveals the reason for the behaviour of the tail drag coefficient. In figure 6.18 it can be seen that the start of the tail, which is denoted with $x = 0m$, there is a low pressure peak on the top surface of the tail. This peak is caused by the slant angle of the tail, which causes a flow expansion. Following the tail downstream there is an adverse pressure gradient that starts steep and bottoms out as it approaches the trailing edge of the tail. The line that is approximately horizontal corresponds to the inside tail panel and the

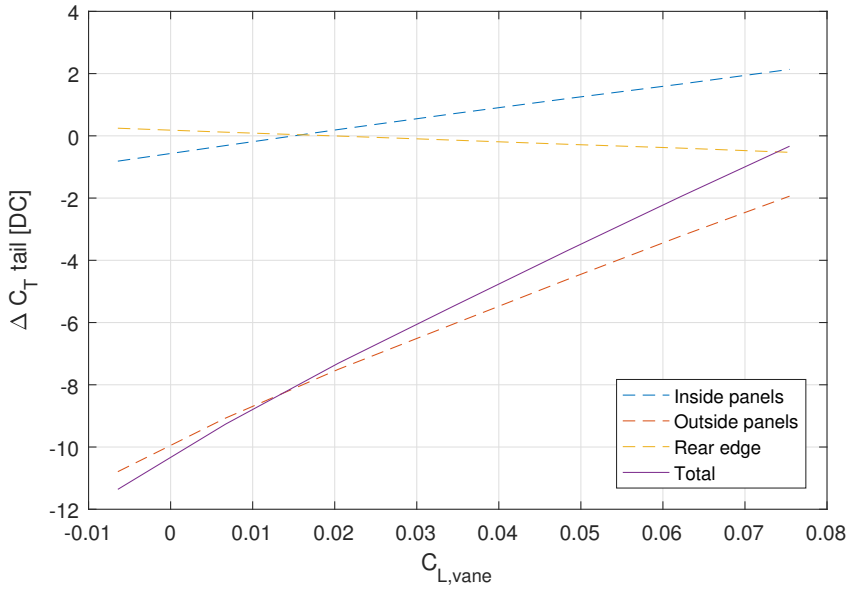

Figure 6.17: **Influence of $C_{L,vane}$ on the tail drag components of the NACA 2412 guide vane relative to the baseline tail. Full-scale, $V = 25m/s$, $Re = 5.1 \cdot 10^6$**

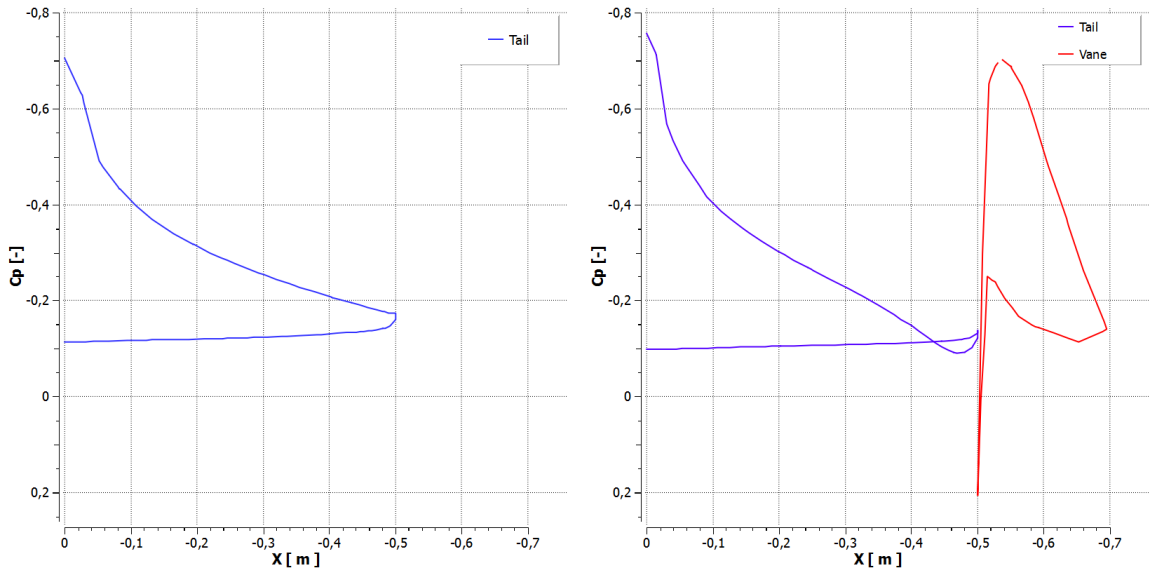

(a) Baseline model (b) NACA 2412, $\alpha = 12°$

Figure 6.18: **Pressure distribution over the tail and guide vane in the symmetry plane**

pressure on this panel is related to the pressure in the wake and consequently the base pressure. In terms of drag, there is a negative pressure acting on the outside surface that faces rearwards, which causes a drag force. On the forward facing inside panel, a smaller negative pressure is acting, causing a small thrust force. Now it is possible to look at the influence of the guide vane on the pressure distribution in figure 6.18b and the change of $C_{T,tail}$ with $C_{L,vane}$ in figure 6.17. From these figures, three interaction effects between the tail and the guide vane can be identified:

- The stagnation point near the leading edge of the guide vane causes a high pressure region that locally increases the pressure on the top surface of the tail
- The suction peak on the top surface of the guide vane causes a low pressure zone that extends

upstream, increasing the low pressure peak at the start of the tail

- The downwash of the guide vane increases the pressure in the wake, which causes the pressure on the bottom tail panel to increase

The first point is the reason for the drag of the upper tail panel to decrease relative to the baseline case when a guide vane is present. Whereas the second effect is the cause for the increase in $C_{T,tail}$ when $C_{L,vane}$ increases. Additionally, when the vane angle is increased the stagnation point moves to the bottom side of the vane and slightly down stream. This causes the first effect to act on a smaller portion near the trailing edge of the tail. Finally the last interaction effect between the guide vane and the tail is the reason for the drag of the inside tail panels to increase relative to the baseline model when $C_{L,vane}$ increases.

Taking notice of these three interactions that were found between the guide vane and the tail, it was attempted to improve the mutual interference between these elements. This was done by rounding the last part of the tail, to increase the slant angle at the trailing edge of the tail. It was found that this increased the drag of the tail, but leads to a lower base and vane drag. Also the longitudinal position of the guide vane was varied to investigate whether this would improve the interaction between the tail and guide vane. An overview of the results of these design modifications are presented in table 6.3. For these simulations the best performing guide vane configuration with a NACA 2412 airfoil, $\alpha = 8°$, $h_{gap} = 0.1L_t$ and $c = 0.4L_t$ is used as a baseline. To give a clear overview of the effect of rounding the last part of the tail and longitudinally shifting the guide vane, the ΔC_T values in table 6.3 are relative to this guide vane configuration.

Table 6.3: **Effect of design modifications on the rear drag contributions relative to the NACA 2412 guide vane with $\alpha = 8°$, $h_{gap} = 0.1L_t$ and $c = 0.4L_t$. Full-scale, $V = 25m/s$, $Re = 5.1 \cdot 10^6$. Positive Δx_{LE} is upstream**

		ΔC_T [DC]			
Radius [mm]	Δx_{LE} [mm]	Base	Tail	Vane	Total
-	$-0.25c_v$	-2.6	2.9	-1.0	-0.7
-	$-0.05c_v$	-0.7	0.7	-0.4	-0.4
-	$0.05c_v$	0.5	0.5	-0.1	-0.1
$0.3L_t$	0	-5.2	9.6	-4.8	-0.3
$0.4L_t$	$-0.05c_v$	-4.2	6.8	-3.1	-0.4
$0.4L_t$	0	-3.4	6.5	-3.3	-0.3
$0.4L_t$	$0.05c_v$	-3.1	6.3	-3.6	-0.5
$0.6L_t$	0	-2.1	3.8	-2.0	-0.3
Smaller vane	$0.5c_v$	3.9	2.3	-5.8	0.4

First of all, it can be seen that all simulated design modifications yield a larger drag reduction than the 'standard' NACA 2412, $\alpha = 8°$ guide vane, though the differences are small. That is remarkable, as this was the best performing guide vane configuration until now. Except for the configuration with a forward (positive) shift of the guide vane van no rounding, all simulated designs reduce the base drag. Rounding the aft part of the tail leads to a larger tail drag contribution, but this is counteracted by the positive effect on the vane and base drag. When rounding of the aft tail section with a radius of $R = 0.4L_t$ is combined with a $0.05c_{vane} = 10mm$ forward translation of the guide vane, an additional reduction of half a drag count is found. There is one configuration, with no rounding and a $-0.25c_{vane} = 50mm$ downstream translation of the vane, that yields a larger drag reduction. However, when considering the comparison between the guide vane and the tail elongation in figure 6.11, moving the guide vane further downstream is not the right approach to improve the performance. Therefore it is much more valuable if an additional drag reduction can be achieved by translating the vane forward, making the tail assembly shorter.

With this in mind, the 'standard' NACA 2412 $8°$ guide vane was simulated with a shorter chord length of $c = 0.2L_t$. It can be seen in table 6.3 that this increases the base and tail drag relative to the guide vane with $c = 0.4L_t$, but also leads to a smaller vane drag component. With a drag coefficient of $C_T = 0.2005$, this is a 0.4 drag count increase compared to the larger vane, but it reduces the full-scale length of the tail assembly with 100mm.

To conclude, the combination of rounding the aft tail portion and a forward shift of the guide vane yields a new 'best performing guide vane' that offers 3.5 drag count reduction relative to the baseline model. Given the drag of the full-scale baseline model, $C_T = 0.203$, this corresponds to a 1.7% drag reduction. The streamlines around this configuration as seen from the symmetry plane are given in figure 6.19. The C_p distribution over the tail and guide vane is plotted next to the 'standard configuration' with a straight tail and the leading edge of the guide vane placed at the tail's trailing edge.

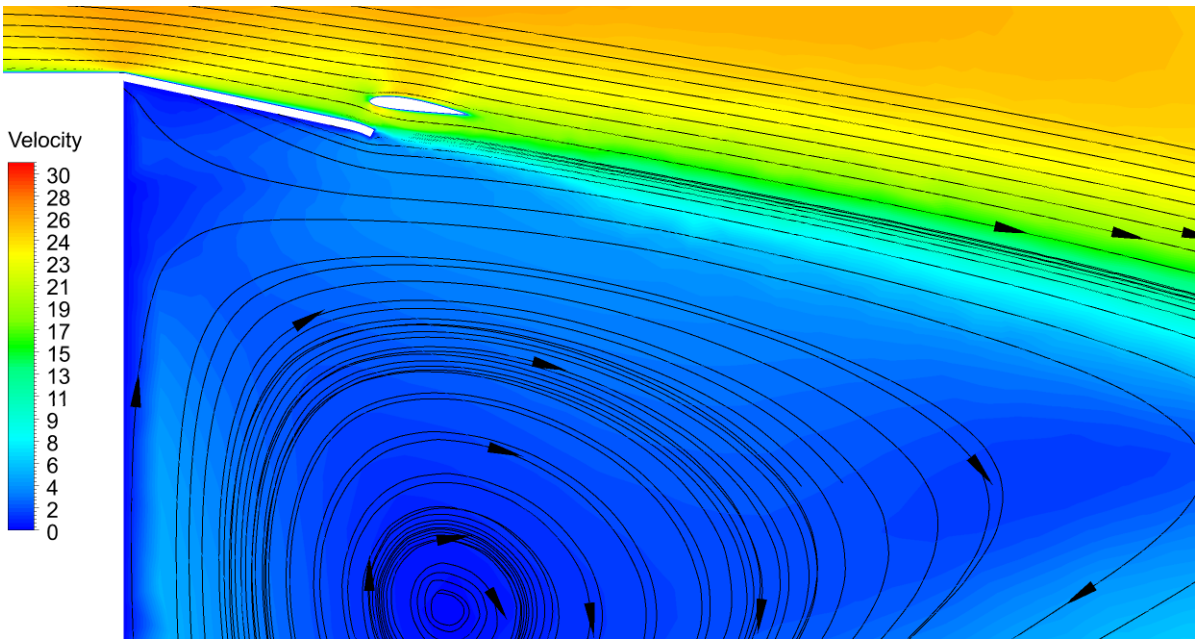

Figure 6.19: **Streamlines around the NACA 2412 guide vane with $\alpha = 8°$, rounded tail end and upstream translation. Full-scale, $V = 25m/s$, $Re = 5.1 \cdot 10^6$**

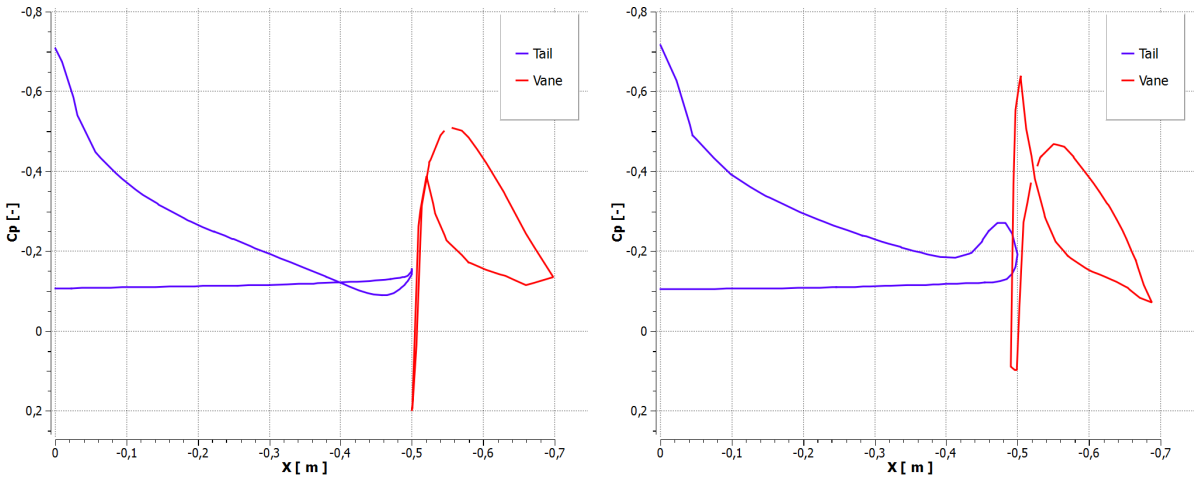

(a) NACA 2412 $\alpha = 8°$ (b) $R = 0.4L_t$, $\Delta x_{LE} = 0.05c_v$

Figure 6.20: **Pressure distribution over the tail and guide vane in the symmetry plane**

7

Conclusion and recommendations

In this chapter conclusions will be drawn based on the results of the numerical and experimental analysis performed in this thesis research. Furthermore the used methodology will be reviewed and recommendations regarding potential future work will be given.

7.1. Conclusion

In order to have a chance of meeting the ambitious goals of the Paris climate agreement, global CO_2 emissions should peak in the coming years followed by a steady decline to reach zero emissions in the second half of the century. Aerodynamic add-on devices for the rear-end of heavy duty vehicles can reduce the emissions related to road transport in the short term by lowering the pressure drag. In this thesis research, two existing drag reduction devices, a tail and guide vanes, have been combined in an attempt to improve the performance. It has been investigated how the drag reduction achieved by a tail on an HDV can be improved by combining it with a guide vane. This has been done by performing both numerical simulations and a wind tunnel experiment on the GETS model, in order to answer the research question: ”What is the effect of combining a tail and a guide on the drag coefficient of a bluff body?”

GETS and baseline model

The goal of this research was to improve the performance of a tail behind an HDV by combining it with a guide vane. To do so, first the effect of such a tail on the flow around the GETS model had to be assessed. The numerical simulations showed that the drag of the GETS model can be reduced by 50 to 56 drag counts, or 17.3% to 19.7% by adding the baseline tail in 1/8-scale and full-scale simulations respectively. In the wind tunnel experiment the tail provided a wind-averaged drag reduction of 45 drag counts. Comparing the numerical and experimental results of the GETS and baseline model revealed that this difference was mainly caused by the two analyses not agreeing on the drag coefficient of the GETS model. Whereas the wind-averaged drag coefficient of the baseline model as predicted by the simulations and the experiment differed less than a drag count. It is suspected that the discrepancies between the numerical and experimental C_T values of the GETS model are caused by the mean flow solution found by the RANS simulations. While in the experiment the measured C_T value is an average of a series of instantaneous solutions. The tail is known to stabilise the wake of the GETS model, so this might explain why the agreement between the numerical and experimental results is better for the GETS model fitted with a tail. The increase in C_T with yaw angle was underestimated by the numerical simulations for both models, possibly because of the used mesh not being valid for the highest yaw angle. Because only the results of the balance measurement can be used for validating the numerical simulations, it is difficult to make definitive statements about the source of the discrepancies.

Results of combining a tail with a guide vane

It was found that placing a guide vane on the trailing edge of an HDV tail can reduce the base drag. Initially it was expected that the guide vanes should be oriented to have a substantial angle with respect to the local flow to guide the flow inside the wake region. This was based on the research of van Straaten [67] on guide vanes placed directly on the trailing edge of an HDV, where he concluded that high lift was more important than a high L/D ratio for these guide vanes. The opposite was found to be the case for the guide vane placed on the trailing edge of a tail.

Because the vane is operating in the deflected flow field around the tail, a component of the lift force lies in the tangential direction. The effect of $C_{L,vane}$ on the rear drag contributions of the model was analysed. This revealed that increasing $C_{L,vane}$ reduces the base drag, but increases the tail drag contribution. Initially the interaction between the tail and the guide vane causes a drag reduction, but this positive effect reduces as $C_{L,vane}$ increases. Three interaction effects were identified between the tail drag and $C_{L,vane}$: The guide vane influences the pressure distribution over the outside tail panel locally through the stagnation pressure and further upstream due to the suction peak, while the inside tail panel is subjected to the pressure inside the wake. Combining the effect of $C_{L,vane}$ on the base and tail drag with the lift component in the tangential direction, the resulting drag reduction with respect to the baseline model is nearly independent of $C_{L,vane}$. The maximum drag reduction is achieved if the guide vane is operating at its minimum drag condition. In the full-scale simulations the largest drag reduction was achieved by the NACA 2412 airfoil, lowering C_T with 3 drag counts. It is estimated that this can be increased to a maximum of 5 drag counts if a lower drag airfoil is used. The optimal incidence angle of the NACA 2412 airfoil was found to be $8°$ with respect to the vehicle x-axis, while for the more cambered NACA 6415 profile it is $6°$. Both these incidence angles yield a slightly negative angle of attack with respect to the local flow, which was found to have an angle of $10°$ at a height of $h_{gap} = 0.1L_t$ above the tail. The gap height has been varied in the simulations as well as the wind tunnel experiment and it was found that a low gap height leads to the largest drag reduction. In the simulations this could be traced back to a lower vane drag contribution, which follows from the change in flow angle and velocity with height above the tail. A guide vane with a small chord length $(c = 0.2L_t)$ was found to yield a larger drag reduction than a larger guide vane $(c = 0.4L_t)$, due to the vane drag being lower. The effect of the smaller chord length reduces as h_{gap} is decreased and disappears at the lowest gap height. Unfortunately the smaller guide vane could not be tested in the wind tunnel because the profile thickness would be too small for a 3D-printed prototype to provide the required stiffness.

The wind tunnel experiment confirmed that a guide vane can improve the drag reduction of the baseline tail behind the GETS model. The highest single drag reduction measured in the wind tunnel was 5 drag counts. The NACA 2412 airfoil guide vanes with vane angle $6°$ and $8°$ both yielded a wind-averaged drag reduction of two drag counts. The numerical and experimental results were compared to validate the methodology. There are some discrepancies between the numerical and experimental results, especially in terms of the absolute drag values. But overall the CFD simulations predict similar trends as the wind tunnel experiment and there is good agreement between the drag reductions of a guide vane relative to the baseline model. The are some discrepancies in the yaw angle behaviour, but the wind-averaged drag coefficients found by the numerical and experimental analysis agree very well. The average difference between $\bar{C}_{T,exp}$ and $\bar{C}_{T,sim}$ being only 3.9 drag counts or 1.2%. This validates that the methodology combining numerical simulations and scaled wind tunnel experiments can be used to design drag reduction devices for heavy duty vehicles. Though the small drag reductions caused by the guide vane and the large experimental uncertainty make it difficult to make definitive statements.

The insights into the interaction between the guide vane and the tail led to small modifications of the design of the tail and guide vane. When rounding of the aft tail section was combined with a $0.05c_{vane}$ forward translation of the guide vane, an additional reduction of half a drag count was found. This yields a new ‘best performing guide vane’ that offers 3.5 drag count reduction relative to the baseline model.

Given the drag of the full-scale baseline model, $C_T = 0.203$, this corresponds to a 1.7% drag reduction. More fine-tuning of the design, combined with a lower drag airfoil can probably lead to a larger drag reduction. However, ultimately combining a guide vane and a tail will at best yield around the same drag reduction as a tail elongation of the same length, which is a simpler solution.

7.2. Recommendations

Methodology

The uncertainty of the experimental set-up was too high to make definitive statements about the small drag reductions provided by the guide vanes. The accuracy of the measurements should be increased if one wants to investigate small drag reductions. The 7 drag count (2.14%) uncertainty observed during the experiment was much higher than the sensor error of 0.06% reported by Alons [2] in the calibration experiment. Previous research at the faculty that made use of the same external balance, reported a similar drag uncertainty, such as 1.68% found by Terra [58] and 2.20% by Mulkens [42]. Having spoken to various staff members involved in experiments in the OJF, it was concluded that it has been a long time since the balance has been calibrated. Besides, the signal-to-noise ratio observed on the time-varying signal from the balance was very high. The source of this noise can be anything from unsteady aerodynamic effects, vibrations of the test set-up, amplifier noise or electro-magnetic interference with the tunnel motor. The author believes that the current practice of averaging the signal over 60 seconds is not the best way to address this. Therefore it is recommended that a recalibration of the balance and an investigation of the source of the measurement noise is performed to improve the accuracy of the experimental set-up in the OJF.

However, it has to be noted that handling the model in between configuration changes also introduces an uncertainty that can not be attributed to the measurement set-up. Furthermore, due to the flexible layout of the OJF, the ground board and supporting structure were largely handmade, specifically for this experiment. The resulting single purpose structure was not very stable, which can also have had an influence on the measurement noise. This would be less of an issue when testing in a closed section tunnel with more permanent support structures, like the Low Turbulence Tunnel of the TU Delft.

The alignment of the model in the wind tunnel using a laser tool, proved to be a tedious and difficult task. At 0° yaw angle a minimum drag was measured, but also a small sideforce was present, making it unclear if the model was perfectly aligned. Possibly the model was not completely symmetric due to manufacturing inaccuracies. Pressure tabs on both sides of the model could help indicate that the model is aerodynamically aligned. Unfortunately the rotation device could not achieve negative yaw angles, which would also have helped verifying the alignment over a larger range of angles.

The validation procedure indicated good overall agreement between the numerical and experimental analysis. However, if more different types of measurements, such as pressure, wake or PIV measurements, were performed in the wind tunnel, it would have been able to validate the simulation results more thoroughly. This would have required more time in the wind tunnel, which was unfortunately not available. The largest discrepancies were in the drag increase with yaw angle and the drag of the single GETS model in general. The simulations at high yaw angles might be improved by extending the mesh refinement box on the leeward side. The difference between the numerical and experimental results of the single GETS model can attributed to the inability of the RANS simulations to capture certain flow phenomena. Using a different numerical method, such as LES, DNS or Lattice Boltzmann Methods should lead to higher accuracy results.

Future research

This research has shown that it is difficult to improve the drag reduction provided by a tail without making it longer. Similarly, the research by Kruijssen [34] showed that asymmetrical tail deflections could only marginally improve the wind-averaged drag with respect of the (axisymmetric) baseline tail. This

can be regarded from the positive side, by stating that the drag reduction of the current tail is very close to the optimal drag reduction that can be achieved by an add-on device of this size. An obvious way to improve it would be make the tail longer, which relies on regulations. The effect of a longer tail is a higher taper ratio, which can also be achieved without increasing the total length of the vehicle by reducing the cross-section of the trailer before the trailing edge. Hirz [26] proposed reducing the height of the trailer at the rear actively if the trailer is not completely full, so there is minimum impact on the maximum load capacity. Last summer, the variable trailer concept in combination with a boat tail was road tested within the TRANSFORMERS project [62] as can be seen in figure 7.1. This showed promising results and will be further developed in the coming years.

Figure 7.1: **Road test of a variable trailer geometry concept reducing the height at the rear of the trailer combined with a boat tail. Source: TRANSFORMERS [62]**

To improve the performance of the tail without making it longer, solutions should be sought in active flow control methods such as (oscillatory) boundary layer blowing or suction. This might be able to improve the drag reduction of a tail without increasing its size, given that the passive methods investigated in this study were not able to yield large improvements. Another improvement would be to include a bottom panel to the tail. For this to be truly effective and worth reducing the accessibility of the rear doors during loading and docking operations, it would require a re-design of the under-body flow near the rear end. As more and more sources of pressure drag on HDV's are treated, at some point reducing the viscous drag will also become important and require smoother designs. To conclude, in the future, aerodynamics should be incorporated throughout design of the tractor-trailer system as a whole to lead to more effective transport vehicles.

Bibliography

[1] Aeroserve Technologies Ltd. Airtab. https://http://www.airtab.com/. Accessed: 23-01-2018.

[2] H.J. Alons. OJF external balance-documentation. Technical report, NLR-CR-2008 695, Dutch Aerospace Laboratory NLR, 2008.

[3] J.D. Anderson. *Fundamentals of aerodynamics*. Tata McGraw-Hill Education, 2010.

[4] ANSYS Inc. Ansys fluent 14.0 theory guide. 2011.

[5] Avantechs Inc. Vorblade trailer wing system. https://http://www.vorblade.com/trailer-wing-system/. Accessed: 23-01-2018.

[6] A.K. Barlas. *Active aerodynamic load control on wind turbines: Aeroservoelastic modeling and wind tunnel experiments*. Delft University of Technology, 2011.

[7] P.W. Bearman. Investigation of the flow behind a two-dimensional model with a blunt trailing edge and fitted with splitter plates. *Journal of Fluid Mechanics*, 21(02):241–255, 1965.

[8] P.W. Bearman and J.C. Owen. Reduction of bluff-body drag and suppression of vortex shedding by the introduction of wavy separation lines. *Journal of Fluids and Structures*, 12(1):123–130, 1998.

[9] J. Beaudoin and J. Aider. Drag and lift reduction of a 3D bluff body using flaps. *Experiments in fluids*, 44(4):491–501, 2008.

[10] J. Cai, T.L Chng, and H.M. Tsai. On vortical flows shedding from a bluff body with a wavy trailing edge. *Physics of Fluids (1994-present)*, 20(6):064–102, 2008.

[11] I.B. Celik, U. Ghia, P.J. Roache, et al. Procedure for estimation and reporting of uncertainty due to discretization in CFD applications. *Journal of fluids Engineering-Transactions of the ASME*, 130 (7), 2008.

[12] K.R. Cooper. SAE wind tunnel test procedure for trucks and buses. *SAE Recommended Practice J*, 1252, 2012.

[13] K.R. Cooper and B. Ewald. Bluff body blockage corrections for closed and open test sections (chapter 6 of AGARDograph 336 wind tunnel wall corrections). *Advisory Group for Aerospace Research & Development AGARD, France*, 1998.

[14] Core Writing Team, R.K. Pachauri, and L.A. Meyer. *Climate change 2014: synthesis report. Contribution of Working Groups I, II and III to the fifth assessment report of the Intergovernmental Panel on Climate Change*. IPCC, Geneva, Switzerland, 2014.

[15] Daimler AG. The future is electric | E-FUSO. http://efuso.jp/. Accessed: 7-12-2017.

[16] S.P. Doppenberg. Drag influence of tails in a platoon of bluff bodies. Master's thesis, Delft University of Technology, Faculty of Aerospace Engineering, 2015.

[17] E.G. Duell and A.R. George. Experimental study of a ground vehicle body unsteady near wake. Technical report, SAE Technical Paper, 1999.

[18] European Union. Directive (EU) 2015/719 of the european parliament and of the council of 29 april 2015 amending council directive 96/53/EC laying down for certain road vehicles circulating within the community the maximum authorised dimensions in national and international traffic and the maximum authorised weights in international traffic. *Official Journal of the European Union*, L115, 2015.

[19] European Union. *EU transport in figures - Statistical pocketbook 2017*. Office for Official Publications of the European Communities, Luxembourg, 2017. ISBN 978-92-79-62312-7.

[20] European Commision Eurostat. *Panorama of Transport*. Office for Official Publications of the European Communities, Luxembourg, 2009. ISBN 978-92-79-11119-8.

[21] K. Frey. Verminderung des strömungswiderstandes von körpern durch leitflächen. *Forschung im Ingenieurwesen*, 4(2):67–74, 1933.

[22] J. Fuller and M.A. Passmore. The importance of rear pillar geometry on fastback wake structures. *Journal of Wind Engineering and Industrial Aerodynamics*, 125:111–120, 2014.

[23] H.C. Garner, E.W. Rogers, W.E. Acum, and E.C. Maskell. Blockage effects in closed or open tunnels (chapter 5 of Agardograph 109 wind tunnel wall corrections). *Advisory Group For Aerospace Research & Development AGARD, France*, 1966.

[24] T. Gheyssens. Aerodynamic analysis of a platoon of bluff bodies subjected to cross wind. Master's thesis, Delft University of Technology, Faculty of Aerospace Engineering, 2016.

[25] P. Gilliéron and A. Kourta. Aerodynamic drag reduction by vertical splitter plates. *Experiments in fluids*, 48(1):1–16, 2010.

[26] M. Hirz and S. Stadler. A new approach for the reduction of aerodynamic drag of long-distance transportation vehicles. *SAE International Journal of Commercial Vehicles*, 6(2013-01-2414):453–458, 2013.

[27] L. Hjelm and B. Bergqvist. European truck aerodynamics - a comparison between conventional and CoE truck aerodynamics and a look into future trends and possibilities. In *The Aerodynamics of Heavy Vehicles II: Trucks, Buses, and Trains*, pages 469–477. Springer, 2009.

[28] J. Howell and G. Le Good. Vortex drag for a simple bluff body at incidence in ground proximity. Technical report, SAE Technical Paper, 2005.

[29] W. Hucho and G. Sovran. Aerodynamics of road vehicles. *Annual review of fluid mechanics*, 25 (1):485–537, 1993.

[30] G. Jacobs. Numerical investigation on drag reduction of a 2D bluff body through guiding vanes. Master's thesis, Delft University of Technology, Faculty of Aerospace Engineering, 1998.

[31] JOST SDR. SDR - drag reduction and less spray mist. `http://www.invetr.com/body-and-structure/roof-diffusers`. Accessed: 07-03-2017.

[32] B. Khalighi, S. Zhang, C. Koromilas, et al. Experimental and computational study of unsteady wake flow behind a bluff body with a drag reduction device. Technical report, SAE Technical Paper, 2001.

[33] S. Krajnović. Large eddy simulation exploration of passive flow control around an ahmed body. *Journal of Fluids Engineering*, 136(12):103–121, 2014.

[34] F. Kruijssens. The effect of asymmetric base flaps on the drag of a tractor-trailer for four crosswind angles. Master's thesis, Delft University of Technology, Faculty of Aerospace Engineering, 2017.

[35] M. Lanfrit. A best practice guideline to handle automotive external aerodynamics with fluent. *Fluent Inc. - Technical Notes*, 2005.

[36] J. Leuschen and K.R. Cooper. Summary of full-scale wind tunnel tests of aerodynamic drag-reducing devices for tractor-trailers. In *The aerodynamics of heavy vehicles II: trucks, buses, and trains*, pages 451–462. Springer, 2009.

[37] A. Martín-Alcántara, E. Sanmiguel-Rojas, C. Gutiérrez-Montes, and C. Martínez-Bazán. Drag reduction induced by the addition of a multi-cavity at the base of a bluff body. *Journal of Fluids and Structures*, 48:347–361, 2014.

[38] Materialise. Technical specifications tuskxc2700w. `http://www.materialise.com/en/manufacturing/materials/tuskxc2700w`. Accessed: 28-11-2017.

[39] M. Meinshausen, N. Meinshausen, W. Hare, et al. Greenhouse-gas emission targets for limiting global warming to 2 c. *Nature*, 458(7242):1158–1162, 2009.

[40] Mercedes Benz. Efficiency run 2015. `https://www.mercedes-benz.com/en/mercedes-benz/vehicles/trucks/efficiency-run-2015/`. Accessed: 30-08-2016.

[41] J.D. Miller and C. Façanha. The state of clean transport policy: a 2014 synthesis of vehicle and fuel policy developments. Technical report, International Council on Clean Transportation, Washington, DC, 2014.

[42] W.P.K.M Mulkens. Aerodynamic analysis of drag reduction devices for the tractor-trailer gap. Master's thesis, Delft University of Technology, Faculty of Aerospace Engineering, 2016.

[43] G. Muttitt et al. The sky's limit: Why the paris climate goals require a managed decline of fossil fuel production. *Oil Change International, September*, 2016.

[44] C.N. Nayeri, J. Haff, D. Greenblatt, L. Loefdahl, and C.O. Paschereit. Drag reduction on a generic tractor-trailer using active flow control in combination with solid flaps. In *The Aerodynamics of Heavy Vehicles II: Trucks, Buses, and Trains*, pages 179–191. Springer, 2009.

[45] J.C. Nouwens. Aerodynamic analysis on add-on devices for a semi-trailer truck with underbody obstruction. Master's thesis, Delft University of Technology, Faculty of Aerospace Engineering, 2015.

[46] W.L. Oberkampf, T.G. Trucano, and C. Hirsch. Verification, validation, and predictive capability in computational engineering and physics. *Applied Mechanics Reviews*, 57(5):345–384, 2004.

[47] H. Park, D. Lee, W. Jeon, et al. Drag reduction in flow over a two-dimensional bluff body with a blunt trailing edge using a new passive device. *Journal of Fluid Mechanics*, 563:389–414, 2006.

[48] S. Perzon, J. Janson, and L. Höglin. On comparisons between CFD methods and wind tunnel tests on a bluff body. Technical report, SAE Technical Paper, 1999.

[49] M.S. Petrusma and S.L. Gai. Bluff body wakes with free, fixed, and discontinuous separation at low reynolds numbers and low aspect ratio. *Experiments in fluids*, 20(3):189–198, 1996.

[50] D. Pointer, T. Sofu, Chang J., and D. Weber. Applicability of commercial CFD tools for assessment of heavy vehicle aerodynamic characteristics. In *The Aerodynamics of Heavy Vehicles II: Trucks, Buses, and Trains*, pages 349–361. Springer, 2009.

[51] S.B. Pope. *Turbulent Flows*. Cambridge University Press, 2000.

[52] P. Roache. Error bars for CFD. In *41st Aerospace Sciences Meeting and Exhibit*, page 408, 2003.

[53] SAE International. Sae guidelines for aerodynamic assessment of medium and heavy commercial ground vehicles using computational fluid dynamics. *SAE Recommended Practice J*, 2966, 2013.

[54] H.J. Schmidt, R. Woszidlo, C.N. Nayeri, and C.O. Paschereit. Drag reduction on a rectangular bluff body with base flaps and fluidic oscillators. *Experiments in Fluids*, 56(7):1–16, 2015.

[55] A. Seifert, O. Stalnov, D. Sperber, G. Arwatz, V. Palei, S. David, I. Dayan, and I. Fono. Large trucks drag reduction using active flow control. In *The Aerodynamics of Heavy Vehicles II: Trucks, Buses, and Trains*, pages 115–133. Springer, 2009.

[56] G. Sovran and M.S. Bonn. Formulae for the tractive-energy requirements of vehicles driving the EPA schedules. Technical report, SAE Technical Paper, 1981.

[57] B.L. Storms, J.C. Ross, J.T. Heineck, et al. An experimental study of the ground transportation system (GTS) model in the NASA Ames 7-by 10-ft wind tunnel. Technical report, NASA, 2001.

[58] W. Terra, A. Sciacchitano, and F. Scarano. Evaluation of aerodynamic drag of a full-scale cyclist model by large-scale tomographic-PIV. In *International Workshop on Non-Intrusive Optical Flow Diagnostics*, 2016.

[59] Tesla Inc. Tesla semi. `https://www.tesla.com/semi/`. Accessed: 7-12-2017.

[60] W.A. Timmer. Snelle pakken. *Nieuw archief voor wiskunde*, 5(4):292–295, 2004.

[61] N. Tombazis and P.W. Bearman. A study of three-dimensional aspects of vortex shedding from a bluff body with a mild geometric disturbance. *Journal of Fluid Mechanics*, 330(1):85–112, 1997.

[62] TRANSFORMERS. Configurable and adaptable trucks and trailers for optimal transport efficiency. `http://www.transformers-project.eu/`. Accessed: 13-02-2018.

[63] United Nations Framework Convention on Climate Change UNFCCC. Paris climate agreement. United Nations Treaty Collection, `https://treaties.un.org/pages/ViewDetails.aspx?src=TREATY&mtdsg_no=XXVII-7-d&chapter=27&clang=_en`. Accessed: 8-12-2017.

[64] P. van Leeuwen. Computational analysis of base drag reduction using active flow control. Master's thesis, Delft University of Technology, Faculty of Aerospace Engineering, 2009.

[65] G.M.R. Van Raemdonck. *Design of Low Drag Bluff Road Vehicles*. TU Delft, Delft University of Technology, 2012.

[66] G.M.R. Van Raemdonck and M.J.L. van Tooren. Data acquisition system of a tractor-trailer combination to register aerodynamic performances. In *The Aerodynamics of Heavy Vehicles II: Trucks, Buses, and Trains*, pages 299–310. Springer, 2009.

[67] M. van Straaten. Computational and experimental investigation on base drag reduction of a generic transportation system by guiding vanes. Master's thesis, Delft University of Technology, Faculty of Aerospace Engineering, 2007.

[68] L.L.M. Veldhuis. Aircraft aerodynamics primer - part 5, 2016 - 2017. Faculty of Aerospace Engineering, Delft University of Technology.

[69] Wabco OptiFlow. Wabco optiflow tail. `http://www.wabco-auto.com/products/category-type/trailer-aerodynamics/optiflow-tail/`. Accessed: 25-01-2017.

[70] S. Watkins. *Windtunnel modelling of vehicle aerodynamics: with emphasis on turbulent wind effects on commercial vehicle drag*. Victorian University of Technology, 1990.

[71] S. Watkins, J.W. Saunders, and P.H. Hoffmann. Comparison of road and wind-tunnel drag reductions for commercial vehicles. *Journal of Wind Engineering and Industrial Aerodynamics*, 49(1):411–420, 1993.

[72] F.M. White and I. Corfield. *Viscous fluid flow*, volume 3. McGraw-Hill Higher Education Boston, 2006.

[73] R.M. Wood. Impact of advanced aerodynamic technology on transportation energy consumption. Technical report, SAE Technical Paper, 2004.

[74] R.M. Wood and S.X.S. Bauer. Simple and low-cost aerodynamic drag reduction devices for tractor-trailer trucks. Technical report, SAE Technical Paper, 2003.